Barry Doyle · Karol Miller
Adam Wittek · Poul M.F. Nielsen *Editors*

Computational Biomechanics for Medicine

New Approaches and New Applications

Springer

Computational Biomechanics for Medicine

Barry Doyle • Karol Miller • Adam Wittek
Poul M.F. Nielsen
Editors

Computational Biomechanics for Medicine

New Approaches and New Applications

Springer

Editors
Barry Doyle
School of Mech. and Chem. Engineering
The University of Western Australia
Perth, WA, Australia

Karol Miller
School of Mech. and Chem. Engineering
The University of Western Australia
Perth, WA, Australia

Adam Wittek
School of Mech. and Chem. Engineering
The University of Western Australia
Perth, WA, Australia

Poul M.F. Nielsen
Auckland Bioengineering Institute
The University of Auckland
Auckland, New Zealand

ISBN 978-3-319-15502-9 ISBN 978-3-319-15503-6 (eBook)
DOI 10.1007/978-3-319-15503-6

Library of Congress Control Number: 2015937617

Springer Cham Heidelberg New York Dordrecht London

Printed on acid-free paper

Springer International Publishing AG Switzerland is part of Springer Science+Business Media (www.springer.com)

Preface

Perhaps the greatest challenge facing the computational engineering community is to extend the success of computational mechanics to fields outside traditional engineering, in particular, to biology, the biomedical sciences, and medicine.

The field of computational biomechanics continues to progress towards clinically relevant simulations. Personalized medicine will play a major role in the future of health care and personalized computational simulations have a clear part to play. We, the computational biomechanics community, are making real advancements towards this ultimate goal of comprehensive patient-specific modelling, but there is of course much more work to do yet.

The Computational Biomechanics for Medicine book series began in 2009 with the first edition. Since then, it has become an annual reference for the community to read about the latest advancements in the field. The book series provides an opportunity for specialists in computational sciences to describe their new research and discuss the possibilities of applying their techniques to computer-integrated medicine.

This sixth volume of the Computational Biomechanics for Medicine series comprises 12 of the latest developments in new approaches and new applications, from researchers in Australia, New Zealand, USA, Switzerland, and France. Some of the exciting topics discussed are as follows:

- Tailored computational models
- Growth and remodeling
- Soft tissue mechanics
- Medical image analysis
- Clinically relevant simulations

The Computational Biomechanics for Medicine book series not only provides the community with a snapshot of the latest state of the art, but importantly, when computational biomechanics and patient-specific modeling is a mainstay of personalized health care, it will serve as a key reminder of how the field has developed over the years.

We would like to thank the authors for submitting high quality work and the reviewers for helping with paper selection.

We hope you enjoy this year's volume.

Perth, WA, Australia — Barry Doyle
Perth, WA, Australia — Karol Miller
Perth, WA, Australia — Adam Wittek
Auckland, New Zealand — Poul M.F. Nielsen

Contents

Part II New Applications

Part I
New Approaches

Vademecums for Real-Time Computational Surgery

D. Gonzalez, I. Alfaro, C. Quesada, E. Cueto, and F. Chinesta

1 Vademecums and Computational Vademecums

The usage of vademecums in medicine or engineering possesses a strong tradition. In essence, known solutions to problems of interest were compiled in a volume of easy consult, such as, the vademecum published by Bernoulli in the nineteenth century [3]. There, solutions to parametric problems were compiled and graphically represented for consult, as in Fig. 1, for instance.

In the field of computational surgery it is frequent to ask for real-time responses. What we exactly mean by the term "real-time" strongly depends on the context but, in essence, it means that we are asking a computer for a response that ranges between 1 kHz for surgery training systems equipped with haptic peripherals to some seconds or minutes in surgery planning applications. But in this last example simulations tend to include long-term behavior of the surgery outcome.

These requirements are extremely astringent if one takes into account the difficulty associated with surgery: highly non-linear soft living tissues, distributed contact, fluid–solid interaction, multi-scale phenomena (that go from the centimeter scale to the sub-cellular scale of gene regulatory systems [2]). Therefore, many computational strategies have tried to pre-compute off-line as many things as

D. Gonzalez • I. Alfaro • E. Cueto
Universidad de Zaragoza, Aragon Institute of Engineering Research,
Universidad de Zaragoza, Zaragoza, Spain
e-mail: gonzal@unizar.es; iciar@unizar.es; ecueto@unizar.es

C. Quesada
Universidad de Zaragoza, Zaragoza, Spain
e-mail: cquesada@unizar.es

F. Chinesta (✉)
Ecole Centrale de Nantes, Nantes, France
e-mail: Francisco.Chinesta@ec-nantes.fr

B. Doyle et al. (eds.), *Computational Biomechanics for Medicine*,
DOI 10.1007/978-3-319-15503-6_1

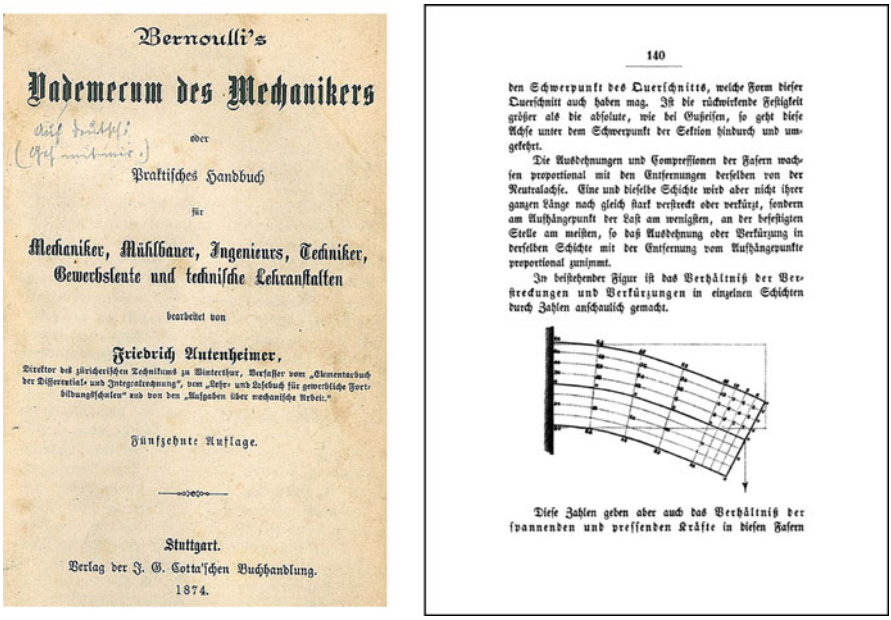

Bernoulli's

Vademecum des Mechanikers

oder

Praktisches Handbuch

für

Mechaniker, Mühlbauer, Ingenieurs, Techniker, Gewerbsleute und technische Lehranstalten

bearbeitet von

Friedrich Autenheimer,

Direktor des züricherischen Technikums zu Winterthur, Verfasser vom „Elementarbuch der Differential- und Integralrechnung", vom „Lese- und Lesebuch für gewerbliche Fortbildungsschulen" und von den „Aufgaben über mechanische Arbeit."

Fünfzehnte Auflage.

Stuttgart.
Verlag der J. G. Cotta'schen Buchhandlung.
1874.

140

den Schwerpunkt des Querschnitts, welche Form dieser Querschnitt auch haben mag. Ist die rückwirkende Festigkeit größer als die absolute, wie bei Gußeisen, so geht diese Achse unter dem Schwerpunkt der Sektion hindurch und umgekehrt.

Die Ausdehnungen und Compressionen der Fasern wachsen proportional mit den Entfernungen derselben von der Neutralachse. Eine und dieselbe Schichte wird aber nicht ihrer ganzen Länge nach gleich stark verstreckt oder verkürzt, sondern am Aufhängepunkt der Last am wenigsten, an der befestigten Stelle am meißten, so daß Ausdehnung oder Verkürzung in derselben Schichte mit der Entfernung vom Aufhängepunkte proportional zunimmt.

In beistehender Figur ist das Verhältniß der Verstreckungen und Verkürzungen in einzelnen Schichten durch Zahlen anschaulich gemacht.

Diese Zahlen geben aber auch das Verhältniß der spannenden und pressenden Kräfte in diesen Fasern

Fig. 1 The vademecum for engineers developed by Bernoulli [3]

possible, and to store them in memory for fast and easy-to-access posterior usage, just like traditional vademecums did. For instance, the so-called fast finite elements for surgery simulation [4] employed static condensation of finite element matrices for linear elastic materials intensively. These matrices could be stored in memory and used when necessary. In essence, when computing $\mathbf{u} = \mathbf{K}^{-1}\mathbf{f}$, matrix $\mathbf{K}^{-1}$ could be stored for the sake of speedup.

This can be seen as a sort of very simple computational vademecum, in the sense that $\mathbf{K}^{-1}$ is pre-computed and consulted as often as necessary. However, when dealing with truly non-linear soft living tissues this naive approach is no longer possible, since a consistent tangent stiffness matrix updating should be performed, and this is a very CPU-consuming task. The beam bending vademecum of Fig. 1 could be updated if we consider the computational solution of a non-linear, hyperelastic beam bending problem in which the displacement field $\mathbf{u}$ is computed by taking the position of the applied load as a parameter, see Fig. 2, thus by

$$\mathbf{u} = \mathbf{u}(\mathbf{x}, \mathbf{s}),$$

where $\mathbf{s}$ is the position of the acting load along the boundary of the beam.

This is, roughly speaking, the approach followed in our latest works to develop a means to deal with highly non-linear problems (hyperelastic soft tissues, contact, cutting, etc.) appearing in computational surgery: to make an intensive use of computational vademecums as far as possible. In the subsequent sections we

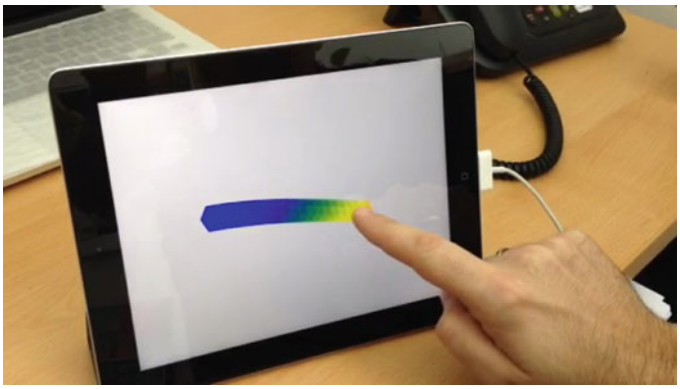

Fig. 2 An example of computational vademecum that updates the original one shown in Fig. 1

review the main theoretical aspects of this technique as well as some details of its implementation. Other approaches, such as the employ of explicit finite elements, [11, 12], are also equally possible and have given excellent results in recent years.

2 A Vademecum for a Hyperelastic Solid Under Arbitrary Loads

The main drawback of the appealing method sketched in the previous section is that the complexity of the problem (say, the number of degrees of freedom once the problem is approximated by the finite element method, for instance) grows exponentially with the number of parameters of the model, considered as extra-coordinates. To avoid this burden, we have employed a model order reduction technique coined as proper generalized decomposition (PGD). In essence, PGD techniques avoid this exponential growth in the number of degrees of freedom by assuming the solution as a finite sum of separable functions, i.e.,

$$\mathbf{u} \approx \sum_{i}^{N} F_i(\mathbf{x}) \cdot G_i(\mathbf{s}).$$

In this approach there are two main aspects to be discussed: how to determine the functions F_i and G_i and how to determine how many of these functions are necessary (i.e., the precise value of N).

Determining functions F_i and G_i is made by a greedy algorithm [5] that gives rise to a non-linear problem for each sum (even if the original one is linear), whose solution can be obtained by your favorite linearization technique. We have made an

intensive use of fixed-point, alternating directions algorithms to this end, with very satisfactory results [13, 14]. The number of terms, N, in turn, can be determined by an appropriate error estimator [1].

As usual in the FE method, PGD considers the weak form of the equilibrium equations (balance of linear momentum) without inertia terms. The (doubly-) weak form of the problem, extended to the whole geometry of the organ, Ω, and the portion of its boundary which is accessible to load during surgery, $\bar{\Gamma} \subset \Gamma_t$, consists in finding the displacement $\mathbf{u} \in \mathscr{H}^1$ such that for all $\mathbf{u}^* \in \mathscr{H}_0^1$:

$$\int_{\bar{\Gamma}} \int_{\Omega} \nabla_s \mathbf{u}^* : \boldsymbol{\sigma} \, d\Omega \, d\bar{\Gamma} = \int_{\bar{\Gamma}} \int_{\Gamma_{t2}} \mathbf{u}^* \cdot \mathbf{t} d\Gamma \, d\bar{\Gamma}, \tag{1}$$

where $\Gamma = \Gamma_u \cup \Gamma_t$ represents the boundary of the organ, divided into essential and natural regions, and where $\Gamma_t = \Gamma_{t1} \cup \Gamma_{t2}$, i.e., regions of homogeneous and non-homogeneous, respectively, natural boundary conditions. Here, $\mathbf{t} = -\mathbf{e}_k \cdot \delta(\mathbf{x} - \mathbf{s})$, where δ represents the Dirac-delta function and $\mathbf{e}_k$ the unit vector along the z-coordinate axis (we consider here, as mentioned before, and for the ease of exposition, a unit load directed towards the negative z axis of reference).

The Dirac-delta term is then regularized, and approximated by a truncated series of separable functions in the spirit of the PGD method, i.e.,

$$t_j \approx \sum_{i=1}^{m} f_j^i(\mathbf{x}) g_j^i(\mathbf{s}),$$

where m represents the order of truncation and f_j^i, g_j^i represent the jth component of vectorial functions in space and boundary position, respectively.

The key aspect of the method here proposed is that PGD techniques efficiently construct the computational vademecum $\mathbf{u}(\mathbf{x}, \mathbf{s})$ by constructing, in an iterative way, an approximation to the solution in the form of a finite sum of separable functions [6]. If we assume that the method has converged to a solution, at iteration n of this procedure,

$$u_j^n(\mathbf{x}, \mathbf{s}) = \sum_{k=1}^{n} X_j^k(\mathbf{x}) \cdot Y_j^k(\mathbf{s}), \tag{2}$$

where the term u_j refers to the jth component of the displacement vector, $j = 1, 2, 3$, and functions $\mathbf{X}^k(\mathbf{x})$ and $\mathbf{Y}^k(\mathbf{s})$ represent the separated functions used to approximate the unknown field, obtained in previous iterations of the PGD algorithm. At this stage, the objective of PGD is to provide the solution with an improvement given by the $(n + 1)$th term of the approximation,

$$u_j^{n+1}(\mathbf{x}, \mathbf{s}) = u_j^n(\mathbf{x}, \mathbf{s}) + R_j(\mathbf{x}) \cdot S_j(\mathbf{s}), \tag{3}$$

where $\mathbf{R}(\mathbf{x})$ and $\mathbf{S}(\mathbf{s})$ are the sought functions that improve the approximation. In an equivalent manner, admissible variations of this displacement field will be given by

$$u_j^*(\mathbf{x},\mathbf{s}) = R_j^*(\mathbf{x}) \cdot S_j(\mathbf{s}) + R_j(\mathbf{x}) \cdot S_j^*(\mathbf{s}).$$

Of course, the price to pay during this procedure is that, even if the original problem is linear, PGD needs for the solution of a non-linear problem, i.e., to determine a product of functions, see Eq. (3). We describe now a practical way to do this, although the reader can think of any linearization method available in the literature.

For the computation of $\mathbf{S}(\mathbf{s})$ assuming $\mathbf{R}(\mathbf{x})$ is known, following standard assumptions of variational calculus, we have

$$u_j^*(\mathbf{x},\mathbf{s}) = R_j(\mathbf{x}) \cdot S_j^*(\mathbf{s}), \tag{4}$$

or, equivalently, $\mathbf{u}^*(\mathbf{x},\mathbf{s}) = \mathbf{R} \circ \mathbf{S}^*$. The symbol "$\circ$" stands here for the so-called entry-wise, Hadamard or Schur multiplication for vectors. Once substituted into Eq. (1) gives

$$\int_{\bar{\Gamma}} \int_{\Omega} \nabla_s(\mathbf{R} \circ \mathbf{S}^*) : \mathbf{C} : \nabla_s \left(\sum_{k=1}^{n} \mathbf{X}^k \circ \mathbf{Y}^k + \mathbf{R} \circ \mathbf{S} \right) d\Omega\, d\bar{\Gamma}$$
$$= \int_{\bar{\Gamma}} \int_{\Gamma_{t2}} (\mathbf{R} \circ \mathbf{S}^*) \cdot \left(\sum_{k=1}^{m} \mathbf{f}^k \circ \mathbf{g}^k \right) d\Gamma\, d\bar{\Gamma},$$

or, equivalently

$$\int_{\bar{\Gamma}} \int_{\Omega} \nabla_s(\mathbf{R} \circ \mathbf{S}^*) : \mathbf{C} : \nabla_s(\mathbf{R} \circ \mathbf{S}) d\Omega\, d\bar{\Gamma}$$
$$= \int_{\bar{\Gamma}} \int_{\Gamma_{t2}} (\mathbf{R} \circ \mathbf{S}^*) \cdot \left(\sum_{k=1}^{m} \mathbf{f}^k \circ \mathbf{g}^k \right) d\Gamma\, d\bar{\Gamma} - \int_{\bar{\Gamma}} \int_{\Omega} \nabla_s \left(\mathbf{R} \circ \mathbf{S}^* \right) \cdot \mathscr{R}^n d\Omega\, d\bar{\Gamma},$$

where $\mathscr{R}^n$ represents:

$$\mathscr{R}^n = \mathbf{C} : \nabla_s \mathbf{u}^n.$$

Since the symmetric gradient operates on spatial variables only, we have:

$$\int_{\bar{\Gamma}} \int_{\Omega} (\nabla_s \mathbf{R} \circ \mathbf{S}^*) : \mathbf{C} : (\nabla_s \mathbf{R} \circ \mathbf{S}) d\Omega\, d\bar{\Gamma}$$
$$= \int_{\bar{\Gamma}} \int_{\Gamma_{t2}} (\mathbf{R} \circ \mathbf{S}^*) \cdot \left(\sum_{k=1}^{m} \mathbf{f}^k \circ \mathbf{g}^k \right) d\Gamma\, d\bar{\Gamma} - \int_{\bar{\Gamma}} \int_{\Omega} \left(\nabla_s \mathbf{R} \circ \mathbf{S}^* \right) \cdot \mathscr{R}^n d\Omega\, d\bar{\Gamma},$$

where all the terms depending on $\mathbf{x}$ are known and hence all integrals over Ω and Γ_{t2} (support of the regularization of the initially punctual load) can be computed to derive an equation to determine $\mathbf{S}(\mathbf{s})$.

The computation of $R(\mathbf{x})$ once $S(\mathbf{s})$ is known follows equivalent guidelines and will not be repeated here. The interested reader can consult [14] for more details.

If we consider, as is generally the case for soft living tissues, hyperelastic constitutive laws, large strain tensors (usually the Green–Lagrange tensor $\mathbf{E}$) must be equally linearized. Again, different alternatives exist. In [13] an explicit approach was developed that renders, in general, very good results without stability problems. On the contrary, in [14] an approach was developed based on the combined use of PGD and asymptotic numerical methods (ANM). In this last approach, the solution $\mathbf{u}$ is expanded in terms of a power series of an arc-length parameter, providing a sort of continuation method in which there is no need of updating tangent stiffness matrices.

Implementation of this technique for the simulation of liver palpation during cholecystectomy, for instance, provided haptic feedback rates on a simple laptop (in our case a MacBook pro running MAC OSX 10.7.4, equipped with 4 Gb RAM and an Intel core i7 processor at 2.66 GHz). Feedback rates in the order of 1 kHz are obtained without problems for a Geomagic Touch haptic device [8], see Fig. 3.

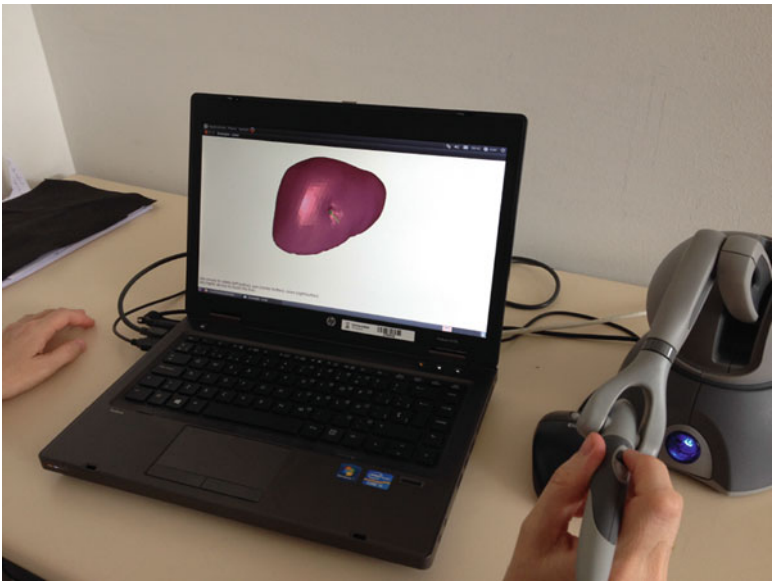

Fig. 3 Implementation of liver palpation with haptic feedback on a HP ProBook 6470b laptop equipped with a Geomagic Touch device

2.1 Interactive Vademecums

Providing the surgery simulator with full interactivity needs to include dynamics in the system. But pre-computing and storing in memory data relative to interactive solid dynamics of non-linear solids is far from being trivial. In [9] we presented a method based on the construction of a computational vademecum whose parameters were precisely initial values (displacement and velocity) of the problem. In this way, a sort of black-box integrator was made such that, once nodal displacement and velocity values were known at time t, they could be considered as initial values for the subsequent time step $t + \triangle t$.

Consider the weak form of the solid dynamics equations, i.e.: given $\mathbf{f}$, $\mathbf{g}$, $\mathbf{h}$, $\mathbf{u}_0$, and $\dot{\mathbf{u}}_0$ find $\mathbf{u}(t) \in \mathscr{S}_t = \{\mathbf{u} | \mathbf{u}(\mathbf{x}, t) = \mathbf{g}(\mathbf{x}, t),\ \mathbf{x} \in \Gamma_u,\ \mathbf{u} \in \mathscr{H}^1(\Omega)\}$, $t \in [0, T]$, such that for all $\mathbf{w} \in \mathscr{V}\{\mathbf{u} | \mathbf{u}(\mathbf{x}, t) = \mathbf{0},\ \mathbf{x} \in \Gamma_u,\ \mathbf{u} \in \mathscr{H}^1(\Omega)\}$,

$$(\mathbf{w}, \rho\ddot{\mathbf{u}}) + a(\mathbf{w}, \mathbf{u}) = (\mathbf{w}, \mathbf{f}) + (\mathbf{w}, \mathbf{h})_{\Gamma_t} \tag{5a}$$

$$(\mathbf{w}, \rho\mathbf{u}(0)) = (\mathbf{w}, \rho\mathbf{u}_0) \tag{5b}$$

$$(\mathbf{w}, \rho\dot{\mathbf{u}}(0)) = (\mathbf{w}, \rho\dot{\mathbf{u}}_0). \tag{5c}$$

The main ingredient of the developed computational vademecum is to express the displacement field as a parametric field such:

$$\mathbf{u} : \bar{\Omega} \times]0, T] \times \mathscr{I} \times \mathscr{J} \to \mathbb{R}^3,$$

where $\mathscr{I} = [\mathbf{u}_0^-, \mathbf{u}_0^+]$ and $\mathscr{J} = [\dot{\mathbf{u}}_0^-, \dot{\mathbf{u}}_0^+]$ represent the considered intervals of variation of initial boundary conditions, $\mathbf{u}_0$ and $\dot{\mathbf{u}}_0$. This makes it necessary to define a new (triply-) weak form where:

$$a(\mathbf{w}, \mathbf{u}) = \int_{\mathscr{I}} \int_{\mathscr{J}} \int_{\Omega} \nabla^s \mathbf{w} : \mathbf{C} : \nabla^s \mathbf{u}\ d\Omega d\dot{\mathbf{u}}_0 d\mathbf{u}_0,$$

$$(\mathbf{w}, \mathbf{f}) = \int_{\mathscr{I}} \int_{\mathscr{J}} \int_{\Omega} \mathbf{w}\mathbf{f}\ d\Omega d\dot{\mathbf{u}}_0 d\mathbf{u}_0,$$

$$(\mathbf{w}, \mathbf{h})_{\Gamma} = \int_{\mathscr{I}} \int_{\mathscr{J}} \int_{\Gamma_t} \mathbf{w}\mathbf{h}\ d\Gamma d\dot{\mathbf{u}}_0 d\mathbf{u}_0.$$

In order to solve such a high-dimensional problem (a straightforward approach by meshing the entire parametric space would not be possible due to the so-called curse of dimensionality, arising to an enormous number of degrees of freedom), PGD methods construct an approximation to the solution as a finite sum of separable functions,

$$\mathbf{v}^h(\mathbf{x}, t, \mathbf{u}_0, \dot{\mathbf{u}}_0) = \left[\sum_{i=1}^{N} \mathbf{F}_i(\mathbf{x}) \circ \mathbf{G}_i(\mathbf{u}_0) \circ \mathbf{H}_i(\dot{\mathbf{u}}_0) \right] \circ \mathbf{d}(t), \tag{6}$$

where the nodal coefficients $\mathbf{d}(t)$ carry out all the time-dependency of the solution and the symbol "$\circ$" stands for the entry-wise Hadamard or Schur multiplication of vectors. PGD computes these separable functions by first linearizing the non-linear problem (since we seek for a product of functions) by employing your favorite linearization technique (usually fixed-point algorithms, but also Newton or quasi-Newton methods are equally possible). PGD computes one sum at a time, then one product at a time, see [7], for instance.

The very last detail in the implementation is to search for an approximation not for the whole time interval of the problem, $]0, T]$, but for $]0, \triangle t]$:

$$\mathbf{v} : \bar{\Omega} \times]0, \triangle t] \times \mathscr{I} \times \mathscr{J} \times [h^-, h^+] \to \mathbb{R}^3,$$

where $\triangle t$ represents the necessary time to response prescribed by the particular envisaged application. For instance, for haptic feedback it has been already mentioned that a physical sensation of touch needs for some 500 Hz to 1 kHz feedback rate. This means that $\triangle t = 0.001$ s. This value $\triangle t$ is not the necessary time step to achieve stability in the time integration chosen (that can be smaller if needed), although it can be coincident (and will be for all the examples shown hereafter).

But the space of initial conditions, if approximated by finite elements, needs for a very large number of degrees of freedom (three velocity components and three displacements per node of the model). Our approach includes the projection of this subspace into another one, conveniently reduced by employing POD techniques. The resulting technique is a sort of black-box integrator that, given the conditions at time step t as initial conditions, provides the method with the resulting displacement and velocity fields at time $t + \triangle t$.

Simulating again liver palpation, a ramp load of 5 N is applied at a particular point of the liver surface during a period of 0.25 s, and then released during other 0.25 s. The liver is then left vibrating free. Even if the liver tissue is well known to possess some kind of viscoelastic properties, these have been neglected. The purpose of this example is not to obtain an extremely realistic simulation from a physiological point of view, but to show the performance of the technique. In particular, the influence of the number of modes chosen to parametrize the space of initial conditions on the long-term behaviour of the solution. To this end, a reference solution has been computed by employing a HHT time integrator [10] and standard finite elements. POD modes have been extracted from this reference solution to construct the basis for the combined PGD–POD integrator.

It can be noticed that, in the idealized situation of absence of any type of damping, after the load release, the liver continues vibrating indefinitely. A PGD–POD solution has been computed by employing 1, 3, and 7 modes in the basis of the space of initial conditions. It can be noticed from Fig. 4 that increasing the number of modes, as expected, provides converging results towards the reference solution. In fact, it can be noticed how the reduction in the number of degrees of freedom,

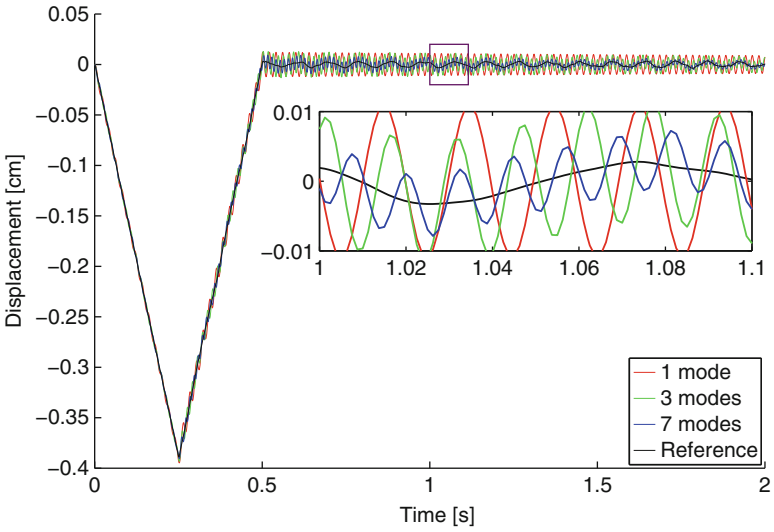

Fig. 4 Response of the liver for a peak load. Reference (FE) results, and PGD results with basis composed by 1, 3, and 7 modes

very much like in classical model order reduction, eliminates high frequencies from the solution (those with the lowest content in energy) and therefore oscillations around the reference solution can be observed. The richer the basis is, the smaller the amplitude of these oscillations and the smaller their period.

3 Conclusions

In our recent research work a method for real-time simulation of computational surgery has been developed that makes intensive use of computational vademecums. These have proven how many aspects of on-line simulations can be pre-computed off-line and employed very efficiently at extremely high feedback rates. In this chapter we have reviewed some of our latest works in the field [7, 9], detailing how this technique can be employed for non-linear constitutive equations (and strain measures) and also for solid dynamics.

References

1. Ammar, A., Chinesta, F., Diez, P., Huerta, A.: An error estimator for separated representations of highly multidimensional models. Comput. Methods Appl. Mech. Eng. **199**(25–28), 1872–1880 (2010)
2. Alfaro, I., Gonzalez, D., Bordeu, F., Leygue, A., Ammar, A., Cueto, E., Chinesta, F.: Real-time in silico experiments on gene regulatory networks and surgery simulation on handheld devices. J. Comput. Surg. 1, 1–1 (Open access)

3. Bernoulli, C.: Vademecum des Mechanikers. Cotta, Stuttgart (1836)
4. Bro-Nielsen, M., Cotin, S.: Real-time volumetric deformable models for surgery simulation using finite elements and condensation. Comput. Graph. Forum **15**(3), 57–66 (1996)
5. Chinesta, F., Cueto, E.: PGD-Based Modeling of Materials, Structures and Processes. Springer International Publishing, Switzerland (2014)
6. Chinesta, F., Ammar, A., Cueto, E.: Recent advances in the use of the Proper Generalized Decomposition for solving multidimensional models. Arch. Comput. Methods Eng. **17**(4), 327–350 (2010)
7. Chinesta, F., Leygue, A., Bordeu, F., Aguado, J.V., Cueto, E., Gonzalez, D., Alfaro, I., Ammar, A., Huerta, A.: PGD-based computational vademecum for efficient design. Optimization and control. Arch. Comput. Methods Eng. **20**(1), 31–59 (2013)
8. Geomagic: OpenHaptics Toolkit. 3D systems – Geomagic solutions, Morrisville (2013)
9. Gonzalez, D., Cueto, E., Chinesta, F.: Real-time direct integration of reduced solid dynamics equations. Int. J. Numer. Methods Eng. **99**(9), 633–653 (2014)
10. Hilber, H.M., Hughes, T.J.R., Taylor, R.L.: Improved numerical dissipation for time integration algorithms in structural dynamics. Earthq. Eng. Struct. Dyn. **5**, 283–292 (1977)
11. Joldes, G.R., Wittek, A., Miller, K.: Real-time nonlinear finite element computations on {GPU} – application to neurosurgical simulation. Comput. Methods Appl. Mech. Eng. **199** (49–52), 3305–3314 (2010)
12. Miller, K., Joldes, G., Lance, D., Wittek, A.: Total lagrangian explicit dynamics finite element algorithm for computing soft tissue deformation. Commun. Numer. Methods Eng. **23**(2), 121–134 (2007)
13. Niroomandi, S., González, D., Alfaro, I., Bordeu, F., Leygue, A., Cueto, E., Chinesta, F.: Real-time simulation of biological soft tissues: A PGD approach. Int. J. Numer. Methods Biomed. Eng. **29**(5), 586–600 (2013)
14. Niroomandi, S., Gonzalez, D., Alfaro, I., Cueto, E., Chinesta, F.: Model order reduction in hyperelasticity: a proper generalized decomposition approach. Int. J. Numer. Methods Eng. **96**(3), 129–149 (2013)

Data-Guided Growth and Remodeling Model of Abdominal Aortic Aneurysm Accounting for the Bio-chemical Effects of Intraluminal Thrombus

Mehdi Farsad, Byron A. Zambrano, and Seungik Baek

1 Introduction

Most of the abdominal aortic aneurysms (AAA) include an intraluminal thrombus layer (ILT). In general, the ILT thickens with increase in the AAA volume [33]. While researchers are not unanimous about the mechanical effects of the ILT on the AAA expansion, the majority of them agree that ILT can bio-chemically weaken the AAA wall by activating proteolytic activity on the AAA wall located beneath the ILT [20, 29, 31]. To better understand the effect of the ILT on an expanding AAA's biomechanics, a growth and remodeling (G&R) computational framework that brings into account and updates the bio-chemical effects of the ILT on the AAA will be of great interest.

The AAA formation promotes favorable conditions for the deposition of the activated platelets on the internal AAA wall. An evolving fibrin mesh is then formed on the internal side of the AAA wall to hold the platelets, erythrocytes, leukocytes, and some other proteins [32]. This fibrin mesh stabilizes itself by forming more fibers and crosslinks on the ILT surface in direct contact with the blood [10]. Consequently, the internal regions of the ILT get denser while the voids between the crosslinked fibrins increase by approaching the arterial wall [25]. As the ILT gets thicker, three different layers are developed in the ILT, namely, luminal, medial, and abluminal layers from aortic lumen towards the AAA wall [30, 32].

M. Farsad
Department of Engineering Technology, West Virginia University Institute of Technology, Montgomery, WV 25136, USA

B.A. Zambrano • S. Baek (✉)
Department of Mechanical Engineering, Michigan State University, East Lansing, MI 48824, USA
e-mail: sbaek@egr.msu.edu

B. Doyle et al. (eds.), *Computational Biomechanics for Medicine*,
DOI 10.1007/978-3-319-15503-6_2

Some studies have suggested that the presence of ILT would have an impact on the AAA growth and consequently rupture [12, 16]. In fact, it has been observed that the probability to accumulate ILT increases as the AAA diameter increases. ILT accumulates eccentrically mostly at the anterior side of an AAA. However, it has been reported that AAA rupture mostly occurs at the posterior side [8]. Recently, Doyle et al. [4] used CFD and longitudinal CT data (from four time points) to show ILT development and expansion in AAA. In addition, Zambrano et al. [33] reported in a study from patients longitudinal CT studies that ILT accumulation rate would relate in a linear manner with the AAA expansion rate. They calculated these rates by measuring the changes in volume between two consecutive CT scans of ILT and AAA, respectively.

The bio-chemical effect of ILT on the AAA wall is led by the proteolytic activities accompanied by the active proteolytic enzymes found in the ILT. The active proteolytic enzymes, such as MMP-2, MMP-8, MMP-9, MPO, uPA, and LE, contribute to the weakness of the AAA walls covered by ILT [31]. These enzymes degrade AAA wall elastin and collagen fibers as they change and reduce the smooth muscle cells and the collagen fiber formation, respectively [7, 20]. These proteases are mainly released by inflammatory cells such as neutrophil and polymorphonuclear leukocytes [6]. The inflammatory cells are trapped between the fibrillar network of the luminal layer of the ILT during the ILT formation [7]. While the medial and abluminal layers of the ILT have significant permeability due to their connected large canaliculi [1], the inflammatory cells are found only up to a depth of 1.0 cm in the luminal side of the ILT [2]. The inflammatory cells trapped in the luminal layer release proteolytic enzymes gradually after the ILT is formed [7]. Since the luminal layer mainly contains active proteolytic enzymes, it is faced to more probability of proteolytic activity that results in a weaker wall. This may be the reason that the AAA ruptures have been reported around the areas with thin ILTs.

On the other hand, the oxygen delivered to the AAA wall through the ILT decreases owing to the ILT's limited diffusion [1, 27]. Hence, when the ILT becomes thicker, it may cause hypoxia. In this case, the oxygen delivered from the lumen through the ILT to the AAA wall decreases significantly resulting in the low oxygen concentration. As a result, new vessels (neo-vessels) are formed in the ILT near the AAA wall [28]. Neo-vessels are found as the main sources of inflammatory cells which, by themselves, are the sources of proteolytic enzymes. In addition, mast cells, which are found abundantly around the neo-vessels, activate the proteolytic enzymes leading to inflammation, degradation, and finally weakness of the AAA wall located beneath a thick ILT [15, 21]. As a result, the phenomenon of oxygen loss in the AAA wall beneath a thick ILT (called hypoxia) leads to the AAA wall weakness not by the proteolytic enzymes being delivered to the wall from the luminal layer but because of the secondary effect of hypoxia explained above.

In this paper, a bio-chemomechanical model is developed for taking into account the effect of proteolytic activity and hypoxia (caused by ILT) on a growing AAA. The approach is, however, phenomenological in that the chemical effects of proteolytic activities and hypoxia cause G&R of aneurysmal wall. The model then uses the patients' data including the AAA's maximum diameter, expansion, and the

rate of expansion so that the data guide for computational model to qualitatively estimate the model parameters. Retrospective data of longitudinal CT scans were taken from several patients, whereas most of the CT scans include ILT, and the G&R model simulation is compared with the patients' data.

2 Methods

To account for the bio-chemical effects of the ILT on the AAA progression, we present a model by modifying an axisymmetric finite element G&R computational framework originally developed by [35]. In this model, we capitalize on the bio-chemical effects that ILT contributes on the AAA wall degradation and expansion. Although many researchers have previously investigated the mechanical effects of the ILT [3, 14, 17], the interstitial pressure of the ILT can be transferred to the aneurysmal wall [5, 18, 22] since the thrombus is composed of a porous material. The mechanical effect of ILT is not considered in this paper.

The AAA wall is assumed to consist of three incompressible solid constituents: elastin (an isotropic solid), smooth muscle (oriented circumferentially), and four collagen fiber families (oriented anisotropically in the AAA wall based on an optimization method [34]). The AAA is initiated by loss of elastin in the aorta wall. While the lost elastin cannot be generated again in an adult's tissue, smooth muscle and collagen fibers are continuously degraded and regenerated in a stress mediated regime.

In an AAA without an ILT, the rate of smooth muscle or collagen fiber mass production per unit reference area of the AAA wall is given by

$$m_R^i(t) = \frac{M_R^i(t)}{M_R^i(0)} m_b^i \left(K_\sigma^i \frac{\sigma^i(t) - \sigma_h^i}{\sigma_h^i} + 1.0 \right), \tag{1}$$

where the superscript $i = c, m$ denotes collagen fiber and smooth muscle, respectively, K_σ^i represents a scalar value that controls the sensitivity of the mass production of constituent i to a scalar value of the membrane stress $\sigma^i(t)$, and m_b^i is the basal rate of mass production of constituent i. Also, $M_R^i(t)$ and σ_h^i denote mass density at time t and homeostatic membrane stress for the constituent i.

Indeed, the strain energy of constituent i at time t per unit reference area, $W^i(t)$, is given by:

$$W^i(t) = M_R^i(0) Q^i(t) \Psi^i(0) + \int_0^t m_R^i(\tau) q^i(\tau, t) \Psi^i(\tau) d\tau, \tag{2}$$

where Ψ^i denote strain energy of constituent i per unit mass, Q^i is the mass fraction of constituent i generated at time zero and still exists at time t, and survival function q^i is the mass fraction of constituent i generated at time τ and still survives at time t.

The following equation is commonly used for survival function of constituent i in absence of ILT:

$$q^i(\tau,t) = \begin{cases} \exp\left[-\int_\tau^t \kappa^i(s)ds\right] & t-\tau \le a^i_{\max} \\ 0 & t-\tau > a^i_{\max}, \end{cases} \tag{3}$$

where $a^i_{\max}$ represents the maximum time that constituent i may survive and $\kappa^i(s)$ is a function of mechanical contribution of the artery's wall such as wall shear stress (WSS), circumferential stress, or stretch accounting for the rate of degradation of constituent i. The expression introduced in [26] is used such that:

$$\kappa^i(s) = \kappa^i_b + \kappa^i_\zeta \left(\frac{\zeta^i(s) - \zeta^i_h}{\zeta^i_h}\right)^2, \tag{4}$$

where ζ^i and ζ^i_h denote tension in constituent i and its homeostatic value, respectively. In addition, κ^i_b and κ^i_ζ represent the basal rate of degradation of constituent i and the sensitivity of the rate of degradation to the stretch of constituent i, respectively.

Aforementioned in the introduction, the ILT may lead to increased degradation and/or decreased production of smooth muscle cells and collagen fibers in the AAA wall. This process is done by the proteolytic enzymes released by the inflammatory cells. Here we divide this process into two categories: first, the inflammatory cells trapped in the luminal layer of the ILT release proteolytic enzymes up to a depth of about 1.0 cm in the luminal side of the ILT (we call it primary proteolytic activity), and second, in case of forming a thick ILT, the oxygen content near the AAA wall decreases significantly and, as a result, neo-vessels are formed near that area. Neo-vessels are known as the sources of inflammatory cells which, by themselves, release proteolytic enzymes. Indeed, mast cells, which are found in the vicinity of the neo-vessels, activate the proteolytic enzymes (we account for this secondary proteolytic activity happening because of hypoxia).

The significance of the primary proteolytic activity depends on the concentration of active proteolytic enzymes in the AAA wall beneath the ILT (C^p). Similarly, the severity of proteolytic activity due to hypoxia depends on the oxygen amount (C^{O_2}) delivered to the AAA wall from lumen through the ILT such that the more loss in the oxygen content leads to the more proteolytic activity. Accordingly, the concentration of active proteolytic enzymes in an AAA wall is given by C^p_h and $C^{O_2}_h$ in absence of the ILT. Beneath the ILT, the oxygen concentration in the lumen, the following equations give the modified versions of Eqs. (1) and (4) for the final rate of production and degradation of constituent i accounting for the effect of both primary and secondary proteolytic activity:

$$m^i_R(t) = \frac{M^i_R(t)}{M^i_R(0)} m^i_b \left(K^i_\sigma \frac{\sigma^i(t) - \sigma^i_h}{\sigma^i_h} - K^i_p \frac{C^p - C^p_h}{C^p_h} + K^i_s \frac{C^{O_2} - C^{O_2}_h}{C^{O_2}_h} + 1.0\right), \tag{5}$$

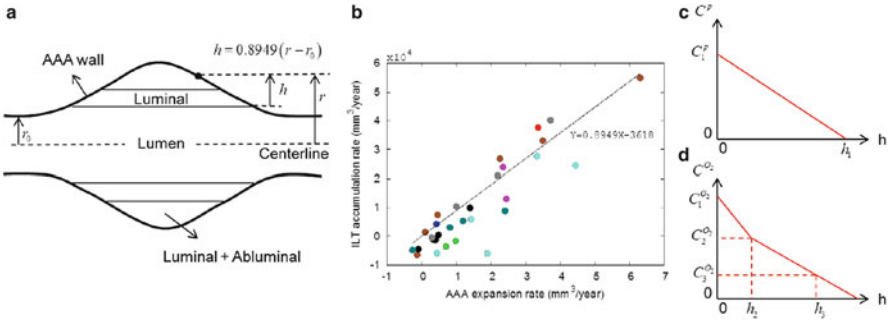

Fig. 1 (**a**) Schematic view of an AAA including ILT. (**b**) The plot for the correlation between the ILT accumulation rate and the rate of AAA expansion. These rates were defined as the changes of volumes between two consecutive scans over that time interval. Each color refers to longitudinal CT data of a different patient [33]. (**c**) The changes of active proteolytic enzymes in the ILT's depth. (**d**) The changes of oxygen concentration in the ILT's depth

$$\kappa^i(s) = \kappa_b^i + \kappa_\zeta^i \left(\frac{\zeta^i(s) - \zeta_h^i}{\zeta_h^i} \right)^2 + \kappa_p^i(s) \frac{C^p - C_h^p}{C_h^p} - \kappa_s^i \frac{C^{O_2} - C_h^{O_2}}{C_h^{O_2}}, \tag{6}$$

where K_p^i and $\kappa_p^i(s)$ denote parameters representing the sensitivity of the production and degradation of constituent i to the primary proteolytic activity, respectively; where K_s^i and $\kappa_s^i(s)$ represent the sensitivity of the production and degradation of constituent i to the secondary proteolytic activity (due to hypoxia), respectively.

Since the number of inflammatory cells reduces linearly with the ILT thickness in the luminal side of the ILT [1], we assume that C^p also is reduced linearly in luminal layer such that it vanishes in depth of h_2 (see Fig. 1). Furthermore, assume that each ILT layer is made of a homogeneous material and C^{O_2} in the ILT changes linearly in the depth of ILT but the rate of change differs in each layer due to different permeabilities of the ILT layers. We assume the same material properties for the medial and abluminal layers. As a result, the changes of C^{O_2} versus the ILT depth takes the multi-line shape depicted in Fig. 1c regarding less permeability in the luminal layer due to its dense cross linked fibrillar matrix [1, 11, 19, 24, 25].

Furthermore, the thickness of ILT at each point on the AAA wall is estimated based on the recent clinical study performed by Zambrano et al. [33] on studying the rate of ILT formation as a function of the AAA geometry from longitudinal CT studies of patients. They showed by calculating the changes of ILT and AAA outer volumes between two consecutive scans over time that there is a positive correlation between the ILT accumulation rate and the AAA expansion rate with $\alpha = 0.8949$, where α is the slope of the trendline (see Fig. 1b). Accordingly, for an axisymmetric model of AAA, the thickness of the ILT (h) at each point on the AAA wall located

Table 1 The values, units, and references of the parameters used in Eqs. (5) and (6), and Fig. 1c, d

C_1^p	C_h^p	$C_1^{O_2}$	$C_2^{O_2}$	$C_3^{O_2}$	$C_h^{O_2}$	h_1	h_2	h_3	K_σ^i	κ_b^i	κ_ζ^i
5.4	0.2	100	60	20	100	0.8	1.0	2.5	0.05	0.02	0
(ng/g)	(ng/g)	(%)	(%)	(%)	(%)	(cm)	(cm)	(cm)	–	(s^{-1})	–
[6]	[6]	[28]	[28]	[28]	[28]	[6]	[28]	[28]	[13]	[13]	–

For all other parameter values, please see [13]

in the radial distance r is estimated by $h = \alpha \cdot (r - r_0)$, where r_0 is the initial radius of the (healthy) aorta. The latter equation is easily obtained by assuming that the stretch of the AAA wall in the axial direction is relatively negligible compared to the changes of the AAA radius r.

The values of the parameters used in the G&R model along with the reference they are taken from are summarized in Table 1.

3 Results

All the AAA G&R simulations in this section are initiated with a loss in the elastin content concentrated at the middle of the aorta.

The sensitivity of an AAA expansion to the parameters $\kappa_s^c = \kappa_s^m = \kappa_s$, related to the degradation of the AAA wall due to hypoxia, and $\kappa_p^c = \kappa_p^m = \kappa_p$, related to the degradation of the AAA wall due to primary proteolytic activity, is illustrated in Fig. 2. When the sensitivity of the model to any of the four parameters κ_p^i, κ_s^i, K_p^i, and K_s^i is studied, all the other three parameters are set to zero. Figure 2a–d shows that by increasing both the parameters κ_s and κ_p the final AAA radius and volume increase significantly as expected. By increasing κ_s, the rate of changes in the AAA radius and volume increases over time (see Fig. 2c). On the other hand, the rate of changes in the AAA radius and volume increases initially and then decreases over time for all the κ_p values (Fig. 2f). The same trend as what shown in Fig. 2 is followed when the sensitivity of the model to the parameters K_p^i and K_s^i is studied (results are not provided because of similarity).

In the last set of simulations, a combination of the parameters (κ_p^i and κ_s^i) is estimated to mimic the same trend of the changes in the AAA volume extracted from the clinical data (see Fig. 3a). The other two parameters (K_p^i and K_p^i) are set to zero. Fig. 3a shows that a similar trend is observed for the changes of the volume of the AAAs with ILT as a function of their maximum radius for the clinical data and the numerical simulation after estimating the parameters. However, Fig. 3b illustrates that although the rates of AAA expansion have at the similar range for the clinical and numerical results, two plots have different trends.

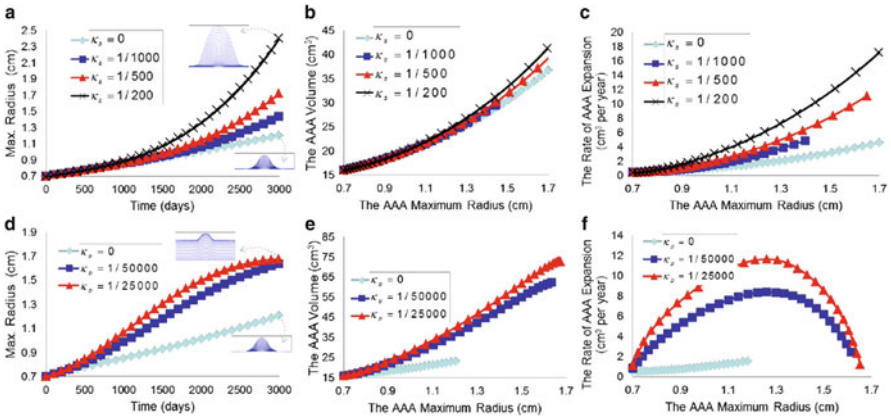

Fig. 2 The sensitivity of the AAA maximum radius, volume, and expansion rate to the parameters (**a**–**c**) κ_s and (**d**–**f**) κ_p introduced in Eq. (6). The sub-figures in (**a**) and (**d**) show qualitative changes of the modeled AAAs without and with ILT during 3,000 days expansion

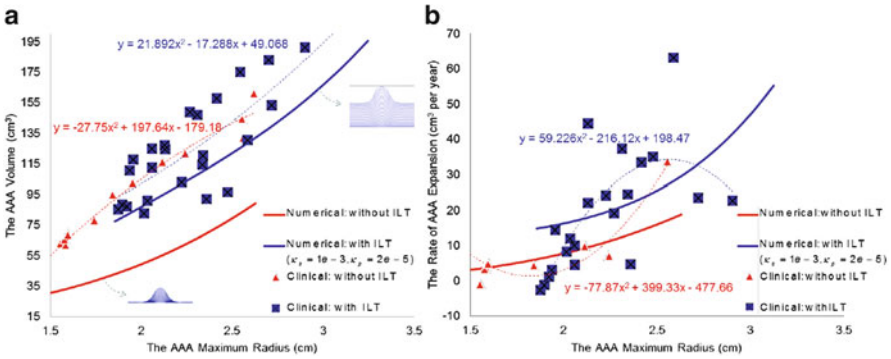

Fig. 3 The changes of the AAA (**a**) volume. (The sub-figures show qualitative changes of the modeled AAAs without and with ILT during 3,000 days expansion.) (**b**) Rate of expansion after estimating the parameters κ_p and κ_s in Eq. (6) using the clinical data. The *dotted lines* show the trend lines for the clinical data

4 Discussion

More than 70 % of the AAAs include a thrombus layer [9, 27]. Bio-chemical and/or mechanical interaction between AAA wall and ILT may affect the AAA expansion and thus increase the risk of rupture.

The ILT affects the AAA expansion by releasing proteases (proteolytic enzymes). These proteolytic enzymes are then activated and lead to the degradation of the elastin and collagen fibers content as well as decreasing the rate of re-synthesis of the smooth muscle cells and collagen fibers. This process finally leads to weakening of the AAA wall and its rupture. The bio-chemical effects of ILT on the AAA

studied in this paper are categorized in two groups. First, the proteolytic activity that happens in the active luminal layer (primary proteolytic activity) and, second, the proteolytic activity that mainly occurs in the AAA wall located beneath a thick ILT because of the secondary effect of hypoxia (secondary proteolytic activity).

The primary proteolytic activity is performed by the activated proteases released by the inflammatory cells trapped in the luminal layer during the ILT formation. Some of the proteases are activated because of being in close contact with the fresh blood. As long as the ILT is thin and made of only the luminal layer, more regions of the AAA wall are in direct contact with this active layer and, thus, are faced to more severe proteolytic activity. When the ILT thickens more, and is layered, only limited parts of the AAA wall (i.e., the AAA shoulders) are faced to severe proteolytic activity that happens in the luminal layer only. This phenomenon may lead to lowering the rate of the AAA expansion compared to the case when the ILT was thin. Our model's simulation results illustrated in Fig. 2d–f are in good agreement with what discussed above. These figures show that (for all values of κ_p and K_p) the AAA initially expands very fast with increasing rate of expansion, but the expansion slows down after a while when the ILT thickens.

The AAA wall beneath a thick ILT is faced to proteolytic activity as the secondary effect of hypoxia (lack of oxygen). The secondary proteolytic activity becomes more severe by the AAA expansion and the ILT thickening due to more significant loss of oxygen in the AAA wall. Figure 2a–c, while verifying what discussed above, shows that the simulated AAAs expansion due to the secondary proteolytic parameters (κ_s and K_s) initially increases with a mild slope (because of low to moderate level of hypoxia) but, then, the rate of AAA expansion speeds up with the ILT thickening and severe hypoxia.

In the last set of simulations, the proteolytic activity parameters affecting the smooth muscle cells and collagen fibers degradation (κ_p and κ_s) are chosen to be estimated such that the simulated AAA's maximum diameter and volume is as close as possible to the patients' data illustrated in Fig. 3. Figure 3a shows that the AAA's volume varies between 55 and 200 cm^3, where the AAA maximum radius varies in the range of 1.5–3 cm. Both the ranges are the same as what observed in the clinical data illustrated in Fig. 3. Nevertheless the trend of the changes are not the same for the rate of AAA expansion (Fig. 3b). The reason can be that there is not enough data in the clinical study specially for the AAA's radius smaller than 1.5 cm, or due to the restrictions that have not been considered in our model, such as the mechanical effects of the ILT on the AAA expansion. The mechanical effect can lead to more resistance against the AAA expansion when the ILT thickens by cushioning the AAA wall. However, the numerical simulation and the patients' data could be closer if a better method was used for parameter estimating (such as what used by Seyedsalehi et al. [23]. They have estimated model parameters considering penalty terms in a cost function).

The model presented in this paper shows the effect of primary and secondary proteolytic activity, due to a growing ILT, on the AAA expansion. The parametric study shows that AAA's radius and volume increase significantly in existence of ILT because of both hypoxia and proteolytic activity. However, the relation between the

AAA volume and its maximum diameter slightly changes due to hypoxia while this relation highly changes because of the proteolytic activity in the luminal layer of the ILT. The simulation results presented in this paper however cannot be expected to perfectly estimate a real AAA expansion over time due to our model's limitations. For example, the mechanical effect of the ILT, which is neglected in this paper, may lead to a completely different trend of the AAA expansion. In addition, most of the AAAs interact with their surrounding tissues such as the spinal column and the vena cava, while these constraints have not been included in the model. Finally our model is an axisymmetric model which may lead to increasing the level of error in estimating an AAA expansion. Approaching the mentioned limitations can be the subject of future research.

Acknowledgements The authors gratefully acknowledge the support by the NIH under R01HL115185 and the NSF under CAREER CMMI-1150376.

References

1. Adolph, R., Vorp, D.A., Steed, D.L., Webster, M.W., Kameneva, M.V., Watkins, S.C.: Cellular content and permeability of intraluminal thrombus in abdominal aortic aneurysm. J. Vasc. Surg. **25**(5), 916–926 (1997)
2. Biasetti, J., Christian G.T., Auer, M., Hedin, U., Fausto, L.: Hemodynamics of the normal aorta compared to fusiform and saccular abdominal aortic aneurysms with emphasis on a potential thrombus formation mechanism. Ann. Biomed. Eng. **38**(2), 380–390 (2010)
3. Bluestein, D., Dumont, K., De Beule, M., Ricotta, J., Impellizzeri, P., Verhegghe, B., Verdonck, P.: Intraluminal thrombus and risk of rupture in patient specific abdominal aortic aneurysm – FSI modelling. Comput. Methods Biomech. Biomed. Eng. **12**(1), 73–81 (2009)
4. Doyle, B.J., McGloughlin, T.M., Kavanagh, E.G., Hoskins, P.R.: From Detection to Rupture: A Serial Computational Fluid Dynamics Case Study of a Rapidly Expanding, Patient-Specific, Ruptured Abdominal Aortic Aneurysm, pp. 53–68. Springer, New York (2014)
5. Fillinger, M.F., Raghavan, M.L., Marra, S.P., Cronenwett, J.L., Kennedy, F.E.: In vivo analysis of mechanical wall stress and abdominal aortic aneurysm rupture risk. J. Vasc. Surg. **36**(3), 589–597 (2002)
6. Folkesson, M., Silveira, A., Eriksson, P., Swedenborg, J.: Protease activity in the multi-layered intra-luminal thrombus of abdominal aortic aneurysms. Atherosclerosis **218**(2), 294–299 (2011)
7. Fontaine, V., Jacob, M.-P., Houard, X., Rossignol, P., Plissonnier, D., Angles-Cano, E., Michel, J.-B.: Involvement of the mural thrombus as a site of protease release and activation in human aortic aneurysms. The Am. J. Pathol. **161**(5), 1701–1710 (2002)
8. Hans, S.S., Jareunpoon, O., Balasubramaniam, M., Zelenock, G.B.: Size and location of thrombus in intact and ruptured abdominal aortic aneurysms. J. Vasc. Surg. **41**(4), 584–588 (2005)
9. Harter, L.P., Gross, B.H., Callen, P.W., Barth, R.A.: Ultrasonic evaluation of abdominal aortic thrombus. J. Ultrasound Med. **1**(8), 315–318 (1982)
10. Houard, X., Leclercq, A., Fontaine, V., Coutard, M., Martin-Ventura, J.-L., Ho-Tin-Noé, B., Touat, Z., Meilhac, O., Michel, J.-B.: Retention and activation of blood-borne proteases in the arterial wall: Implications for atherothrombosis. J. Am. Coll. Cardiol. **48**(9)(Suppl.), A3–A9 (2006)

11. Julian, D., Scott, A., Prasad, P., Philippou, H., Rashid, S.T., Sohrabi, S., Whalley, D., Kordowicz, A., Tang, Q., West, R.M., Johnson, A., Woods, J., Ajjan, R.A., Ariens, R.A.S.: Clot architecture is altered in abdominal aortic aneurysms and correlates with aneurysm size. Arterioscler. Thromb. Vasc. Biol. **31**(12), 3004–3010 (2011)
12. Kleinstreuer, C., Li, Z.: Analysis and computer program for rupture-risk prediction of abdominal aortic aneurysms. Biomed. Eng. OnLine **5**(1), 19 (2006)
13. Kwon, S.T., Rectenwald, J.E., Baek, S.: Intrasac pressure changes and vascular remodeling after endovascular repair of abdominal aortic aneurysms: Review and biomechanical model simulation. J. Biomech. Eng. **133**, 011011 (2011)
14. Meyer, C.A. Jr., Moore, J.E., Guivier-Curien, C.: Trans-thrombus blood pressure effects in abdominal aortic aneurysms. J. Biomech. Eng. **132**(7), 071005–071005 (2010)
15. Myrnp, M.I., Trosien, J.A., Fontaine, V., Folkesson, M., Kazi, M., Eriksson, P., Swedenborg, J., Hedin, U.: Mast cells associate with neovessels in the media and adventitia of abdominal aortic aneurysms. J. Vasc. Surg. **50**(2), 388–395; Discussion 395–396 (2009)
16. Pappu, S., Dardik, A., Tagare, H., Gusberg, R.J.: Beyond fusiform and saccular: A novel quantitative tortuosity index may help classify aneurysm shape and predict aneurysm rupture potential. Ann. Vasc. Surg. **22**(1), 88–97 (2008)
17. Polzer, S., Bursa, J.: Poroelastic model of intraluminal thrombus in FEA of aortic aneurysm. In: Lim, C.T., Goh, J.C.H. (eds.) 6th World Congress of Biomechanics (WCB 2010). Proceedings of the IFMBE, August 1–6, 2010 Singapore, vol. 31, pp. 763–767. Springer, Berlin (2010)
18. Polzer, S., Gasser, T.C., Swedenborg, J., Bursa, J.: The impact of intraluminal thrombus failure on the mechanical stress in the wall of abdominal aortic aneurysms. Eur. J. Vasc. Endovasc. Surg. **41**(4), 467–473 (2011)
19. Pulinx, B., Hellenthal, F.A.M.V.I., Hamulyák, K., van Dieijen-Visser, M.P., Schurink, G.W.H., Wodzig, W.K.W.H.: Differential protein expression in serum of abdominal aortic aneurysm patients – a proteomic approach. Eur. J. Vasc. Endovasc. Surg. **42**(5), 563–570 (2011)
20. Reeps, C., Pelisek, J., Seidl, S., Schuster, T., Zimmermann, A., Kuehnl, A., Eckstein, H.-H.: Inflammatory infiltrates and neovessels are relevant sources of MMPs in abdominal aortic aneurysm wall. Pathobiology **76**(5), 243–252 (2009)
21. Saarinen, J., Kalkkinen, N., Welgus, H.G., Kovanen, P.T.: Activation of human interstitial procollagenase through direct cleavage of the leu83-thr84 bond by mast cell chymase. J. Biol. Chem. **269**(27), 18134–18140 (1994)
22. Schurink, G.W., van Baalen, J.M., Visser, M.J., van Bockel, J.H.: Thrombus within an aortic aneurysm does not reduce pressure on the aneurysmal wall. J. Vasc. Surg. **31**(3), 501–506 (2000)
23. Seyedsalehi, S., Zhang, L., Choi, J., Baek, S.: Prior distributions of material parameters for Bayesian calibration of growth and remodeling computational model of abdominal aortic wall. In: BMES Annual Meeting, San Antonio, 24 October 2014
24. Takagi, H., Manabe, H., Kawai, N., Goto, S., Umemoto, T.: Circulating lipoprotein(a) concentrations and abdominal aortic aneurysm presence. Interact. Cardiovasc. Thorac. Surg. **9**(3), 467–470 (2009)
25. Tong, J., Cohnert, T., Regitnig, P., Holzapfel, G.A.: Effects of age on the elastic properties of the intraluminal thrombus and the thrombus-covered wall in abdominal aortic aneurysms: Biaxial extension behaviour and material modelling. Eur. J. Vasc. Endovasc. Surg. **42**(2), 207–219 (2011)
26. Valentín, A., Cardamone, L., Baek, S., Humphrey, J.D.: Complementary vasoactivity and matrix remodeling in arterial adaptations to altered flow and pressure. J. R. Soc. Interface **6**, 293–306 (2009)
27. Vorp, D.A.: Biomechanics of abdominal aortic aneurysm. J. Biomech. **40**(9), 1887–1902 (2007)
28. Vorp, D.A., Lee, P.C., Wang, D.H., Makaroun, M.S., Nemoto, E.M., Ogawa, S., Webster, M.W.: Association of intraluminal thrombus in abdominal aortic aneurysm with local hypoxia and wall weakening. J. Vasc. Surg. **34**(2), 291–299 (2001)

29. Vorp, D.A., Wang, D.H., Webster, M.W., Federspiel, W.J.: Effect of intraluminal thrombus thickness and bulge diameter on the oxygen diffusion in abdominal aortic aneurysm. J. Biomech. Eng. **120**(5), 579–583 (1998)
30. Wang, D.H., Makaroun, M., Webster, M.W., Vorp, D.A.: Mechanical properties and microstructure of intraluminal thrombus from abdominal aortic aneurysm. J. Biomech. Eng. **123**(6), 536–539 (2001)
31. Wiernicki, I., Stachowska, E., Safranow, K., Cnotliwy, M., Rybicka, M., Kaczmarczyk, M., Gutowski, P.: Enhanced matrix-degrading proteolytic activity within the thin thrombus-covered wall of human abdominal aortic aneurysms. Atherosclerosis **212**(1), 161–165 (2010)
32. Wilson, J.S., Virag, L., Di Achille, P., Karsaj, I., Humphrey, J.D.: Biochemomechanics of intraluminal thrombus in abdominal aortic aneurysms. J. Biomech. Eng. **135**(2), 021011 (2013)
33. Gharahi, H., Zambrano, B., Lim, C.-Y., Choi, J., Lee, W., Baek, S.: An alternative method to measure the diameter of abdominal aortic aneurysms using maximally inscribed spheres. In: BMES Conference, San Antonio, 25 October 2014
34. Zeinali-Davarani, S., Raguin, L.G., Vorp, D.A., Baek, S.: Identification of *in vivo* material and geometric parameters of a human aorta: Toward patient-specific modeling of abdominal aortic aneurysm. Biomech. Model. Mechanobiol. **10**, 689–699 (2011)
35. Zeinali-Davarani, S., Sheidaei, A., Baek, S.: A finite element model of stress-mediated vascular adaptation: Application to abdominal aortic aneurysms. Comput. Methods Appl. Mech. Eng. **14**(9), 803–817 (2011)

A Computer Simulation for 3D Vasculature-Based Oxygen Distribution and Tumour Growth

Alice Chapuis and Harvey Ho

1 Introduction

Over the last several decades Cellular Automaton (CA) has become a powerful tool in simulating cell growth (e.g., in [1]), cell–cell interaction and angiogenesis (e.g., in [2]). While the early CA models have been mainly developed for simulations in a 2D domain (see [3] for a review), 3D simulations have also been reported owing to improved computer performance [4, 5]. Amongst the 3D CA models, Düchting and Vogelsaenger used the control theory to manage cell cycles [6]; Kansal et al. modeled a self-organizing brain tumour (glioblastoma multiforme) where the growth of the tumour complies with the Gompertz model [7]. Wise et al. developed a diffuse interface model for avascular tumours and simulated surface tension of cells in a adaptive 3D mesh [8].

In our previous study we used a hybrid CA and continuum model to simulate cancer and normal cell competition in a 2D domain with a background of known oxygen distribution [9]. That work was similar to the model proposed by Alarcon et al. [1] in that at every time step the program simulates the evolution of the two colonies (cancer and normal cells) with a steady oxygen supply. In this study we develop the concepts and computational means in [9] in several aspects. Firstly, we extend the hybrid model from a 2D domain to a 3D domain. Secondly, we consider oxygen consumption (or uptake) by cells, and thirdly we use a different vascular tree growing algorithm. The objective is to develop a computational framework for cancer/normal cell competition and also take into account oxygen metabolism.

A. Chapuis
Department of Fluid Mechanics and Hydraulics, ENSEEIHT, Toulouse, France

H. Ho (✉)
Auckland Bioengineering Institute, University of Auckland, Auckland, New Zealand
e-mail: harvey.ho@auckland.ac.nz

B. Doyle et al. (eds.), *Computational Biomechanics for Medicine*,
DOI 10.1007/978-3-319-15503-6_3

2 Method

2.1 Micro-Vasculature Construction

We consider a domain of size $1 \times 1 \times 1$ mm which is divided into a $100 \times 100 \times 100$ grid. The size of each grid is therefore $\Delta x = \frac{1}{100}\,\text{mm} = 10\,\mu\text{m}$ which is roughly the size of a cell. The domain contains blood vessels which are the sources of oxygen and nutrients. In our previous work the 2D micro-vasculature was generated using a diffusion CA model [9]. In this work we used a constrained constructive optimization (CCO) algorithm to grow the vascular network. This powerful algorithm has been used to simulate vascular network in 2D [10] and also in 3D [11]. The full description of the CCO algorithm is not provided here, but an interested reader can find more information from literature [10, 11].

In brief, the CCO algorithm grows trees in a manner that fulfils the principle of minimum blood volume, i.e., only a minimum necessary amount of blood is required to perfuse a tissue/organ. Practically an input mean flow rate and a global pressure drop need to be defined for the tree. Figure 1 shows a 3D vasculature of 2,000 vessels, with the flow rate at the root vessel being 1.0×10^{-3} ml and the pressure drop being 5 mmHg across the tree. This vasculature will be used in the 3D domain for oxygen diffusion simulation.

2.2 Oxygen Distribution

The transient diffusion equation in 3D can be expressed as [12]:

$$\frac{\partial c(r,t)}{\partial t} = D \cdot \left(\frac{\partial^2 c(x,y,z,t)}{\partial x^2} + \frac{\partial^2 c(x,y,z,t)}{\partial y^2} + \frac{\partial^2 c(x,y,z,t)}{\partial z^2} \right) - k(x,y,z) \tag{1}$$

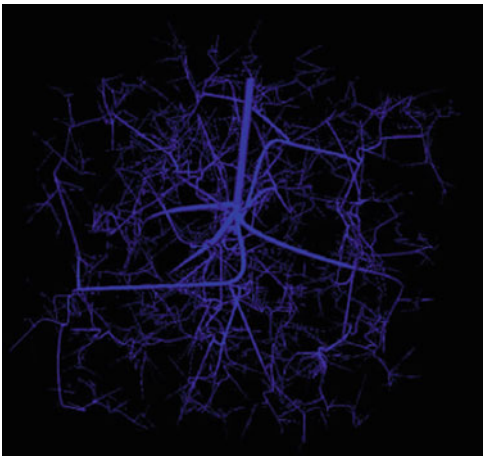

Fig. 1 Micro-vasculature generated using CCO algorithm

where $D = 1.0 \times 10^{-9}\,\mathrm{m^2\,s^{-1}}$ is the diffusion coefficient [12], $c(\mathbf{r}, t)$ is the magnitude of oxygen concentration in the whole domain at location $\mathbf{r}$ and time t. With a finite difference method explicit in time (n) and centered in space (i, j, k) and without considering the oxygen consumption term k, Eq. (1) becomes:

$$C_{i,j,k}^{n+1} = C_{i,j,k}^{n} + \frac{D \cdot \Delta t}{\Delta x^2} \cdot \left\{ C_{i+1,j,k}^{n} + C_{i-1,j,k}^{n} + C_{i,j+1,k}^{n} + C_{i,j-1,k}^{n} + C_{i,j,k+1}^{n} + C_{i,j,k-1}^{n} - 6 \cdot C_{i,j,k}^{n} \right\} \tag{2}$$

As the spatial step was fixed (10 μm), step time has to be chosen to obtain a stable scheme for diffusion. Thus, stability conditions are given by the diffusion number $R = \frac{D * \Delta t}{\Delta x^2} < 0.5$, which gives us:

$$\Delta t < 5.0 \times 10^{-2}\,\mathrm{s}$$

and therefore $\Delta t = 1$ ms was chosen.

A significant difference between the 2D and 3D versions of oxygen diffusion was that the computer memory for the matrix size needs to be considered, especially when floating numbers (default as the data type 64-bit double) are used for the representation of C values for the lattice. In order to reduce the computational cost, the matrix vectorization was used where the concentration at each coordinate $C(i, j, k)$ was identified with an index l and so:

$$C(i, j, k) = C(l) = i + (j - 1) \cdot p + (k - 1) \cdot p \cdot p \tag{3}$$

The internal computation will be made with index l but the result interpretation will be made with indexes i, j, k. A new matrix A was created which will be the basis of the computation and a standard line for A is:

$$\begin{aligned} A(l, :) = [&C(i, j, k)C(i - 1, j, k)C(i + 1, j, k)C(i, j - 1, k) \\ &C(i, j + 1, k)C(i, j, k - 1)C(i, j, k + 1)] \end{aligned} \tag{4}$$

This vectorization scheme resulted in significantly improved computation time. For example, it took around 1 h to compute the first iteration in a conventional matrix form in Matlab. With vectorization it computes much faster: about 60 s for 100 iterations, while saving all the data in a 4D-matrix (three coordinates for space and the last one for time). Without saving the data the computation time for 1,000 iterations was about 450 s.

2.3 Cellular Automata Domain and Rules

To enable cancerous/normal cells to evolve in the 3D domain, we need to define CA *rules*. The first rules were adapted from Alarcon et al. [1]. In brief, a cancerous cell is similar to normal cells in that it may only *proliferate* if oxygen is present in that

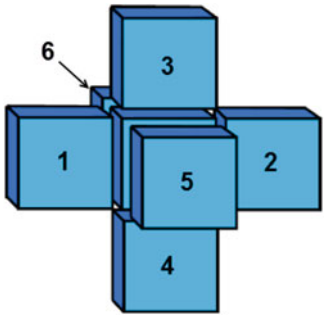

Fig. 2 Neumann neighborhood in 3D: each element has six neighbour elements

element. However a cancerous cell can *survive* and also enter a quiescent state when no oxygen is present in that element. Once a cancerous cell enters a quiescent state, a clock is started and the cell's functions are suspended, including proliferation. The clock is incremented at each time step if no oxygen is present in that centre element. The cell dies once the clock reaches a certain value. However, if oxygen enters the cell at any time, it returns to proliferation state and the clock is reset to zero. The CA model was run on a Neumann lattice, which in three dimensions results in six nearest neighbours (Fig. 2).

Initial proportions of normal and cancer cells in the domain were arranged as 70–30, i.e. more normal cells than cancer cells to enable the development of a normal cell colony. No difference of behaviour between cancer cells and normal cells was considered except the competition rules, which were:

1. If a free element is surrounded by more normal cells than cancerous cells, it would become a normal cell only if there is enough oxygen for the cell to spread into the free element.
2. If a free element is surrounded by an equal number of normal and cancer cells, it would become a cancerous cell, if there is enough oxygen for the cell to spread into the free element.

The above simple rules, when coupled with the diffusion equation, enabled us to simulate different cell growth patterns, as described in Sect. 3.

3 Results

3.1 Oxygen Diffusion in the 3D Domain

The oxygen diffusion based on Eq. (1) and the vasculature of Fig. 1 were solved with the initial condition $C = 0$ kg-mol everywhere in the domain. Figure 3 shows the oxygen distribution isosurfaces when the solution became steady. The concentration gradient from the vasculature to the tissue can be seen from the four isosurfaces in the figure.

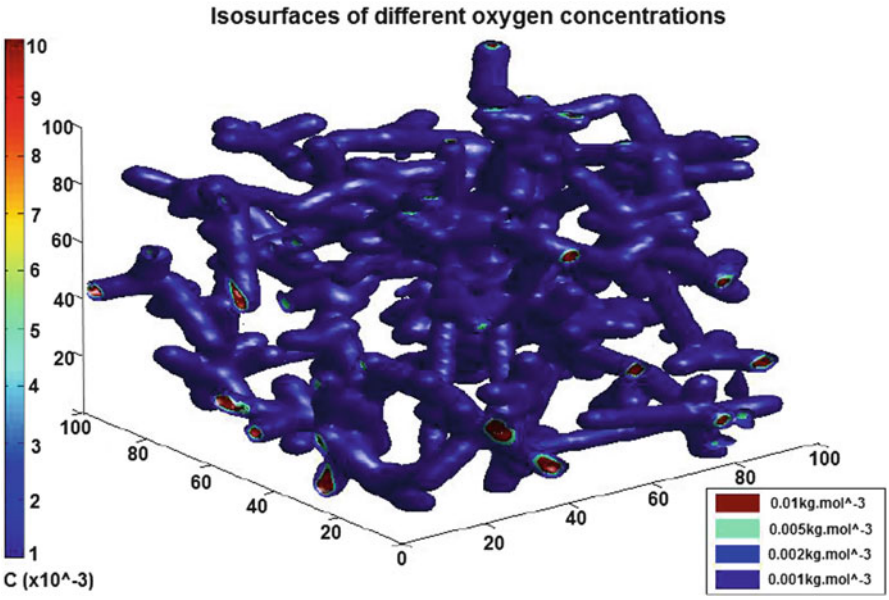

Fig. 3 Isosurfaces of different oxygen concentrations

With an oxygen distribution in the background, the cancer and normal cells may survive and compete with each other. The different growth patterns presented below include:

- the colony at the end of a simulation: cancer cells in red, normal cells in green and vessels in blue
- the evolution of the number of cells during the simulation
- the parameters used in the simulation (diffusion coefficient D and uptake ratio k)

3.2 Cancer/Normal Cell Competition Under Hypoxia

Firstly we considered the scenario where there was an insufficient oxygen supply due to a disrupted vascular network, or the uptake in tumour cells greatly exceeded the supply of the host tissue. We simulated an acute case where a colony started from a normal oxygen concentration distribution shown in Fig. 3, but the oxygen concentration diminished with time due to consumptions from cells. Because of the competition law and the difference of oxygen concentrations needed for proliferation, cancer cells resisted hypoxia better than normal cells.

It can be seen in Fig. 4 that since there was no supply of oxygen from the vessels, the colony decreased and once the oxygen was totally consumed, the cells disappeared. However, under the same initial condition but with different oxygen consumption rates between cancer and normal cell, the initialization enabled normal cell to spread further than cancer cells. However, in the end there were still more cancer cells than normal cells before the disappearance of the colony (Fig. 5).

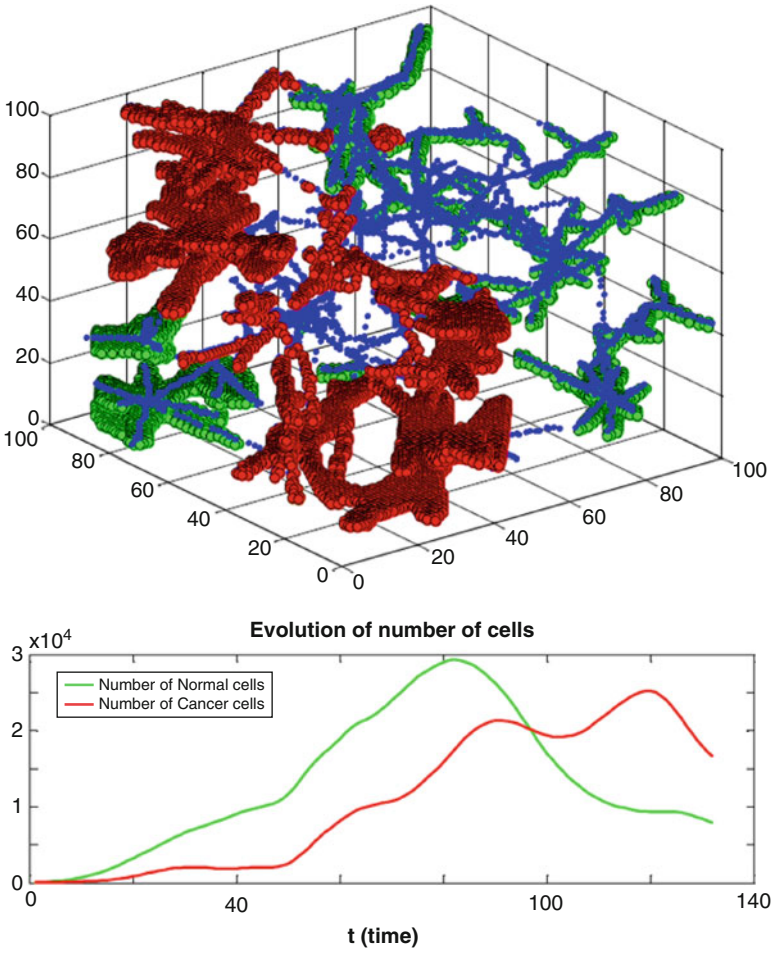

Fig. 4 Hypoxia state simulation. Concentration needed to spread into cells: $C_{\text{normal}} = 0.03\ \text{kg m}^{-3}$, $C_{\text{cancer}} = 0.01\ \text{kg m}^{-3}$. Oxygen consumption rate: $k_{\text{normal}} = 0.1\ \text{g cell}^{-1}\ \text{iteration}^{-1}$, $k_{\text{cancer}} = 0.1\ \text{g cell}^{-1}\ \text{iteration}^{-1}$

3.3 Cancer/Normal Cell Competition Under Steady Oxygen Supply Conditions

We considered another scenario where the vasculature was effectively functioning and the colony received constant oxygen supply. Since the difference remained only in the consumption rates and the initialization was still favourable for normal cells, the normal cells stayed more numerous than cancer cells until the colonies were stable (Fig. 6).

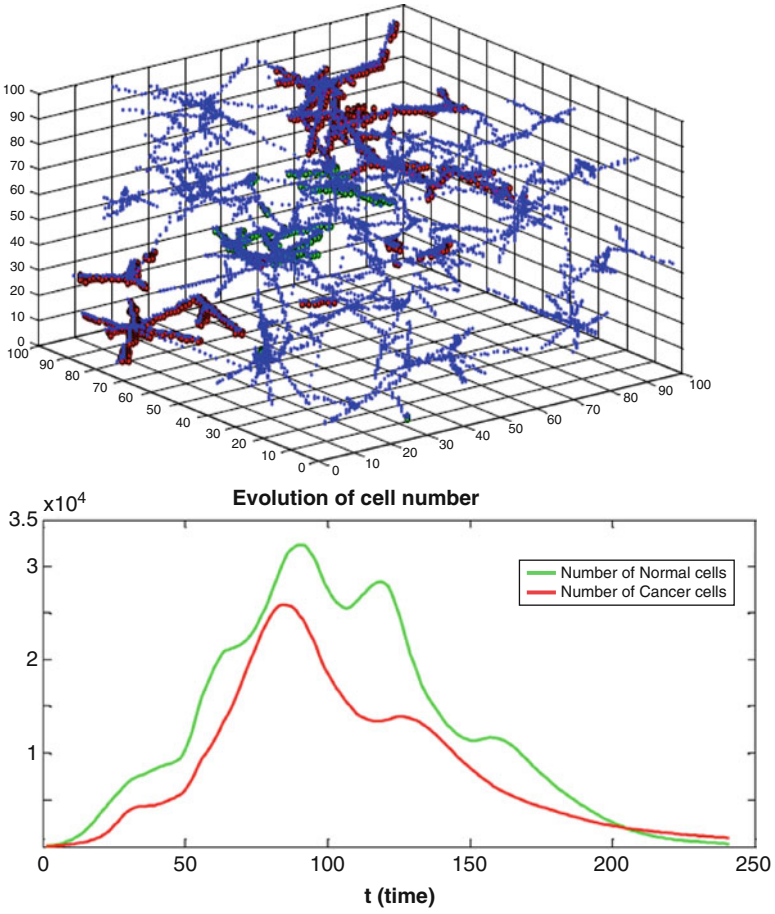

Fig. 5 Hypoxia state simulation. Concentration needed to spread into cells: $C_{\text{normal}} = 0.03\ \text{kg m}^{-3}$, $C_{\text{cancer}} = 0.01\ \text{kg m}^{-3}$. Oxygen consumption rate: $k_{\text{normal}} = 0.21\ \text{g cell}^{-1}\ \text{iteration}^{-1}$, $k_{\text{cancer}} = 0.1\ \text{g cell}^{-1}\ \text{iteration}^{-1}$

Lastly we ran another simulation where the cancer cell growth was strongly favoured due to a much lower concentration needed to spread into adjacent cells, and also a lower uptake rate (Fig. 7). However, the colony of normal cells displayed a resistance to cancer cells in that it remained in the domain. Also note that the tumour cells did not propagate across the whole domain due to low oxygen concentrations in areas far from vessels. Indeed, Folkman observed that tumour cells at a distance of more than 150 μm from capillaries were transformed into necrosis cells [13].

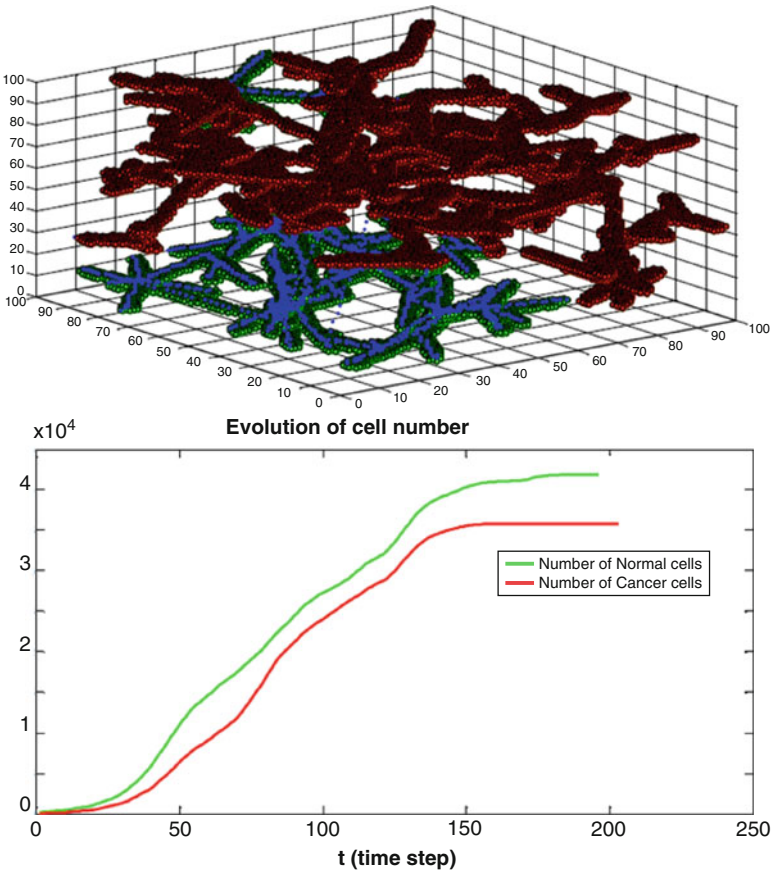

Fig. 6 Oxygenated state simulation. Concentration needed to spread into cells: $C_{\text{normal}} = 0.02\,\text{kg}\,\text{m}^{-3}$, $C_{\text{cancer}} = 0.02\,\text{kg}\,\text{m}^{-3}$. Oxygen consumption rate: $k_{\text{normal}} = 0.21\,\text{g}\,\text{cell}^{-1}\,\text{iteration}^{-1}$, $k_{\text{cancer}} = 0.1\,\text{g}\,\text{cell}^{-1}\,\text{iteration}^{-1}$

4 Discussion

It is well known that a compact solid tumour will grow to a diffusion-limited size, after which it will have to recruit existing vasculature, or acquire a new one through angiogenesis in order to grow further [8, 13]. In the process of metastasis the role of a vascular network is also crucial. In this project we adopted a highly complex 3D vasculature as the source for oxygen diffusion. The goal was to study the growth pattern of a 3D colony of competing normal and cancerous cells by the means of CA, with varying oxygen diffusion and uptake rates occurring at the background. Through the implementation and adjusting of a set of CA rules, evolution of the colony was visualized and compared.

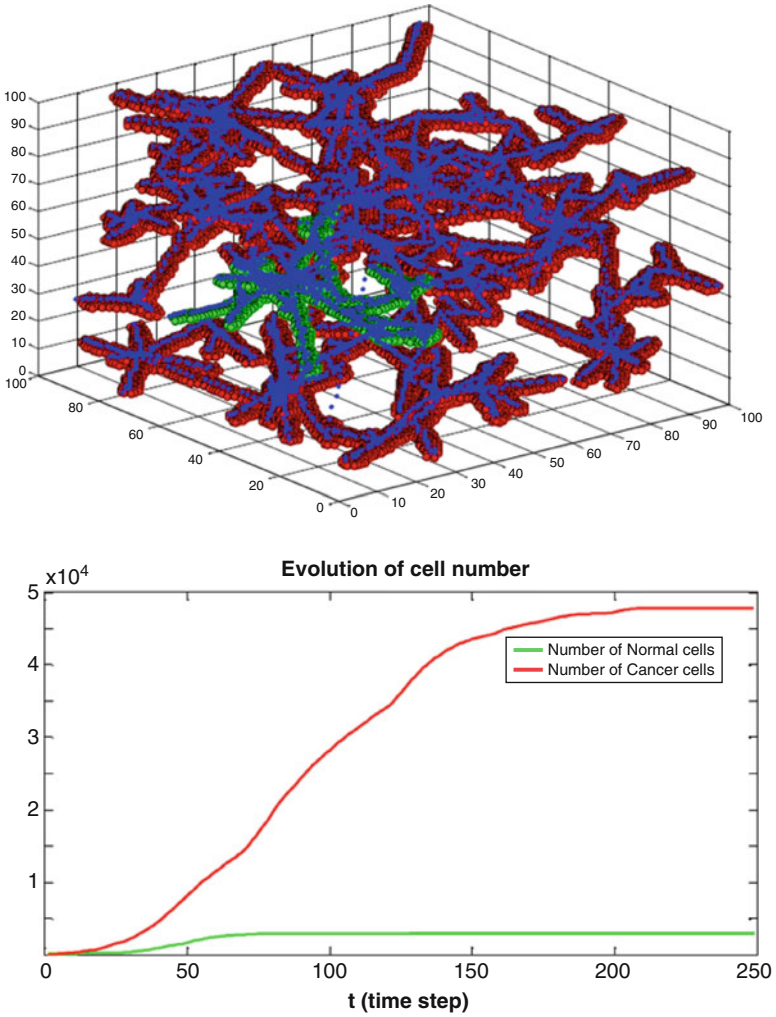

Fig. 7 Oxygenated state simulation. Concentration needed to spread into cells: $C_{\text{normal}} = 0.02\,\text{kg}\,\text{m}^{-3}$, $C_{\text{cancer}} = 0.01\,\text{kg}\,\text{m}^{-3}$. Oxygen consumption rate: $k_{\text{normal}} = 0.21\,\text{g}\,\text{cell}^{-1}\,\text{iteration}^{-1}$, $k_{\text{cancer}} = 0.1\,\text{g}\,\text{cell}^{-1}\,\text{iteration}^{-1}$

The assumptions of the simulations were rather idealistic. Firstly, angiogenesis happened separately from metastasis and so the vasculature was created before the computation; secondly, the initialization was from a random colony of 25 cells (70 % of normal cells and 30 % of cancer cells), located in the centre of the vasculature; Thirdly, the growth coefficient was empirically configured. Future works include incorporation of a vasculature network that would evolve with, and due to, the tissue would greatly increase validity. More specifically, vasculature that responds to growth factors emitted by cancerous tissue would be included.

The spatial scale (1 mm) of the current hybrid CA-continuum model provides an excellent interface for multiscale modelling. Moreover, the current domain configuration ($\times 10^6$ cells of $\sim$1 mm in each dimension) represents the size of some fundamental units of biosystems, e.g., the liver lobule, which has a complex vessel organization. Thus the current framework represents our first effort for ensuing 3D vasculature-based tumour growth models. For example, from a computational perspective it is possible to incorporate more complex CA rules. One of such rules is to allow a cancer cell to divide even when there is no free space around it—the tumour cell mitosis scheme as introduced in [6].

5 Conclusion

In this paper we presented a hybrid CA-continuum method to simulate cancer and normal cell competition in a 3D domain with a complex vasculature. The current work established a flexible framework to incorporate more realistic CA rules and diffusion/uptake parameters.

Acknowledgement We thank Mr. Alexandre Muller for his help in the tree growing CCO algorithm.

References

1. Alarcon, T., Byrne, H., Maini, P.: A cellular automaton model for tumour growth in inhomogeneous environment. J. Theor. Biol. **225**(2), 257–274 (2003)
2. Anderson, A.R.A., Chaplain, M.A.J.: Continuous and discrete mathematical models of tumor-induced angiogenesis. Bull. Math. Biol. **60**, 857–899 (1998)
3. Chopard, B., Droz, M.: Cellular Automata Modeling of Physical Systems. Springer, New York (2012)
4. Moreira, J., Deutsch, A.: Cellular automaton models of tumor development: a critical review. Adv. Complex Syst. **05**(02n03), 247–267 (2002)
5. Byrne, H.M., Alarcon, T., Owen, M.R., Webb, S.D., Maini, P.K.: Modelling aspects of cancer dynamics: a review. Philos. Trans. R. Soc. A: Math. Phys. Eng. Sci. **364**(1843), 1563–1578 (2006)
6. Düchting, W., Vogelsaenger, T.: Recent progress in modelling and simulation of three-dimensional tumor growth and treatment. Biosystems **18**(1), 79–91 (1985)
7. Kansal, A.R., Torquato, S., Harsh, G.R., Chiocca, E.A., Deisboeck, T.S.: Simulated brain tumor growth dynamics using a three-dimensional cellular automaton. J. Theor. Biol. **203**(4), 367–382 (2000)
8. Wise, S.M., Lowengrub, J.S., Frieboes, H.B., Cristini, V.: Three-dimensional multispecies nonlinear tumor growth – i: model and numerical method. J. Theor. Biol. **253**(3), 524–543 (2008)
9. Deacon, N., Chapuis, A., Ho, H., Clarke, R.: Modelling the tumour growth along a complex vasculature using cellular automata. In: Computational Biomechanics for Medicine. Springer, Berlin (2014)

10. Schreiner, W., Buxbaum, P.: Computer-optimization of vascular trees. IEEE Trans. Biomed. Eng. **40**(5), 482–491 (1993)
11. Karch, R., Neumann, F., Neumann, M., Schreiner, W.: A three-dimensional model for arterial tree representation, generated by constrained constructive optimization. Comput. Biol. Med. **29**(1), 19–38 (1999)
12. Shrestha, S.M.B., Joldes, G.R., Wittek, A., Miller, K.: Cellular automata coupled with steady-state nutrient solution permit simulation of large-scale growth of tumours. Int. J. Numer. Methods Biomed. Eng. **29**(4), 542–559 (2013)
13. Folkman, J.: Angiogenesis in cancer, vascular, rheumatoid and other disease. Nat. Med. **1**(1), 27–30 (1995)

Numerical Algorithm for Simulation of Soft Tissue Swelling and Shrinking in a Total Lagrangian Explicit Dynamics Framework

Benjamin Zwick, Grand Roman Joldes, Adam Wittek, and Karol Miller

1 Introduction

Many soft tissue pathologies and their respective treatments are accompanied by swelling or shrinking of the affected area. Examples of swelling include oedema caused by the abnormal accumulation of fluid within the tissue and the mass-effect of tumour growth. Shrinking of tissues can be observed in hydrocephalus and treatments such as osmodiuretics for the reversal of oedema induced swelling.

The biomechanics of swelling and shrinking has been studied in significant detail and models of varying complexity have been suggested. Early studies include lumped parameter models [17] and finite element models with simplified 2D geometry [16]. More recent developments include detailed 3D models based on linear poroelasticity [10], mixture theory [9], models that account for finite deformations [21] and nonlinear material behaviour of the solid phase [1, 2]. Although these models have shown promising results, a significant challenge is presented by the computational cost involved with solving the complex equilibrium equations that arise from the multiphase mixture theory and the limitations of linear poroelastic models. Within the constraints of the operating theatre results are required quickly and need to be computed on commodity hardware. To enable simulations of entire organs undergoing swelling or shrinking there is a need for computationally efficient and robust solution algorithms.

In this paper, we present an efficient algorithm for modelling swelling and shrinking of soft tissues based on the total Lagrangian (TL) formulation of the finite element (FE) method. In the TL formulation the FE equations are formulated with respect to the initial (undeformed) configuration. Swelling and

B. Zwick (✉) • G.R. Joldes • A. Wittek • K. Miller
Intelligent Systems for Medicine Laboratory, The University of Western Australia,
35 Stirling Highway, Crawley, WA 6009, Australia
e-mail: benjamin.zwick@research.uwa.edu.au

B. Doyle et al. (eds.), *Computational Biomechanics for Medicine*,
DOI 10.1007/978-3-319-15503-6_4

shrinking behaviour is introduced by applying a multiplicative decomposition of the deformation gradient to separate the total deformation into swelling/shrinking and elastic components. The swelling/shrinking deformation is applied to the initial reference configuration to obtain a (fictitious) intermediate stress-free configuration. The elastic deformation is applied to the intermediate configuration to obtain the final deformed configuration. A hyperelastic constitutive law is used to model the elastic behaviour of the material. We do not consider the physiological cause of the swelling. Instead, we impose the swelling stretch as a predefined function of time. Clearly, this model cannot be used to make predictions of swelling or shrinking, but it serves as a demonstration of the method used to enforce swelling and shrinking behaviour in the finite element mesh. Physiological models can be introduced at a later stage to define the amount of swelling/shrinking at each point in the mesh.

The discretised equations are solved using explicit time integration. Adaptive dynamic relaxation [8] ensures rapid convergence towards the steady state solution. A computational advantage of the total Lagrangian over the updated Lagrangian formulation is that all derivatives with respect to the spatial coordinates are calculated with respect to the original configuration and can therefore be pre-computed. The advantage of using explicit time integration with dynamic relaxation for modelling the deformation of soft tissues is that very fast computations are possible compared to similar implicit integration schemes. The stable time step for the explicit method is directly related to the elastic modulus of the material. Compared to structural materials such as steel, soft tissues have a low modulus of elasticity, which allows relatively large time steps to be used making the method especially attractive for modelling soft tissue deformations [15].

2 Methods

2.1 Total Lagrangian Formulation of Swelling and Shrinking

A *motion* or deformation of a continuum body $\mathcal{B} \in \mathbb{R}^3$ is a one-to-one (bijective) mapping [4, 12, 19]

$$\boldsymbol{\varphi}_t : \mathcal{B} \rightarrow \mathcal{S}_t \in \mathbb{R}^3, \tag{1}$$

that maps particles $\boldsymbol{X} \in \mathcal{B}$ from the reference configuration $\mathcal{B}$ onto positions

$$\boldsymbol{x} = \boldsymbol{\varphi}_t(\boldsymbol{X}) = \boldsymbol{\varphi}(\boldsymbol{X}, t), \tag{2}$$

in the current configuration $\mathcal{S}_t \subset \mathbb{R}^3$ at time $t \in [0, T]$. A fundamental measure of deformation is the deformation gradient [19]

$$\boldsymbol{F}(\boldsymbol{X}, t) = D\boldsymbol{\varphi}(\boldsymbol{X}) = \partial \boldsymbol{x} / \partial \boldsymbol{X}. \tag{3}$$

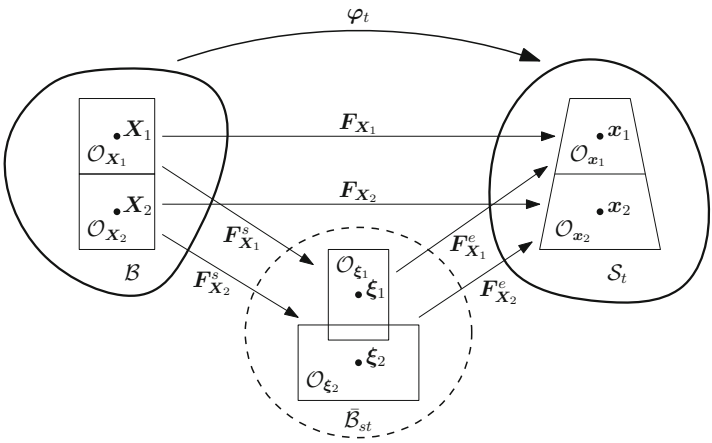

Fig. 1 Multiplicative decomposition of the deformation gradient $\boldsymbol{F} = \boldsymbol{F}^e\boldsymbol{F}^s$ for the motion of two adjacent material points $\boldsymbol{X}_1, \boldsymbol{X}_2 \in \mathcal{B}$ to the spatial positions $\boldsymbol{x}_1, \boldsymbol{x}_2 \in \mathcal{S}_t$

To ensure that the deformation between the spatial and material coordinates is invertible and that the local condition of impenetrability of matter is not violated, the Jacobian determinant must satisfy [19]

$$J(\boldsymbol{X}) = \det[F(\boldsymbol{X})] > 0. \tag{4}$$

Deformation due to swelling or shrinking can be introduced by considering a (fictitious) stress-free intermediate configuration $\bar{\mathcal{B}}_{st}$ between the initial configuration $\mathcal{B}$ and the deformed configuration $\mathcal{S}_t$ (Fig. 1). This concept was first developed by Flory and Rehner [7] for swelling of polymers [5] and is similar to that used for metal plasticity [19], thermal expansion [11] and biological growth [18]. The total deformation $\boldsymbol{F}$ can be separated into elastic $\boldsymbol{F}^e$ and swelling deformation $\boldsymbol{F}^s$ by a local multiplicative decomposition of the form [2, 11, 18]

$$\boldsymbol{F} = \boldsymbol{F}^e\boldsymbol{F}^s. \tag{5}$$

The deformation caused by swelling ($J^s > 1$) and shrinking ($J^s < 1$) is mathematically equivalent; henceforth, the term swelling will be used exclusively to refer to the volume change of the tissue.

It should be understood that $\boldsymbol{F}^e$ and $\boldsymbol{F}^s$ are not proper gradients and that the intermediate configuration is incompatible in a global sense as indicated by the overlapping neighbourhoods $\mathcal{O}_{\boldsymbol{\xi}_1}$ and $\mathcal{O}_{\boldsymbol{\xi}_2}$ of the points $\boldsymbol{\xi}_1, \boldsymbol{\xi}_2 \in \bar{\mathcal{B}}_{st}$ (Fig. 1) [13, 19]. Conceptually, the multiplicative decomposition can be thought of as the disassembly of a finite element mesh (the initial undeformed configuration) and the subsequent application of the local volumetric deformation due to swelling on the individual elements. Unless the swelling deformation is homogeneous, this

intermediate configuration will be incompatible at the boundaries between elements and the elements will no longer "fit together" (more precisely, the intermediate configuration is not a proper configuration because—except for the special case of homogeneous swelling—a bijective mapping between the material particles and $\mathbb{R}^3$ does not exist [6]). Compatibility of the final (deformed) configuration is enforced by reassembling the mesh using the nodal connectivity of the elements. For a formal exposition of the geometrical details, the reader is referred to [6, 12, 13].

For isotropic swelling the swelling deformation gradient can be written as

$$\boldsymbol{F}^s = \lambda_s \boldsymbol{I}, \tag{6}$$

where λ_s is the isotropic swelling stretch and $\boldsymbol{I}$ is the identity tensor. The elastic deformation gradient can then be expressed simply as

$$\boldsymbol{F}^e = \boldsymbol{F}\,(\boldsymbol{F}^s)^{-1} = (\lambda_s)^{-1}\boldsymbol{F}. \tag{7}$$

The total Lagrangian (TL) formulation of the finite element method uses rotation invariant measures of strain (Green–Lagrange strain $\boldsymbol{E}$) and stress (second Piola–Kirchhoff stress $\boldsymbol{S}$) that are calculated with respect to the initial (undeformed) reference configuration $\mathcal{B}$ [3, 4]. The deformations $\boldsymbol{F}^e$ and $\boldsymbol{F}^s$ satisfy the invertibility and impenetrability of matter requirements so that the usual push-forward and pull-back operations can be performed to obtain the stress measures with respect to the configurations $\mathcal{B}$, $\bar{\mathcal{B}}_{st}$ and $\mathcal{S}_t$ [13]. For convenience, the (effective) elastic second Piola–Kirchhoff stress $\boldsymbol{S}^e$ is introduced by the push-forward of $\boldsymbol{S}$ onto the relaxed intermediate configuration $\bar{\mathcal{B}}_{st}$ scaled by the volume ratio J^s. The (total) second Piola–Kirchhoff stress with respect to the initial reference configuration $\mathcal{B}$ can then be expressed as

$$\boldsymbol{S} = J^s(\boldsymbol{F}^s)^{-1}\boldsymbol{S}^e(\boldsymbol{F}^s)^{-T}. \tag{8}$$

In practice, when using hyperelastic materials with the TL formulation of the FE method, $\boldsymbol{S}^e$ is computed using invariants of the elastic deformation gradient $\boldsymbol{F}^e$, whereas the nodal forces are usually computed using $\boldsymbol{S}$ and the total deformation gradient $\boldsymbol{F}$ with respect to the initial reference configuration [3, 4]. This enables the swelling behaviour to be included entirely within the material constitutive model. Standard element formulations can then be used to calculate the element nodal forces and displacements in the usual manner. The Cauchy stress can be obtained using the inverse Piola transformation

$$\boldsymbol{\sigma} = J^{-1}\boldsymbol{F}\boldsymbol{S}\boldsymbol{F}^T. \tag{9}$$

2.2 Constitutive Material Model

At low strain rates the mechanical behaviour of soft tissues can be characterised using a hyperelastic constitutive law [22]. Viscoelastic effects are ignored due to the relatively slow loading speed involved with soft tissue swelling (on the order of a few hours).

Hyperelastic materials are characterised by the existence of a strain energy function $W^e(\boldsymbol{C}^e)$ that relates the deformation to the second Piola–Kirchhoff stress

$$\boldsymbol{S}^e = 2\frac{\partial W^e(\boldsymbol{C}^e)}{\partial \boldsymbol{C}^e}, \tag{10}$$

where $\boldsymbol{C}^e = (\boldsymbol{F}^e)^T \boldsymbol{F}^e$ is the elastic right Cauchy–Green deformation tensor [4]. For hyperelastic materials that are isotropic with respect to the initial, unstressed configuration the strain energy density $W^e(I_1^e, I_2^e, I_3^e)$ can be expressed in terms of the principal invariants $I_1^e = \text{trace}\, \boldsymbol{C}^e$, $I_2^e = \frac{1}{2}\{(\text{trace}\, \boldsymbol{C}^e)^2 - \text{trace}\, (\boldsymbol{C}^e)^2\}$ and $I_3^e = \det \boldsymbol{C}^e$ [4]. The classical (incompressible) neo-Hookean model with strain energy density $W^e(I_1^e) = \mu(I_1^e - 3)$ is based on the assumption that the deformation is isochoric ($J^e = 1$). To account for (slight) compressibility of the material we use the modified strain energy density [24]

$$\bar{W}^e(I_1^e, J^e) = \tfrac{1}{2}\mu\left((J^e)^{-2/3} I_1^e - 3\right) + \tfrac{1}{2}\kappa(J^e - 1)^2, \tag{11}$$

where $J^e = \det \boldsymbol{F}^e$ is used in place of $I_3^e = \det \boldsymbol{C}^e = (J^e)^2$, and μ and κ are the material constants. The behaviour for infinitesimal strains is identical to a linear isotropic elastic model with shear modulus μ and bulk modulus κ. The second Piola–Kirchhoff stress is computed as

$$\boldsymbol{S}^e = \mu(J^e)^{-2/3}\boldsymbol{I} + \left(-1/3\mu(J^e)^{-2/3} I_1^e + \kappa J^e(J^e - 1)\right)(\boldsymbol{C}^e)^{-1}, \tag{12}$$

with respect to the relaxed intermediate configuration $\bar{\mathcal{B}}_{st}$. The strain energy density defined above is equivalent to the neo-Hookean model available in the commercial FE software Abaqus [20] that will be used to verify our algorithm.

The simple hyperelastic model described above serves to demonstrate the effectiveness of the solution procedure. A more realistic model could be used, for example, to account for pressure stiffening due to swelling by defining the stress as a function of the swelling deformation $\boldsymbol{F}^s$ or other solution variables such as the pore pressure.

2.3 Numerical Algorithm for Swelling

Our aim is to determine the configuration of the tissue after swelling or shrinking takes place; therefore, we are interested in the steady state solution. Our algorithm is based on the total Lagrangian formulation of the finite element method and uses

explicit time integration to find the steady state for an artificial dynamic structural equation [3, 4, 15, 23] using adaptive dynamic relaxation [8].

We consider the nonlinear equilibrium equation of structural statics

$$\boldsymbol{f}^{\text{int}}(\boldsymbol{u}) = \boldsymbol{f}^{\text{ext}}, \tag{13}$$

where $\boldsymbol{u}$ is the displacement vector, $\boldsymbol{f}^{\text{int}}$ is the vector of internal nodal forces and $\boldsymbol{f}^{\text{ext}}$ is the vector of externally applied nodal forces. Additional artificial transients are added to (13) to enable the use of the explicit integration procedure. After the inclusion of mass-proportional damping, the equation of motion (13) becomes

$$\boldsymbol{M}\ddot{\boldsymbol{u}} + c\boldsymbol{M}\dot{\boldsymbol{u}} + \boldsymbol{f}^{\text{int}}(\boldsymbol{u}) = \boldsymbol{f}^{\text{ext}}, \tag{14}$$

where the mass matrix $\boldsymbol{M}$ and the mass damping coefficient c are chosen in such a way that rapid convergence towards the steady state solution is achieved [8].

The internal nodal force associated with element $\mathcal{B}_m$ and corresponding to the stress with respect to the initial configuration is given by [4, 19]

$$\boldsymbol{f}^{\text{int},m} = \int_{\mathcal{B}_m} \boldsymbol{F}\,\boldsymbol{S}\,\boldsymbol{B}_0 \, dV, \tag{15}$$

where $\boldsymbol{B}_0$ is the matrix of shape function derivatives. The integration is performed numerically using Gauss quadrature

$$\boldsymbol{f}^{\text{int},m} = \sum_{Q=1}^{n_Q} \boldsymbol{F}\,\boldsymbol{S}\,\boldsymbol{B}_0 J_\xi^0 \bar{w}_Q, \tag{16}$$

where $\bar{w}_Q$ are the quadrature weights and $J_\xi^0 = \det(\partial \boldsymbol{X}/\partial \boldsymbol{\xi})$ is the determinant of the Jacobian between material and element coordinates [4]. For simplicity, we used linear reduced integration tetrahedral elements with a single Gauss point. The nodal forces for each element can therefore be computed as

$$\boldsymbol{f}^{\text{int},m} = \boldsymbol{F}\,\boldsymbol{S}\,\boldsymbol{B}_0 V_0, \tag{17}$$

where V_o is the initial volume of the element [23].

The nodal displacements at integration step $n+1$ are calculated using the central difference formula

$$\boldsymbol{u}_{n+1} = \boldsymbol{u}_n + \beta\,(\boldsymbol{u}_n - \boldsymbol{u}_{n-1}) + \alpha \boldsymbol{M}^{-1}\left(\boldsymbol{f}_n^{\text{ext}} - \boldsymbol{f}_n^{\text{int}}(\boldsymbol{u}_n)\right), \tag{18}$$

$$\alpha = 2\Delta t^2/(2 + c\Delta t), \quad \beta = (2 - c\Delta t)/(2 + c\Delta t),$$

Initialisation:

Compute shape function derivative matrices $\boldsymbol{B}_0$ at each Gauss point ξ_Q.
Choose maximum eigenvalue and scale element densities [8].
Compute the diagonal (constant) mass matrix $\boldsymbol{M}$.
Choose initial minimum eigenvalue and compute iteration parameters [8].
Initialise nodal displacements $\boldsymbol{u}_0 = \boldsymbol{0}$, $\boldsymbol{u}_1 = \boldsymbol{0}$.

Time stepping: (n is the step number)

repeat
  for all elements m **do**
    Gather element nodal displacements.
    Initialise element internal force vector $\boldsymbol{f}_n^{\text{int},m} = \boldsymbol{0}$.
    for all Gauss quadrature points ξ_Q **do**
      Compute total deformation gradient $\boldsymbol{F}_n(\xi_Q) = \boldsymbol{I} + \boldsymbol{B}_0\boldsymbol{u}_n$.
      Compute elastic deformation measures $\boldsymbol{F}_n^e(\xi_Q)$, $\boldsymbol{C}_n^e(\xi_Q)$, I_{1n}^e and J_n^e.
      Compute second Piola–Kirchhoff stress $\boldsymbol{S}_n(\xi_Q)$ using (8).
      Compute internal nodal force contribution $\boldsymbol{f}_n^{\text{int},m}(\xi_Q)$ using (16) or (17) and accumulate in $\boldsymbol{f}_n^{\text{int},m}$.
    end for
    Scatter $\boldsymbol{f}_n^{\text{int},m}$ to global force vector $\boldsymbol{f}_n^{\text{int}}$.
  end for
  Obtain net nodal reaction forces $\boldsymbol{f}_n = \boldsymbol{f}_n^{\text{ext}} - \boldsymbol{f}_n^{\text{int}}$.
  Compute nodal displacements $\boldsymbol{u}_{n+1} = \boldsymbol{u}_n + \beta\,(\boldsymbol{u}_n - \boldsymbol{u}_{n-1}) + \alpha\boldsymbol{M}^{-1}\boldsymbol{f}_n$.
  Enforce Dirichlet (essential) boundary conditions.
  if this is the relaxation stage **then**
    Estimate minimum eigenvalue [8].
    Check maximum eigenvalue of each element and reform $\boldsymbol{M}$ if needed [8].
    Re-compute iteration parameters [8].
  end if
until termination criteria [8] is satisfied.

Box 1: Algorithm for soft tissue swelling and shrinking

where Δt is the integration time step. The damping coefficient c is calculated using an adaptive procedure to obtain optimum convergence towards the steady state solution [8].

We use a lumped (diagonal) mass matrix [3, 4] so that (14) can be decoupled and the solution of a system of algebraic equations at each time step can be avoided. The mass at node I is then given by the Ith entry M_{II} of the diagonal mass matrix $\boldsymbol{M}$. Hence, only the diagonal entries of the mass matrix are needed for the calculation, reducing the storage requirements and making the inversion of $\boldsymbol{M}$ a trivial operation.

The complete algorithm is shown in Box 1. It should be understood that an accurate solution of the dynamic equations cannot be obtained with this method. However, the solution rapidly converges toward the steady state by the use of adaptive mass proportional damping that removes all oscillations within the material.

2.4 FE Model for Algorithm Verification

To verify the proposed algorithm we solved a simple model and compared the results to those obtained using a thermal expansion analogy with the commercial FE code Abaqus [20]. We used a cylinder with diameter and height of 10 cm meshed using 35,598 linear tetrahedral elements and 6,710 nodal points. The nodes on both end surfaces of the cylinder were fully constrained. The swelling stretch was applied using a smooth (3–4–5 polynomial) loading curve [15]

$$\lambda_s(t) = (10 - 15t + 6t^2)t^3, \tag{19}$$

where t is the relative time (varying from 0 to 1). The material parameters of the hyperelastic material model (Sect. 2.2) were chosen to match the behaviour of brain tissue with a mass density of 1,000 kg/m^3, Young's modulus in the undeformed state equal to 3,000 Pa and Poisson's ratio of 0.49 [14].

Abaqus does not offer swelling behaviour of hyperelastic materials so we used the following thermal expansion analogy. The stretch in each principal direction for an unconstrained material undergoing isotropic thermal expansion is

$$\lambda_\theta = (1 + \alpha \Delta\theta), \tag{20}$$

where α is the thermal expansion coefficient and $\Delta\theta$ is the temperature measured with respect to the reference temperature. By setting $\alpha = 1$ the temperature change is related to the isotropic swelling stretch used in our algorithm by

$$\lambda_s \equiv \lambda_\theta = 1 + \Delta\theta. \tag{21}$$

The steady state solution was obtained using the algorithm described in Sect. 2.3 and compared to the Abaqus/Standard [20] static solution.

3 Results

Simulations of constrained swelling and shrinking were performed to verify the proposed algorithm (Sect. 2.4). The results (Fig. 2) show excellent agreement between the proposed algorithm and the Abaqus/Standard [20] static solution for both the reaction forces and the displacements.

4 Conclusions

We developed an algorithm for modelling swelling and shrinking of soft tissues based on the total Lagrangian formulation of the FE method with explicit time integration and adaptive dynamic relaxation used to compute the steady state solution.

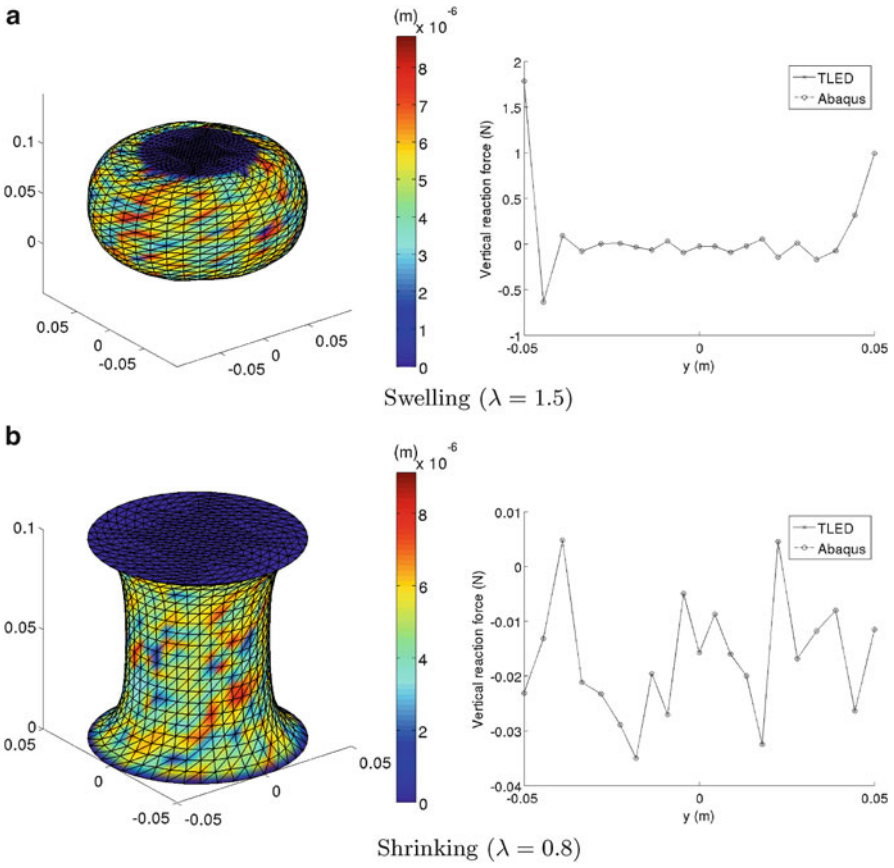

Fig. 2 Differences in displacements (*left*) and vertical nodal reaction forces along a line of nodes on the bottom face (*right*) between our solution method and the equivalent thermal expansion analysis in Abaqus/Standard. The lack of symmetry of the reaction forces is due to the discretisation. (**a**) Swelling ($\lambda = 1.5$); (**b**) shrinking ($\lambda = 0.8$)

The algorithm can easily handle nonlinearities, and is very efficient because it allows pre-computation of important solution parameters and does not require solution of large systems of equations. The use of explicit integration with dynamic relaxation allows the decoupling of the equilibrium equations, leading to an algorithm that is well suited for parallel implementation on graphics processing units (GPUs) for increased computational speed. The algorithm was successfully verified against an established FE code.

Acknowledgements The financial support of the Australian Research Council (Grant No. DP120100402) and NHMRC (Grant No. APP1063986) is gratefully acknowledged.

References

1. Ateshian, G.A., Maas, S., Weiss, J.A.: Multiphasic finite element framework for modeling hydrated mixtures with multiple neutral and charged solutes. J. Biomech. Eng. **135**(11), 111001 (11 pages) (2013)
2. Azeloglu, E.U., Albro, M.B., Thimmappa, V.A., Ateshian, G.A., Costa, K.D.: Heterogeneous transmural proteoglycan distribution provides a mechanism for regulating residual stresses in the aorta. Am. J. Physiol. Heart Circulat. Physiol. **294**(3), H1197–H1205 (2008)
3. Bathe, K.J.: Finite Element Procedures. Prentice Hall, Englewood Cliffs (1996)
4. Belytschko, T., Liu, W.K., Moran, B.: Nonlinear Finite Elements for Continua and Structures. Wiley, Chichester (2006)
5. Duda, F.P., Souza, A.C., Fried, E.: A theory for species migration in a finitely strained solid with application to polymer network swelling. J. Mech. Phys. Solids **58**(4), 515–529 (2010)
6. Dvorkin, E.N., Goldschmit, M.B.: Nonlinear Continua. Springer, Berlin Heidelberg (2006)
7. Flory, P.J., Rehner, J.J.: Effect of deformation on the swelling capacity of rubber. J. Chem. Phys. **12**(10), 412–414 (1944)
8. Joldes, G.R., Wittek, A., Miller, K.: An adaptive dynamic relaxation method for solving nonlinear finite element problems. application to brain shift estimation. Int. J. Numer. Methods Biomed. Eng. **27**(2), 173–185 (2011)
9. Lai, W.M., Hou, J.S., Mow, V.C.: A triphasic theory for the swelling and deformation behaviors of articular cartilage. J. Biomech. Eng. **113**(3), 245–258 (1991)
10. Li, X., von Holst, H., Kleiven, S.: Influences of brain tissue poroelastic constants on intracranial pressure (ICP) during constant-rate infusion. Comput. Methods Biomech. Biomed. Eng. **16**(12), 1330–1343 (2013)
11. Lubarda, V.A.: Constitutive theories based on the multiplicative decomposition of deformation gradient: thermoelasticity, elastoplasticity, and biomechanics. Appl. Mech. Rev. **57**(2), 95–108 (2004)
12. Marsden, J.E., Hughes, T.J.R.: Mathematical Foundations of Elasticity. Prentice-Hall, Englewood Cliffs (1983)
13. Maugin, G.A.: Configurational Forces: Thermomechanics, Physics, Mathematics, and Numerics. Chapman & Hall/CRC, Boca Raton (2010)
14. Miller, K., Chinzei, K.: Mechanical properties of brain tissue in tension. J. Biomech. **35**(4), 483–490 (2002)
15. Miller, K., Joldes, G., Lance, D., Wittek, A.: Total Lagrangian explicit dynamics finite element algorithm for computing soft tissue deformation. Commun. Numer. Methods Eng. **23**(2), 121–134 (2007)
16. Nagashima, T., Shirakuni, T., Rapoport, I.: A two-dimensional, finite element analysis of vasogenic brain edema. Neurol. Med. Chir. **30**(1), 1–9 (1990)
17. Rapoport, S.I.: A mathematical model for vasogenic brain edema. J. Theor. Biol. **74**(3), 439–467 (1978)
18. Rodriguez, E.K., Hoger, A., McCulloch, A.D.: Stress-dependent finite growth in soft elastic tissues. J. Biomech. **27**(4), 455–467 (1994)
19. Simo, J.C., Hughes, T.J.R.: Computational Inelasticity. Springer, New York (1998)
20. Simulia: Abaqus 6.10 Documentation. Dassault Systémes, Providence (2010)
21. Taylor, Z., Miller, K.: Reassessment of brain elasticity for analysis of biomechanisms of hydrocephalus. J. Biomech. **37**(8), 1263–1269 (2004)
22. Wittek, A., Miller, K., Kikinis, R., Warfield, S.K.: Patient-specific model of brain deformation: application to medical image registration. J. Biomech. **40**(4), 919–929 (2007)
23. Wittek, A., Joldes, G., Miller, K.: Algorithms for computational biomechanics of the brain. In: Miller, K. (ed.) Biomechanics of the Brain, Biological and Medical Physics, Biomedical Engineering, pp. 189–219. Springer, New York (2011)
24. Zienkiewicz, O.C., Taylor, R.L., Fox, D.D.: The Finite Element Method for Solid and Structural Mechanics, 7th edn. Elsevier Butterworth-Heinemann, Oxford (2013)

Spatially Weighted Objective Function to Solve the Inverse Elasticity Problem for the Elastic Modulus

Yue Mei and Sevan Goenezen

1 Introduction

Constitutive modeling of human tissues is highly challenging and much research effort is put in this direction to improve current tissue models. The material properties of tissues depend on the selected constitutive model. For example, hyperelastic material models have one or more elastic properties, while viscoelastic material models and poroelastic material models additionally take viscous material properties and material properties characterizing material porosity into consideration [1–3]. In general, the material property values depend not only on the tissue type, e.g., breast tissue, liver tissue, skin, etc., but also on the individual's age, lifestyle, environmental factors, and the pathology of the tissue.

In recent decades, researchers were successful in determining the elastic material properties of soft tissues in vivo and non-invasively which is widely termed as elasticity imaging or elastography. It has shown great potential in detecting and diagnosing breast tumors [4, 5], visualizing stiffness maps of atherosclerotic plaques [6] and the brain. This requires the knowledge of subsurface (interior) displacement fields in the region of interest, which can be measured using imaging modalities such as ultrasound, magnetic resonance imaging (MRI), or computed tomography (CT scan). This displacement field is utilized to solve an inverse problem in elasticity to determine the elastic properties of that particular constitutive model. In its simplest form, strain images (gradient of displacement component in compression direction) were determined and interpreted as the reciprocal of the Young's modulus, assuming

Y. Mei • S. Goenezen (✉)
Department of Mechanical Engineering, Texas A&M University,
College Station, TX 77840, USA
e-mail: sgoenezen@tamu.edu

B. Doyle et al. (eds.), *Computational Biomechanics for Medicine*,
DOI 10.1007/978-3-319-15503-6_5

that the stress is a constant in the entire region of interest. While this is a rough approximation, it has the advantage of quasi-real time application and has clearly shown promising results in clinical applications [7, 8].

Mathematical and computational complexity is involved when solving the inverse problem from the partial differential equations, i.e., the equations of equilibrium, as the problem is highly ill-posed. In [9] the authors solve the inverse problem directly from the equations of equilibrium. This has the disadvantage that derivatives of noisy measured displacement fields are taken, leading to high amplification of errors in the strains and constitutive models [10]. The iterative method utilized in [11–16] minimizes the correlation between a measured displacement field and a computed displacement field under the constrained of the equations of equilibrium. The computed displacement fields satisfy the equations of equilibrium for the current estimate of the elastic properties. While this strategy circumvents taking derivatives of noisy measured displacement fields, it is computationally intensive. The computational cost was reduced in [12, 16] by computing the gradient of the objective function by the adjoint method. Additionally, Tikhonov regularization was utilized to smooth the overall solution of the inverse problem. This method has been extended to accommodate material incompressibility, built in pre-conditioners to improve convergence, and a novel strain energy density function with two elastic properties, which has the advantage of having a deviatoric stress component [12].

We recently observed that the iterative formulation of the inverse problem is sensitive to varying Dirichlet boundary conditions, for example, the solution of the inverse problem is a different one when utilizing uniform displacement boundary conditions versus linearly changing boundary conditions. We realize that this is primarily caused due to the fact that the displacement varies in a wide range spatially, while the objective function minimizes absolute differences between the measured and computed displacement fields. To this end, we provide a new formulation for the objective function and test it on hypothetical data. For simplicity we model the material to be linear and utilize the small strain theory.

2 Methods

We solve the inverse problem in elasticity iteratively by minimizing the correlation between a measured and a computed displacement field under Tikhonov regularization. We assume that the material response is linear and utilize small strain theory in elasticity with time independent (static) deformations. The strong form is given as follows: Find the displacement field $\mathbf{u}$ and the pressure p such that

$$\operatorname{div}(\boldsymbol{\sigma}) = \mathbf{0} \quad \text{in} \quad \Omega \tag{1}$$

$$\mathbf{u} = \mathbf{g} \quad \text{on} \quad \Gamma_g \tag{2}$$

$$\boldsymbol{\sigma} \cdot \mathbf{n} = \mathbf{h} \quad \text{on} \quad \Gamma_h \tag{3}$$

Additionally, we enforce incompressibility as most soft tissues are reported to be nearly incompressible:

$$\mathrm{tr}(\boldsymbol{\varepsilon}) = 0 \text{ in } \Omega \tag{4}$$

Equation (1) represents the equations of equilibrium with Ω the region of interest and $\boldsymbol{\sigma}$ the Cauchy stress tensor. Equations (2) and (3) define the Dirichlet and Neumann boundary conditions, respectively, where $\mathbf{g}$ denotes the prescribed displacement on the Dirichlet boundary Γ_g and $\mathbf{h}$ is prescribed on the Neumann boundary Γ_h with $\mathbf{n}$ being the unit outward normal on that boundary. Additionally it is essential that Γ_h and Γ_g satisfy the following conditions: $\overline{\Gamma_h \cup \Gamma_g}$ define the closed boundary of the region of interest Ω and $\Gamma_h \cap \Gamma_g = \varnothing$. Finally, Eq. (4) enforces the trace of the strain tensor to be zero, i.e., all diagonal components of the strain tensor add up to zero. Throughout this chapter, we will assume plane strain conditions and a linear stress–strain relationship given by

$$\boldsymbol{\sigma} = 2\mu\boldsymbol{\varepsilon} + p\mathbf{I} \tag{5}$$

where μ denotes the shear modulus, p the pressure variable or hydrostatic stress, and $\mathbf{I}$ the 2×2 identity matrix.

It is now straightforward to derive the mixed finite element formulation from Eqs. (1) to (5) which we will also refer to as the forward problem. This will be omitted here and may be reviewed in [12]. Therein, we utilized a stabilized finite element formulation [12, 17], which allows us to use equal order linear triangular elements for the displacement and pressure interpolation, while circumventing the Ladyzenskaya–Babuska–Brezzi conditions.

2.1 Absolute Minimization of Displacement Correlation

In this section we briefly review the inverse problem statement, this is: Find the elastic property distribution μ, such that the objective function

$$F = \frac{1}{2}\sum_{i=1}^{n} w_i \left\| \mathbf{D}\left(\mathbf{u}^i - \mathbf{u}^i_{\text{meas}}\right)\right\|_2^2 + \alpha \int_{\Omega} \sqrt{|\nabla\mu|^2 + c^2}\, d\Omega \tag{6}$$

is minimized under the constraint of the forward elasticity problem. The first term is referred to as the displacement correlation term, where we minimize the discrepancy between a computed, $\mathbf{u}^i$, and measured, $\mathbf{u}^i_{\text{meas}}$, displacement field in the L-2 norm. $\mathbf{D}$ denotes a diagonal matrix which may be defined such that certain displacement components are weighted more than others. This is due to the fact that measured displacement components perpendicular to the ultrasound transducer

axis are much noisier than along the transducer beam. Thus one may choose to weight the displacement component with the higher noise level less than the other displacement component. Furthermore, we observe a summation in Eq. (6) to accommodate n measured displacement fields in the minimization process. The weighting factor, w_i, ensures that displacement fields of different orders contribute equally to the objective function. For all computations in this chapter, we will discard the noisy displacement component and utilize only one displacement field ($n = 1$) to solve the inverse problem in elasticity. The second term is the total variation diminishing regularization term, which acts similar to a penalty term and penalizes oscillations in the shear modulus reconstruction. The regularization factor α weights the regularization term. In general, the regularization factor may be chosen based on Morozov's method or the L-curve method [18]. However, from our experience a better regularization factor can be found, assuming that some sub-region in the reconstruction is expected to be homogeneous and smooth. The parameter c in the square root is chosen to be small to avoid singularities in the gradient.

The inverse problem is solved utilizing a quasi-Newton method, in particular the limited BFGS method. This requires the gradient of the objective function with respect to the shear modulus unknowns and the functional value of the objective function at every minimization iteration for the current shear modulus estimate. We note that we discretize the shear modulus with the same linear triangular shape functions utilized for the displacement and pressure in the forward problem. Thus the number of unknown shear modulus values is equal to the number of mesh nodes. The gradient is solved using the adjoint method, which requires only two linear matrix vector computations of the size of the linear forward problem. The computed displacement field in Eq. (6) satisfies the forward problem [Eqs. (1)–(5)] at each minimization call for the current estimate of the shear modulus. We omit the algorithms to solve the inverse problem iteratively as they were thoroughly discussed in [12, 16].

In the following we create hypothetical "measured" displacement data. In doing so, we define a square region of interest with unit length and a target shear modulus distribution consisting of two horizontally positioned inclusions in a homogeneous background (see Fig. 1). The shear modulus value in the inclusions is 5 and in the background 1. We apply a linear displacement boundary compression on the top edge, with the displacement varying from 0.002 to 0.008 from the left to right corner, respectively. The bottom edge is fixed in vertical direction and the center node on the bottom edge is fixed in all directions to prevent rigid body motion (see Fig. 1). All remaining boundary conditions not specified are traction free. The finite element mesh consists of 3,600 linear triangular elements and 3,721 mesh nodes. We add 3 % white Gaussian noise in order to mimic measured displacement data, which corresponds to about 70 % error in the strain field.

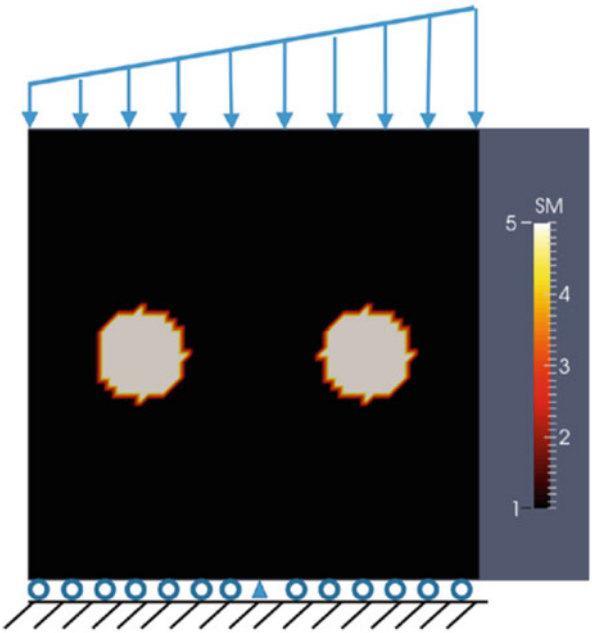

Fig. 1 Target shear modulus distribution of two inclusions in a homogeneous background. The *bottom edge* is fixed in vertical direction, represented by roller supports, except for the center node which is fixed in both directions. We apply a linearly varying compression on the *top edge*

2.2 Spatially Weighted Objective Function

In this section we present an alternative formulation of the objective function introduced in Sect. 2.1. We emphasize that the solution procedure of the inverse problem remains the same as discussed in Sect. 2.1. In order to simplify notations, we present the displacement correlation term in the objective function solely in terms of the vertical displacement component. We recall that we discard the horizontal displacement component entirely in the objective function. The modified objective function is given by

$$F = \frac{1}{2}\|W\,(u - u_{\text{meas}})\|_2^2 + \alpha \int_{\Omega} \sqrt{|\nabla \mu|^2 + c^2}\, d\Omega \tag{7}$$

where u is the computed vertical displacement component and u_{meas} is the measured vertical displacement component. W is a spatially weighted function defined as

$$W = \left(\frac{u_{\text{ave}}\,(u_{\text{ave}} + b)}{(u_{\text{meas}} + b)} + k\,(u_{\text{meas}} - u_{\text{ave}}) \right)^{-1} \tag{8}$$

where u_{ave} is the average measured displacement field of the entire region of interest, and b, k are constants. In Fig. 2 we plot the reciprocal of W over u_{meas} for different choices of the parameter k. We note that for small measured displacements k does

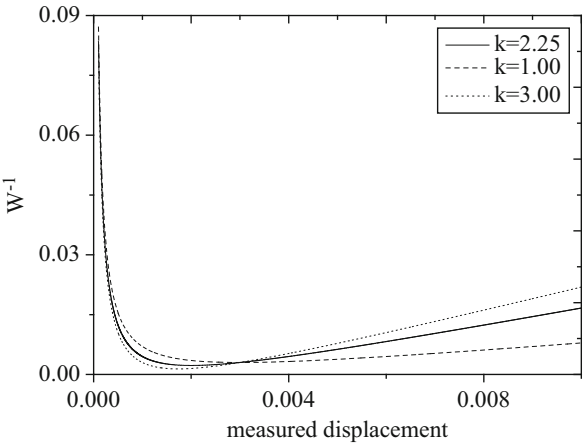

Fig. 2 Plot reciprocal of weighting function over the measured displacement field for $k = 1$, 2.25, and 3

not change the curves significantly, while for increasing measured displacements the curves become increasingly steep with increasing values of k. We choose k such that the product of $W(u^{\text{ave}}_{\text{meas}})u^{\text{ave}}_{\text{meas}}$ is the same in both inclusions, where $u^{\text{ave}}_{\text{meas}}$ is the average measured displacement in each inclusion. We determine the parameter $k = 2.25$, the average measured displacement field in the entire region of interest $u_{\text{ave}} = 0.003$, and set the parameter $b = 10^{-8}$. From our experience, the solution of the inverse problem is not sensitive for a wide range of parameter choices for b. An explicit form is given by $k = \frac{u_{\text{ave}}}{u^{\text{ave}}_{\text{meas},1}} + \frac{u_{\text{ave}}}{u^{\text{ave}}_{\text{meas},2}}$, where the index 1 and 2 refer to inclusion 1 and inclusion 2. In deriving the expression for k, we have assumed that b is much smaller than the averaged displacements, thus can be neglected.

3 Results

3.1 Reconstructions: Absolute Minimization of Displacement Correlation

In this section we solve the inverse problem with the formulation reviewed in Sect. 2.1. We utilize only one displacement field, thus $n = 1$ in Eq. (6) and the weight can be set to $w_1 = 1$. The regularization factor is chosen to be $\alpha = 1.3 \times 10^{-10}$ and the regularization constant is set to $c = 0.01$. In Fig. 3 we present the shear modulus reconstruction and compare it with the target shear modulus distribution. We observe that the left inclusion has a lower shear modulus value than the right inclusion. This difference becomes more apparent in the horizontal centerline plot shown in Fig. 3, where the bottom left plot represents the target shear modulus values and the bottom right plot the reconstructed shear modulus values. The shear modulus in the right inclusion is about 4, while the shear modulus in

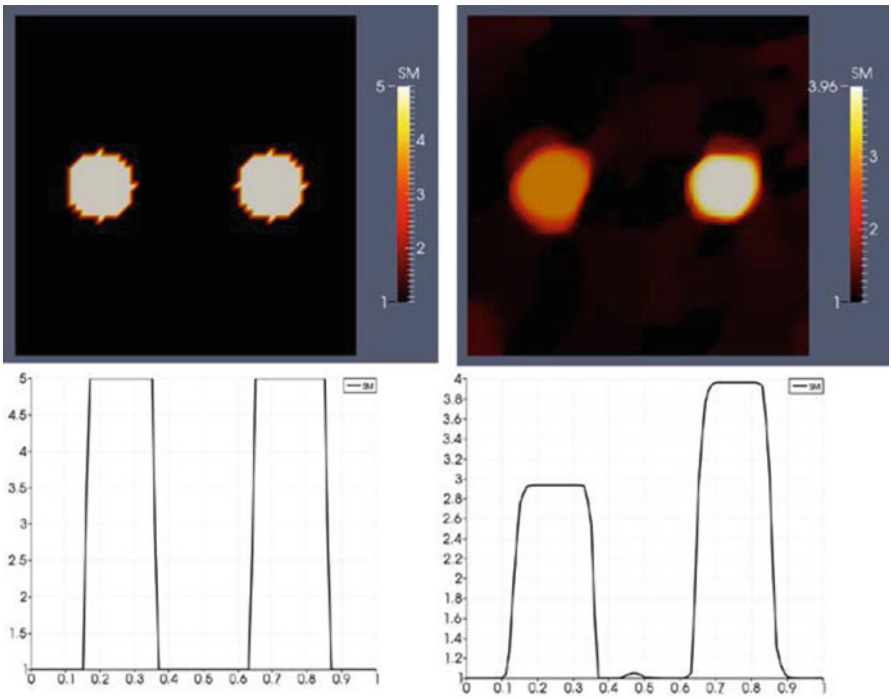

Fig. 3 *Top left*: target shear modulus distribution; *top right*: reconstructed shear modulus distribution; *bottom left*: horizontal centerline plot of the shear modulus through target inclusions; *bottom right*: horizontal centerline plot of the shear modulus through reconstructed inclusions

the left inclusion is about 3. The shear modulus value in the left inclusion is about 25 % smaller than in the right inclusion and about 40 % smaller than the target shear modulus value.

The change in the objective function is utilized as stopping criteria for the reconstructions as shown in Fig. 4. While the reconstructions were obtained after more than 4,000 iterations, we observe clearly that the objective function is already converged after 1,000 iterations.

3.2 Reconstructions: Spatially Weighted Objective Function

In this section we test the new formulation of the objective function, i.e., the spatially weighted displacement correlation term discussed in Sect. 2.2. The regularization factor in Eq. (7) is chosen to be $\alpha = 6.0 \times 10^{-6}$ and the regularization constant is set to $c = 0.01$. We compare the reconstructed shear modulus distribution with the target shear modulus distribution in Fig. 5. Clearly, the shear modulus contrast of the left inclusion has improved drastically, while the shear modulus in the

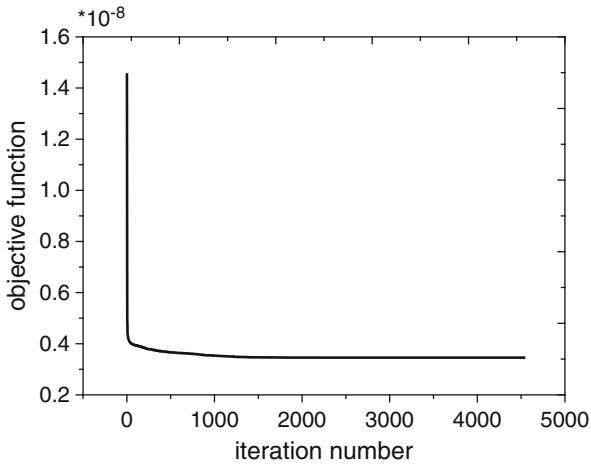

Fig. 4 Objective function value vs. iteration number

background fluctuates strongly. Additionally, the horizontal centerline plot through both inclusions reveals that the shear modulus value within the left inclusion area is very smooth and is not affected by this method. The shear modulus in the left inclusion is about 3.8 and in the right inclusion about 4. Thus, the shear modulus in the left inclusion improves by about 27 %. The drop down in the objective function is used as the stopping criteria. The convergence behavior is similar to Fig. 4 presented in Sect. 3.1 and is not shown here. Also, the results are not sensitive for a wide range of initial guesses. This also holds for the results obtained in Sect. 3.1.

4 Discussion

We briefly discussed the iterative solution of the inverse problem in elasticity, minimizing an objective function under the constraint of the forward elasticity problem. The objective function consists of a displacement correlation term and a regularization term, more precisely, total variation diminishing regularization. We have tested two different formulations for the objective function on hypothetical "measured" displacement data. The formulation of the objective revisited in Sect. 2.1 has been utilized in [11, 12, 15, 16]. Therein, the authors mainly utilized uniform boundary compression. In this chapter, we have shown that this method does not work well to recover the contrast of two inclusions in a homogeneous background, if linearly changing Dirichlet boundary is prescribed. We have omitted the solution of the inverse problem utilizing uniform Dirichlet boundary data, as this has been presented in [12]. We note that the use of linearly changing Dirichlet data leads to displacement fields that are much larger in the right inclusion than in the left inclusion.

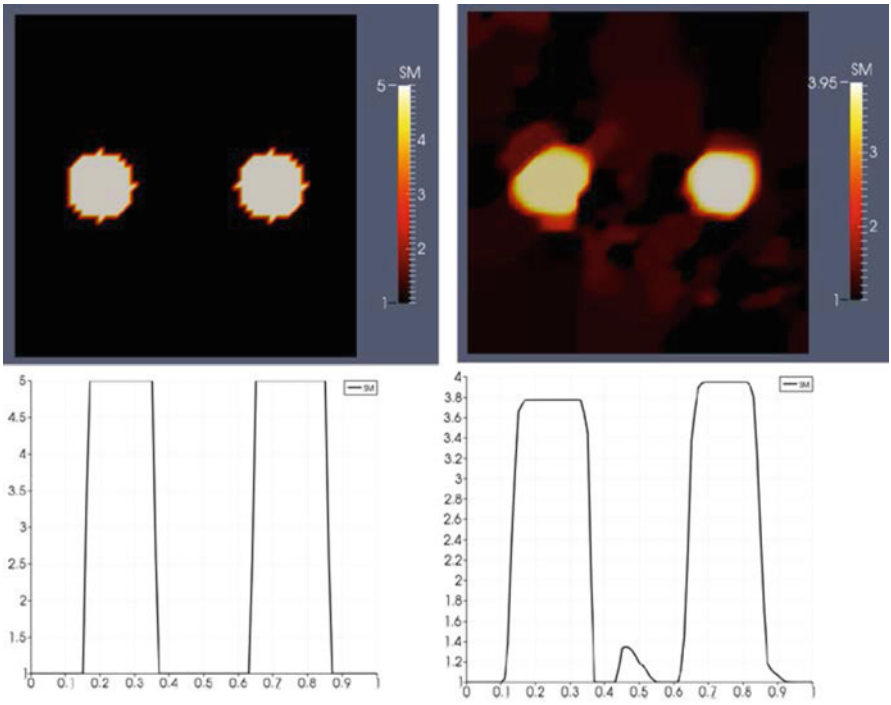

Fig. 5 *Top left*: target shear modulus distribution; *top right*: reconstructed shear modulus distribution; *bottom left*: horizontal centerline plot of the shear modulus through target inclusions; *bottom right*: horizontal centerline plot of the shear modulus through reconstructed inclusions

In fact, when utilizing the conventional formulation of the objective function, the absolute functional drop in the displacement correlation term corresponding to the right inclusion (larger displacement) will be greater than in the left inclusion (smaller displacement), leading to a closer target shear modulus value in the right inclusion. Thus in the new objective function, we weight the displacement correlation term with a functional that ensures that the displacement correlation is minimized equally within the two inclusions locally. It should be emphasized that this issue will persist with Neumann boundary data as well, if displacement fields within objects/inclusions are significantly different. We note that reciprocal of the weighted function W^{-1} becomes very large for small measured displacement fields (see Fig. 2). This is essential as small measured displacement fields are dominated by high noise levels, thus we are controlling the correlation of displacement data within regions of high noise levels.

We note that only Dirichlet boundary conditions (other than slip free conditions) were utilized in the present study, as it is not possible to measure traction boundary data with current ultrasound transducers. This implies that the recovered shear modulus is relative, in other words the shear modulus is determined only up

to a multiplicative factor. Thus the shear modulus ratio of tumor to background tissue is only known and not their absolute values. However, this information is sufficient to visualize the tumor based on this contrast. It is important to note that the optimization method is able to find one solution out of an infinite number of solutions due to the fact that the total variation diminishing regularization drives the smallest shear modulus value to the lowest bound defined in the optimization subroutine [19]. This has been mathematically proven for the one dimensional case in [20] and generalized to the three dimensional case in [21].

In all the computations presented, we have added about 3 % white Gaussian noise to the hypothetical data to mimic noisy experimental data. In fact, white Gaussian noise has been reported to be inherent in displacement measurements using ultrasound techniques [7]. The error in the strain is about 70 % which would be unacceptable to be utilized in a constitutive model [10]. Posing the inverse problem as a constrained and regularized minimization problem is the key to solve the inverse problem robustly in the presence of high noise levels in the displacement data.

Overall, the spatially weighted objective function performs well and reduces the sensitivity of the inverse problem to boundary conditions. A drawback, however, comes from the high oscillations in the background, while the conventional method appears to lead to a smoother shear modulus distribution in the background. This issue may be addressed developing improvised spatially weighted objective functions.

5 Conclusions

We presented a novel formulation of the objective function to solve the regularized inverse problem iteratively. We have shown that this method addresses issues of non-uniqueness observed with the conventional method. In particular, we created hypothetical "measured" displacement data for a target shear modulus distribution of two stiff inclusions in a homogeneous background under a linearly varying compression. One inclusion experiences a larger deformation than the other one, leading to a discrepancy in the minimization process using the conventional method. This is observed to result in large deviations in the shear modulus contrast for the inclusion with the smaller deformation. A novel spatially weighted objective function addresses this issue. This method may have important applications in determining the material properties of soft human tissues as well as detect and diagnose diseased tissues based on changes in their material properties.

References

1. Barbone, P.E., Oberai, A.A., Bamber, J.C., Berry, G.P., Dord, J.F., Ferreira, E.R., Goenezen, S., Hall, T.J.: Nonlinear and poroelastic biomechanical imaging: elastography beyond Youngs modulus. In: Neu, C., Genin, G. (eds.) CRC Handbook of Imaging in Biological Mechanics. CRC Press and Taylor & Francis, New York (2014)
2. Fung, Y.C.: Biomechanics: Mechanical Properties of Living Tissues, p. 433. Springer, New York (1981)
3. Martins, P.A.L.S., Natal Jorge, R.M., Ferreira, A.J.M.: A comparative study of several material models for prediction of hyperelastic properties: application to silicone-rubber and soft tissues. Strain **42**(3), 135–147 (2006)
4. Garra, B.S., Cespedes, E.I., Ophir, J., Spratt, S.R., Zuurbier, R.A., Magnant, C.M., Pennanen, M.F.: Elastography of breast lesions: initial clinical results. Radiology **202**(1), 79–86 (1997)
5. Goenezen, S., Dord, J.F., Sink, Z., Barbone, P., Jiang, J., Hall, T.J., Oberai, A.A.: Linear and nonlinear elastic modulus imaging: an application to breast cancer diagnosis. IEEE Trans. Med. Imaging **31**(8), 1628–1637 (2012)
6. de Korte, C.L., van der Steen, A.F., Cespedes, E.I., Pasterkamp, G.: Intravascular ultrasound elastography in human arteries: initial experience in vitro. Ultrasound Med. Biol. **24**(3), 401–408 (1998)
7. Ophir, J., Alam, S.K., Garra, B., Kallel, F., Konofagou, E., Krouskop, T., Varghese, T.: Elastography: ultrasonic estimation and imaging of the elastic properties of tissues. Proc. Inst. Mech. Eng. H **213**(3), 203–233 (1999)
8. Ophir, J., Cespedes, I., Ponnekanti, H., Yazdi, Y., Li, X.: Elastography: a quantitative method for imaging the elasticity of biological tissues. Ultrason. Imaging **13**(2), 111–134 (1991)
9. Skovoroda, A.R., Lubinski, L.A., Emelianov, S.Y., O'Donnell, M.: Reconstructive elasticity imaging for large deformations. IEEE Trans. Ultrason. Ferroelectr. Freq. Control **46**(3), 523–535 (1999)
10. Prusa, V., Rajagopal, K.R., Saravanan, U.: Fidelity of the estimation of the deformation gradient from data deduced from the motion of markers placed on a body that is subject to an inhomogeneous deformation field. J. Biomech. Eng. **135**(8), 081004 (2013)
11. Doyley, M.M., Meaney, P.M., Bamber, J.C.: Evaluation of an iterative reconstruction method for quantitative elastography. Phys. Med. Biol. **45**(6), 1521–1540 (2000)
12. Goenezen, S., Barbone, P., Oberai, A.A.: Solution of the nonlinear elasticity imaging inverse problem: the incompressible case. Comput. Methods Appl. Mech. Eng. **200**(13–16), 1406–1420 (2011)
13. Goenezen, S., Oberai, A.A., Dord, J., Sink, Z., Barbone, P.: In: Nonlinear Elasticity Imaging Bioengineering Conference (NEBEC), 2011 IEEE 37th Annual Northeast, pp. 1–2 (2011)
14. Hall, T., Barbone, P.E., Oberai, A.A., Jiang, J., Dord, J., Goenezen, S., Fisher, T.: Recent results in nonlinear strain and modulus imaging. Curr. Med. Imaging Rev. **7**(4), 313–327 (2011)
15. Kallel, F., Bertrand, M.: Tissue elasticity reconstruction using linear perturbation method. IEEE Trans. Med. Imaging **15**(3), 299–313 (1996)
16. Oberai, A.A., Gokhale, N.H., Feijóo, G.R.: Solution of inverse problems in elasticity imaging using the adjoint method. Inverse Prob. **19**(2), 297 (2003)
17. Maniatty, A.M., Liu, Y., Klaas, O., Shephard, M.S.: Higher order stabilized finite element method for hyperelastic finite deformation. Comput. Methods Appl. Mech. Eng. **191**(13–14), 1491–1503 (2002)
18. Vogel, C.R.: Computational Methods for Inverse Problems. Society for Industrial and Applied Mathematics, Philadelphia (2002)

19. Zhu, C., Byrd, R.H., Lu, P., Nocedal, J.: L-BFGS-B: a limited memory FORTRAN code for solving bound constrained optimization problems. Tech. Report, NAM-11, EECS Department, Northwestern University (1994)
20. Goenezen, S.: Inverse problems in finite elasticity: an application to imaging the nonlinear elastic properties of soft tissues. Ph.D. Dissertation (2011)
21. Tyagi, M., Goenezen, S., Barbone, P.E., Oberai, A.A.: Algorithms for quantitative quasi-static elasticity imaging using force data. Int. J. Numer. Methods Biomed. Eng. **30**(12) (2014)

Implementation of a Modified Moving Least Squares Approximation for Predicting Soft Tissue Deformation Using a Meshless Method

Habibullah Amin Chowdhury, Grand Roman Joldes, Adam Wittek, Barry Doyle, Elena Pasternak, and Karol Miller

1 Introduction

In case of brain surgery simulation, our vision is to enable a surgeon to interact with the computing facilities in the operating theatre and to visualize the results in real-time with high accuracy. In this way, a surgeon, without requiring any expert knowledge in numerical computation, would be able to evaluate the implications of each stage of a surgical procedure and explore potential alternative solutions. For this purpose, a robust and accurate method for solving the fundamental equations describing the biomechanical behaviour of the subject is an essential requirement. Conventionally, this kind of real-time computations in biomechanics was depended on linear finite element algorithms which assumed infinitesimal deformations [1, 2]. However, modelling of the brain for applications such as neurosurgical simulation and neuroimage registration for image-guided surgery is a non-linear problem of continuum mechanics which involves large deformations and large strains with geometric and material non-linearities. Therefore the infinitesimal assumption is not satisfied where such large deformations occur. Furthermore, in such cases, finite element method can fail due to element distortion. In this context, meshless methods [3, 4] provide a better alternative. The complex finite element grid generation and element distortion problems are avoided, as only a cloud of points are required for discretizing the model [5, 6] in meshless methods; a predefined mesh is not necessary. In this context, the meshless shape functions are important in approximating

H.A. Chowdhury (✉) • G.R. Joldes • A. Wittek • B. Doyle • K. Miller
Intelligent Systems for Medicine Laboratory (ISML), The University of Western Australia, Crawley, WA, Australia
e-mail: 21355123@student.uwa.edu.au

E. Pasternak
School of Mechanical and Chemical Engineering, The University of Western Australia, Crawley, WA, Australia

B. Doyle et al. (eds.), *Computational Biomechanics for Medicine*,
DOI 10.1007/978-3-319-15503-6_6

the unknown field functions to find the approximate solution to a problem governed by PDEs and boundary conditions using these arbitrarily distributed field nodes [4]. The MLS shape functions have been preferred predominantly in meshless methods [3, 7] due to the smoothness, continuity and consistency of the approximation field they create.

The MLS method was first introduced by Shepard [8] to construct smooth approximations for fitting a cloud of points [9]. In 1981, Lancaster and Salkauskas [10] extended this method for general surface generation problems. In generating meshless shape functions, higher order polynomial basis functions are useful in approximating complex data distributions. They also have the potential to increase the accuracy of the simulation results compared with linear basis function. However, as the degree of polynomial basis is increased, more nodes need to be included in the support domain to be able to compute the shape functions. Consequently, the size of the support domain gets enlarged resulting in increased computational cost. Furthermore, not all node distributions can be used in numerical computation for a given size of the support domain. Nevertheless, in most cases, a valid or "admissible" node distribution can be achieved by increasing the support domain size, which is often controlled by a dilatation parameter [11]. In this context, Joldes et al. [12] have recently presented a modified MLS approximation which allows higher order polynomial basis functions to be used under the same conditions as lower degree basis functions. Such an approximation can be used to create a more accurate meshless method without the need to change the nodal distribution or dilatation parameters used.

This paper focuses on the evaluation of a meshless method based on the MMLS shape function developed by Joldes et al. [12] in two specific cases of biomechanics simulations: extension of a soft tissue sample and simulation of a craniotomy induced brain shift. A comparison between the MMLS and the classical MLS with linear and quadratic basis in approximating a bivariate function is also presented.

2 The Modified Moving Least Squares Method

The procedure for constructing classical MLS shape function starts with the approximation of a function $u(\mathbf{x})$, denoted by $u^h(\mathbf{x})$, which is defined by a combination of m monomials (also called basis functions) [4].

$$u^h(\mathbf{x}) = \sum_{i=1}^{m} p_i(\mathbf{x}) a_i(\mathbf{x}) = \mathbf{p}^T(\mathbf{x}) \boldsymbol{a}(\mathbf{x}) \tag{1}$$

where m is the number of terms in the basis $\mathbf{p}(\mathbf{x})$, and $a_i(\mathbf{x})$ are coefficients that depend on the spatial co-ordinates $\mathbf{x}$. These coefficients are computed by minimizing an error functional defined based on the weighted least squares errors:

$$J(\mathbf{x}) = \sum_{j=1}^{n} \left[\left(u^h(\mathbf{x}_j) - u_j \right)^2 w\left(\| \mathbf{x} - \mathbf{x}_j \| \right) \right] \tag{2}$$

where n is the number of nodes in the support domain of $\mathbf{x}$. Rewriting in matrix form yields:

$$\mathbf{J} = (\mathbf{Pa} - \mathbf{u})^T \mathbf{W} (\mathbf{Pa} - \mathbf{u}) \tag{3}$$

Minimization is done by setting the partial derivatives of the error functional J to zero:

$$\frac{\partial \mathbf{J}}{\partial \mathbf{a}} = \mathbf{P}^T \mathbf{WP}\mathrm{a}(\mathrm{x}) - \mathbf{P}^T \mathbf{Wu} = 0 \tag{4}$$

Finally, by solving the resulting system of equations, the MLS approximation is obtained as

$$u^h(\mathbf{x}) = \sum_{j=1}^{n} \varnothing_j(\mathbf{x})\, u_j = \boldsymbol{\Phi}^{\boldsymbol{T}}(\mathbf{x})\, \mathbf{u} \tag{5}$$

where

$$\varnothing_j(\mathbf{x}) = p^T(\mathbf{x}) \left(\boldsymbol{M}^{(-1)}(\mathbf{x})\, \boldsymbol{B}(\mathbf{x}) \right) \tag{6}$$

$$\boldsymbol{M}(\mathbf{x}) = \sum_{j=1}^{n} w\left(\mathbf{x} - \mathbf{x}_j\right) p\left(\mathbf{x}_j\right) p^T\left(\mathbf{x}_j\right) \tag{7}$$

$$\boldsymbol{B}(\mathbf{x}) = [B(\mathbf{x}_1)\ \ B(\mathbf{x}_2) \ldots B(\mathbf{x}_n)] \tag{8}$$

$$B(\mathbf{x}_1) = w(\mathbf{x} - \mathbf{x}_1)\, p(\mathbf{x}_1) \tag{9}$$

Here, $\mathbf{u}$ is the nodal vector parameters of all the nodal field variables in the local support domain, $\boldsymbol{\Phi}(\mathbf{x})$ is the vector of MLS shape functions and $\boldsymbol{M}(\mathbf{x})$ is known as the moment matrix. Generally, linear or quadratic basis functions and cubic or quartic weight functions are used to create the approximation.

As can be seen from Eq. (6), the shape functions construction depends on the non-singularity of the moment matrix defined by Eq. (7). The necessary conditions for the moment matrix to be non-singular depend on the types of basis functions used. For example, in a two-dimensional case, the moment matrix is non-singular as long as there are at least three non-collinear nodes in the support domain for linear basis functions, whereas for a quadratic basis, at least six nodes are needed in the support domain. The support domain of a point $\mathbf{x}$ determines the number of nodes used to compute the approximation value at $\mathbf{x}$. However, some nodal distributions can still lead to singular moment matrices even if enough nodes are included in

the support domain. This type of scenario can occur, for example, if the nodes are distributed on two parallel lines in 2D. To overcome this problem, the traditional remedy is to enlarge the support domains in order to include more nodes. This, however, leads to higher approximation error and increased computational cost. Consequently, these limitations prevent the practical use of higher order polynomial basis for randomly distributed nodes despite their potential capability for better approximation of complex deformation fields and better convergence properties.

In this context, Joldes et al. [12] developed a modified MLS with second order polynomial basis. The development of MMLS is based on the observation that a singular moment matrix mainly means that Eq. (4) used to compute the coefficients $\mathbf{a}(\mathbf{x})$ has multiple solutions, and therefore the functional (2) does not include sufficient constraints to guarantee a unique solution for the given nodal distribution. Based on this observation, for 2D, additional constraints are included in the functional (2) as

$$\overline{J}(\mathbf{x}) = \sum_{j=1}^{n} \left[\left(u^h(\mathbf{x}_j) - u_j \right)^2 w\left(\| \mathbf{x} - \mathbf{x}_j \| \right) \right] + \mu_{x^2} a_{x^2}^2 + \mu_{xy} a_{xy}^2 + \mu_{y^2} a_{y^2}^2 \tag{10}$$

where

$$\mu = \left[\mu_{x^2} \ \mu_{xy} \ \mu_{y^2} \right] \tag{11}$$

is defined as vector of positive weights for the additional constraints. Using the same minimization procedure, the modified approximant is obtained as:

$$\overline{u}^h(\mathbf{x}) = \mathbf{P}^T \left(\mathbf{P}^T \mathbf{W} \mathbf{P} + \mathbf{H} \right)^{-1} \mathbf{P}^T \mathbf{W} \mathbf{u} = \sum_{j=1}^{n} \overline{\varnothing}_j(\mathbf{x}) u_j = \overline{\mathbf{\Phi}}^{\boldsymbol{T}}(\mathbf{x}) \mathbf{u} \tag{12}$$

With the new shape function defined as

$$\overline{\mathbf{\Phi}}(\mathbf{x}) = \left[\overline{\Phi}_1(\mathbf{x}) \ldots \ \overline{\Phi}_n(\mathbf{x}) \right] = \mathbf{P}^T \left(\mathbf{P}^T \mathbf{W} \mathbf{P} + \mathbf{H} \right)^{-1} \mathbf{P}^T \mathbf{W} \tag{13}$$

Here, $\mathbf{H}$ is a matrix with all elements zeros except the last three diagonal entries, which are equal to $\boldsymbol{\mu}$

$$H = \begin{bmatrix} \mathbf{O}_{33} & \mathbf{O}_{33} \\ \mathbf{O}_{33} & diag(\boldsymbol{\mu}) \end{bmatrix} \tag{14}$$

and the modified moment matrix is computed as:

$$\overline{\mathbf{M}} = \mathbf{P}^T \mathbf{W} \mathbf{P} + \mathbf{H} = \mathbf{M} + \mathbf{H} \tag{15}$$

The small alteration of the moment matrix presented in the above equation is the only difference between the MMLS and the classic MLS with quadratic basis functions. Nevertheless, it can be shown that the nodal distributions which are admissible for the classical MLS with linear basis functions are also admissible for the presented MMLS [12].

3 Numerical Examples

3.1 Approximation Capability in 2D

To assess the approximations capability of the modified MLS shape functions with quadratic basis, it is compared with classical MLS shape function with linear and quadratic basis. A quartic spline weight function with circular domain was used in the definition of all shape functions:

$$w(s) = \begin{cases} 1 - 6s^2 + 8s^3 - 3s^4, & s \leq 1 \\ 0, & s > 1 \end{cases} \tag{16}$$

where s is the normalized distance

$$s_j = \frac{\| \mathbf{x} - \boldsymbol{x}_j \|}{R_j} \tag{17}$$

and R_j is the radius of the influence domain of node $\mathbf{x}_\mathrm{j}$. In this example, the same weights for all the additional constraints ($\mu_x{}^2 = \mu_{xy} = \mu_y{}^2 = \mu$) and a constant radius of influence for all nodes ($R_j = R$) were used. A 2D rectangular problem domain was defined and the geometry was represented using both regular and irregular node distributions consisting of 324 nodes, as shown in Fig. 1. The irregular nodal distribution consisted of uniformly scattered nodes were obtained by using the Matlab Halton sequence function [13]. The use of this function ensures a uniform nodal density for the problem domain. The following function was used for testing the approximation accuracy in 2D using MLS and the MMLS for different values of μ and R. The function was chosen to present a variety of behaviour in a surface which consists of Gaussian peaks with sharp descent.

$$u(x, y) = xe^{-x^2-y^2} \tag{18}$$

The approximation accuracy was determined using the root mean square error evaluated using a regular distribution of $N = 81 \times 81$ points:

$$RMSE = \sqrt{\frac{\sum_{i=1}^{N} \left(u(x) - u^h(x)\right)^2}{N}} \tag{19}$$

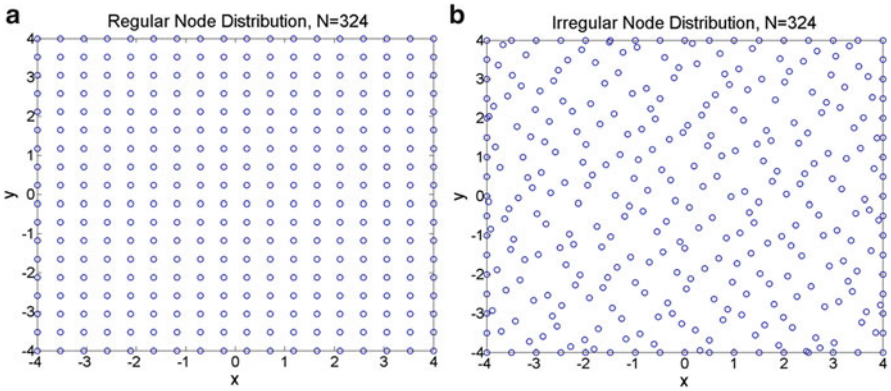

Fig. 1 (**a**) Regular node distribution, (**b**) Irregular node distribution

Table 1 Root mean square error (RMSE) in approximating $\boldsymbol{u}(\boldsymbol{x}, \boldsymbol{y}) = \boldsymbol{x}\boldsymbol{e}^{-x^2-y^2}$ using 324 nodes with varying radius of nodal influence domain, R

	Regular node distribution			Irregular node distribution		
Approximation method	$R = 2.0$	$R = 1.5$	$R = 0.8$	$R = 2.0$	$R = 1.5$	$R = 0.8$
MLS, linear BF	0.0344	0.0272	0.0098	0.0361	0.0281	0.0118
MLS, quadratic BF	0.0081	0.0058	Singular M	0.0107	0.0080	Singular M
MMLS, $\mu = 0.1$	0.0109	0.0106	0.0092	0.0131	0.0125	0.0113
MMLS, $\mu = 0.01$	0.0083	0.0064	0.0064	0.0109	0.0085	0.0089
MMLS, $\mu = 0.001$	0.0081	0.0059	0.0035	0.0107	0.0080	0.0053
MMLS, $\mu = 0.0001$	0.0081	0.0058	0.0029	0.0107	0.0080	0.0046

The results are shown in Table 1.

From the results, it can be seen that as the nodal influence domain radius is gradually decreased, the classic MLS with quadratic basis fails due to singular moment matrix whereas the modified MLS with quadratic basis is stable. The approximation accuracy of MMLS is found to be better than that of classical MLS with linear basis function. Moreover, it is also evident that if the value of μ is decreased, the MMLS accuracy approaches the accuracy of classical MLS with quadratic basis function.

3.2 Applications in Biomechanics

In brain biomechanics, for computing soft tissue deformation considering large deformation and large strain, Miller et al. [14] have developed an efficient finite element algorithm using total Lagrangian (TL) formulation and explicit time integration scheme. The algorithm is capable of handling both geometric and material non-linearities. The adoption of TL formulation allows pre-computation of

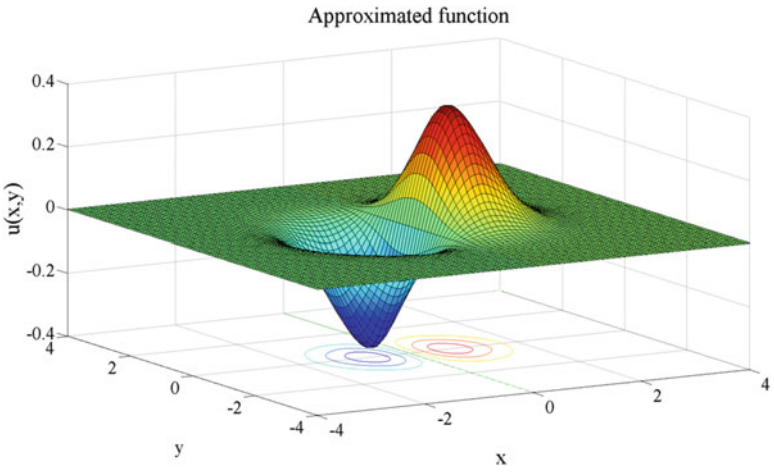

Fig. 2 Approximated function by modified MLS ($\mu = 0.1$, $R = 0.8$) using a regular distribution of 324 nodes

all derivatives with respect to spatial co-ordinates and the explicit time integration based on the central difference method eliminates the necessity for iterations during each time-step. These features resulted in significant reduction in the number of mathematical operations and constituted the base for real-time simulations. Several applications were developed in both surgical simulation and neuroimage registration based on this total Lagrangian explicit dynamics framework [15–19]. Motivated by the prospect of meshless method, Horton et al. [20] developed the Meshless Total Lagrangian Explicit Dynamics (MTLED) algorithm based on the earlier work of Miller et al. [14]. MTLED is based on the Galerkin weak form and uses a regular background grid for integration.

The modified MLS shape functions were incorporated in the MTLED algorithm. For easy imposition of the essential boundary conditions, a regularized weight function [21] was used which possesses almost interpolating properties, as shown in Fig. 3.

Next, two cases of biomechanics applications, an extension of a soft tissue sample and craniotomy induced brain deformation are simulated using the meshless method which incorporates the MMLS with regularized weight functions. The results obtained by the meshless method are compared with those obtained using the commercial finite element software ABAQUS.

3.2.1 Extension of Soft Tissue Sample

For the meshless computation of soft tissue extension, a 2D geometry (10 cm × 4 cm) was created and the domain and boundary were discretized using 57 nodes. To ensure integration accuracy, a regular background grid was used

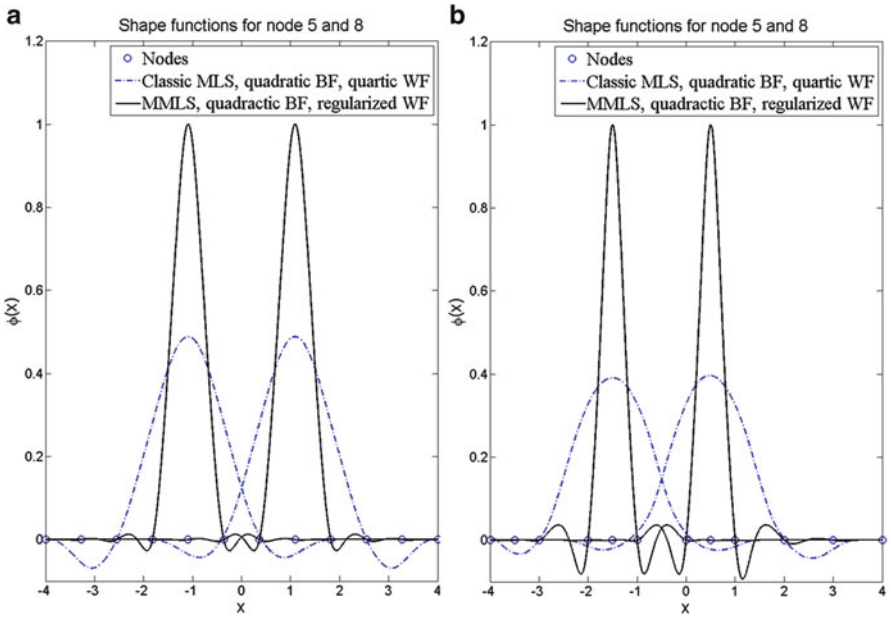

Fig. 3 Classic MLS and Modified MLS ($\mu = 0.01$) with regularized weight function comparison, 12 nodes in 1-D, influence domain radius $R = 3$; (**a**) regular, (**b**) irregular nodal distributions

consisting of 1,000 integration cells with one integration point per cell. For each node, the radius of the influence domain was constant ($R = 1.4$). Loading in terms of displacement (3 cm) was applied to the nodes on the right-hand side boundary and the left boundary nodes were fixed. Explicit integration was performed using the central difference method, with mass proportional damping added (dynamic relaxation) to control the oscillations in order to reach the steady state solution [16, 22].

For simplicity, following [16, 17], the hyper-elastic Neo-Hookean material model was chosen in this numerical experiment to capture the behaviour of soft tissues undergoing large deformation. For the finite element analysis in ABAQUS, identical constitutive material laws, loading and boundary conditions were used; the steady state solution was obtained using the static solver with the default configuration. The simulation results and numerical details are presented in Fig. 4 and Table 2.

For the given nodal influence domain radius, the classical MLS with quadratic basis failed due to the singularity of moment matrix. The differences in computed deformation fields over the whole problem domain are shown in Fig. 4. The results in Table 2 show that the maximum and average difference in displacements between MMLS and ABAQUS are lower compared to those between classic MLS with linear basis and ABAQUS.

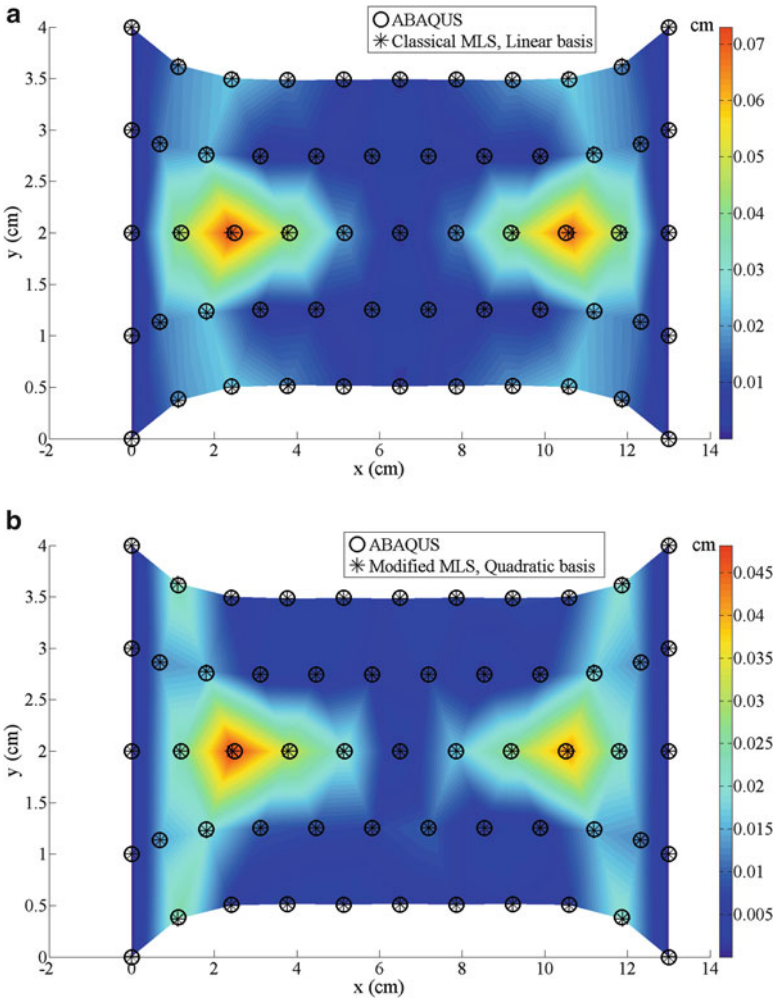

Fig. 4 Differences of the computed deformation field over the whole problem domain, (**a**) between classic MLS (linear basis) and ABAQUS; (**b**) between modified MLS and ABAQUS

Table 2 Numerical details of comparison for the cases presented in Fig. 4

Case	Nodes	Elements (ABAQUS)	Integration points (Meshless)	Average difference (mm)	Maximum difference (mm)
a) Classical MLS	57	84	1,000	0.14996	0.73014
b) MMLS ($\mu = 10^{-10}$)	57	84	1,000	0.10193	0.48192

3.2.2 Simulation of Brain Deformation in 2D

In order to simulate brain deformation, based on experimental data [23] and previous modelling experience [15, 24], the Young's modulus for the brain parenchyma and the tumour was set to 3,000 Pa and 6,000 Pa respectively. Because of the fact that the brain tissue is almost incompressible [25], according to [24] a Poisson's ratio of 0.49 was assigned for both parenchyma and tumour. The ventricles are modelled as a cavity as the cerebrospinal fluid can freely move in and out of them. A variable load in terms of displacement was enforced on the nodes of the brain surface exposed by craniotomy. The interaction between skull and brain was modelled as finite sliding, frictionless contact and the skull was assumed to be rigid as it is orders of magnitude stiffer than the brain tissue. The brain model was discretized with 707 nodes, and for the meshless method 4,988 integration points were created from a triangular background grid with four integration points per cell. A constant influence domain ($R = 8$) and same weights for the additional constraints ($\mu = 10^{-7}$) were used in the meshless computation. Higher order plain strain elements with hybrid formulation were used in ABAQUS to handle the incompressibility of the soft tissues. The constitutive material laws, loading and boundary conditions were identical in both meshless and ABAQUS computations. The differences of the computed deformation field between classical MLS and modified MLS in comparison with ABAQUS are shown in Fig. 5. Numerical details of the comparison are presented in Table 3.

In this experiment, for the given support domain radius, the classic MLS with quadratic basis also failed due to the singularity of moment matrix, whereas the modified MLS with quadratic basis had no problem in computing the shape functions. As shown in Table 3, the maximum and average differences between MMLS and ABAQUS are found to be lower compared to those between classic MLS with linear basis and ABAQUS.

4 Conclusions

In this paper we assessed the use of a modified MLS approximation with a meshless method for predicting soft tissue deformation. The approximation capability of the MMLS is evaluated against the classical MLS with linear and quadratic basis functions for a bivariate function. The results show that the MMLS approximation with a quadratic basis is stable with the same support domain size as the classical MLS using linear basis functions. Moreover, when the value of the weight μ, associated with the additional constraints, is decreased, the accuracy of MMLS approaches the accuracy of classical MLS with quadratic basis functions.

A meshless method using the MMLS shape functions was used for the simulation of extension of a soft tissue sample and craniotomy induced brain deformation. A regularized weight function was used in these examples to enforce the essential boundary conditions. The results were compared with results obtained using the commercial finite element software ABAQUS. In both cases, the results indicate

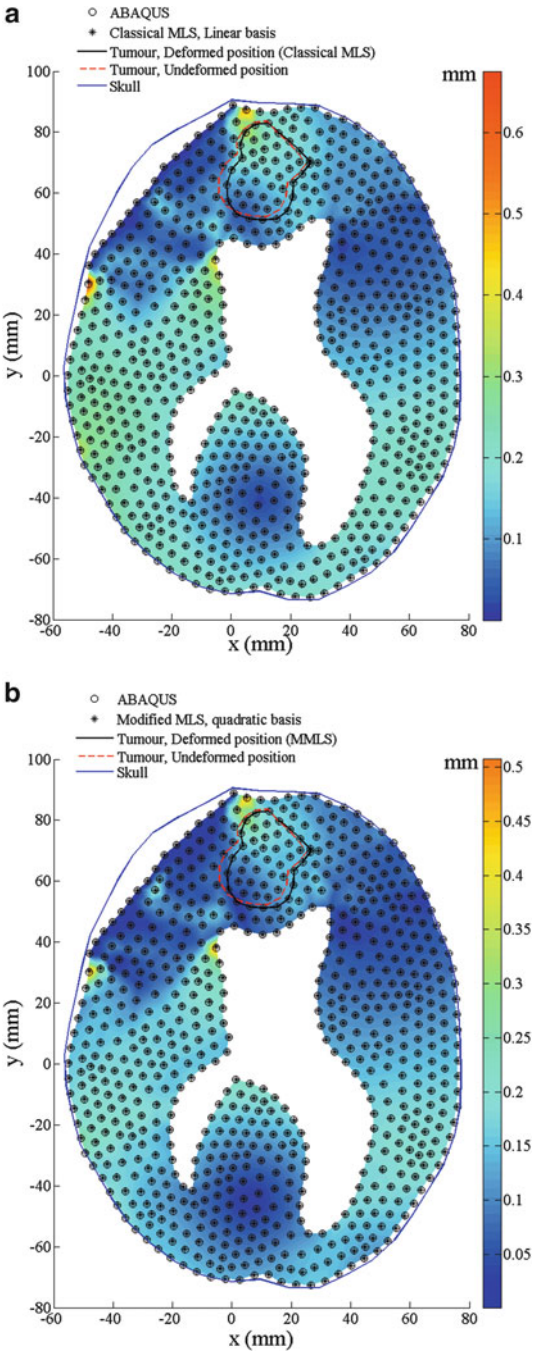

Fig. 5 Differences of the computed deformation field in the brain (**a**) between classic MLS (linear basis) and ABAQUS; (**b**) between modified MLS and ABAQUS

Table 3 Numerical details of comparison for the cases presented in Fig. 5

Case	Nodes	Elements (ABAQUS)	Integration points (Meshless)	Average difference (mm)	Maximum difference (mm)
a) Classical MLS	707	1,247	4,988	0.14509	0.67531
b) MMLS ($\mu = 10^{-7}$)	707	1,247	4,988	0.12332	0.50729

that the MMLS shape functions, having a quadratic basis, provide better accuracy with the same support domain size, compared to classical MLS with linear basis. With the same support domain size, classical MLS with quadratic basis simply fails due to singular moment matrices.

Acknowledgments The first author is a recipient of the SIRF scholarship and acknowledges the financial support of the University of Western Australia. The financial support of Australian Research Council (Discovery Grant No. DP120100402) and National Health and Medical Research Council (Grant No. APP1063986) is gratefully acknowledged.

References

1. Cotin, S., Delingette, H., Ayache, N.: A hybrid elastic model for real-time cutting, deformations, and force feedback for surgery training and simulation. Vis. Comput. **16**(8), 437-452 (2000). doi:10.1007/Pl00007215
2. Warfield, S.K., Talos, F., Tei, A., Bharatha, A., Nabavi, A., Ferrant, M., Black, P.M.L., Jolesz, F.A., Kikinis, R.: Real-time registration of volumetric brain MRI by biomechanical simulation of deformation during image guided neurosurgery. Comput. Vis. Sci. **5**(1), 3–11 (2002). doi:10.1007/s00791-002-0083-7
3. Belytschko, T., Lu, Y.Y., Gu, L.: Element-free Galerkin methods. Int. J. Numer. Methods. Eng. **37**(2), 229–256 (1994). doi:10.1002/nme.1620370205
4. Liu, G-R.: Meshfree Methods: Moving Beyond the Finite Element Method. CRC Press, Boca Raton, Florida, USA (2010)
5. Wittek, A., Joldes, G.R., Miller, K.: Algorithms for computational biomechanics of the brain. In Miller, K. (Ed), Biomechanics of the Brain, pp. 189-219, Springer, New York (2011)
6. Miller, K., Wittek, A., Joldes, G.R.: Biomechanical Modeling of the Brain for Computer-Assisted Neurosurgery. In Miller, K. (Ed), Biomechanics of the Brain, pp. 111-136, Springer, New York (2011)
7. Nayroles, B., Touzot, G., Villon, P.: Generalizing the finite element method: diffuse approximation and diffuse elements. Comput. Mech. **10**(5), 307–318 (1992). doi:10.1007/bf00364252
8. Shepard, D.: A two-dimensional interpolation for irregularly-spaced data. Paper presented at the 23rd ACM national conference (1968)
9. Nguyen, V.P., Rabczuk, T., Bordas, S., Duflot, M.: Meshless methods: a review and computer implementation aspects. Math. Comput. Simul. **79**(3), 763–813 (2008). doi:10.1016/j.matcom.2008.01.003
10. Lancaster, P., Salkauskas, K.: Surfaces generated by moving least-squares methods. Math. Comput. **37**(155), 141–158 (1981). doi:10.2307/2007507
11. Li, S., Liu, W.K.: Meshfree Particle Methods. Springer, Berlin (2004)

12. Joldes, G.R., Chowdhury, H.A., Wittek, A., Doyle, B., Miller, K.: Modified Moving Least Squares with Polynomial Bases for Scattered Data Approximation. UWA, Perth, WA, Report # ISML/02/2014: 17 pages. (school.mech.uwa.edu.au/ISML/index.php/Reports) (2014)
13. Fasshauer, G.E.: Meshfree Approximation Methods with MATLAB. World Scientific Publishing Co., Inc., Singapore (2007)
14. Miller, K., Joldes, G., Lance, D., Wittek, A.: Total Lagrangian explicit dynamics finite element algorithm for computing soft tissue deformation. Commun. Numer. Methods. Eng. **23**(2), 121–134 (2006). doi:10.1002/cnm.887
15. Joldes, G.R., Wittek, A., Couton, M., Warfield, S.K., Miller, K.: Real-Time Prediction of Brain Shift Using Nonlinear Finite Element Algorithms. Medical Image Computing and Computer-Assisted Intervention – Miccai 2009, Pt Ii, Proceedings, vol. 5762, pp. 300–307 (2009)
16. Joldes, G.R., Wittek, A., Miller, K.: Computation of intra-operative brain shift using dynamic relaxation. Comput. Methods. Appl. Mech. Eng. **198**(41–44), 3313–3320 (2009). doi:10.1016/j.cma.2009.06.012
17. Joldes, G.R., Wittek, A., Miller, K.: Suite of finite element algorithms for accurate computation of soft tissue deformation for surgical simulation. Med. Image. Anal. **13**(6), 912–919 (2009). doi:10.1016/j.media.2008.12.001
18. Joldes, G.R., Wittek, A., Miller, K.: Real-time nonlinear finite element computations on GPU – application to neurosurgical simulation. Comput. Methods. Appl. Mech. Eng. **199**(49–52), 3305–3314 (2010). doi:10.1016/j.cma.2010.06.037
19. Wittek, A., Joldes, G., Couton, M., Warfield, S.K., Miller, K. Patient-specific non-linear finite element modelling for predicting soft organ deformation in real-time; application to non-rigid neuroimage registration. Prog. Biophys. Mol. Biol. **103**(2–3), 292–303 (2010). doi:10.1016/j.pbiomolbio.2010.09.001
20. Horton, A., Wittek, A., Joldes, G.R., Miller, K.: A meshless total Lagrangian explicit dynamics algorithm for surgical simulation. Int. J. Numer. Methods Biomed. Eng. **26**(8), 977–998 (2010). doi:10.1002/cnm.1374
21. Most, T., Bucher, C.: A moving least squares weighting function for the element-free Galerkin method which almost fulfills essential boundary conditions. Struct. Eng. Mech. **21**(3), 315–332 (2005)
22. Joldes, G.R, Wittek, A., Miller, K.: An adaptive dynamic relaxation method for solving nonlinear finite element problems. Application to brain shift estimation. Int. J. Numer. Methods. Biomed. Eng. **27**(2), 173–185 (2011). doi:10.1002/cnm.1407
23. Miller, K., Chinzei, K., Orssengo, G., Bednarz, P.: Mechanical properties of brain tissue in-vivo: experiment and computer simulation. J. Biomech. **33**(11), 1369–1376 (2000). doi:10.1016/S0021-9290(00)00120-2
24. Zhang, J.Y., Joldes, G.R., Wittek, A., Miller, K.: Patient-specific computational biomechanics of the brain without segmentation and meshing. Int. J. Numer. Methods. Biomed. Eng. **29**(2), 293–308 (2013). doi:10.1002/cnm.2507
25. Miller, K.: Biomechanics of the Brain. Springer, New York (2011)

Part II
New Applications

Automatic Landmark Detection Using Statistical Shape Modelling and Template Matching

Habib Y. Baluwala, Duane T.K. Malcolm, Jessica W.Y. Jor, Poul M.F. Nielsen, and Martyn P. Nash

1 Introduction

Biomechanical modelling of the breast can provide a reliable way of co-locating tissue locations across various images. Biomechanical models of the breast can be used for guiding clinical biopsy procedures, track tumours for surgical assistance and for both aiding the breast implant selection and predicting the outcome of breast augmentation procedures [1]. However, to generate a patient specific model of the breast, an alignment of the mean mesh on the new patient image volume is required. This alignment can be achieved using landmark detection.

An important area in image understanding is the development of methods for robust and accurate detection of landmarks. Landmarks can be used: as seed points in image segmentation; for mesh generation for biomechanical models; and to define rigid, affine, or thin plate transformations in image registration. Algorithms for automated detection of landmarks are crucial for clinical applications since manual selection of landmarks is time consuming and subjective. In our work, we focus on automated detection of multiple landmarks for breast magnetic resonance (MR) images to be used for torso skin surface mesh generation.

Landmarks can be defined as distinct anatomical points in the body or as edges which can be used as feature points [2]. Landmark detection in medical imaging is focused on three approaches: (a) machine learning algorithms [3, 4]; (b) image intensity models [5]; and (c) invariant geometric measures such as curvatures and

H.Y. Baluwala (✉) • D.T.K. Malcolm • J.W.Y. Jor
Auckland Bioengineering Institute, 70 Symonds Street, Auckland 1010, New Zealand
e-mail: h.baluwala@auckland.ac.nz

P.M.F. Nielsen • M.P. Nash
Auckland Bioengineering Institute, 70 Symonds Street, Auckland 1010, New Zealand

Department of Engineering Science, University of Auckland, Auckland, New Zealand

B. Doyle et al. (eds.), *Computational Biomechanics for Medicine*,
DOI 10.1007/978-3-319-15503-6_7

extreme points based on their shapes [6]. Hartkens et al. [7] proposed detection of landmarks by analysing the image intensity up to third derivatives. Frantz et al. [8] implemented a statistical approach for landmark detection which requires the user to set an initial region of interest in the vicinity of the landmark. Most of these methods are either semi-automatic or cannot accurately detect landmarks on the skin surface from breast MRs due to the wide dynamic intensity range or variability of breast and torso shapes across patients and populations. Some of these methods are sensitive to noise and extract numerous false positives.

We address this problem of landmark detection by combining statistical shape models (SSMs) and landmark image features into a single framework. This process is divided into five steps: (a) build an SSM of the landmarks; (b) build a template patch for each landmark; (c) match the template patch with an unseen image to produce a correlation map; (d) search for the combination of shape components that provides the best combined correlation map values; (e) search the local region of the correlation map for each landmark and move the shape predicted landmark to the local maximum of correlation map. Leave-one-out experiments were performed on 2D breast MR slices from 30 volunteers to test the robustness and accuracy of our method. The algorithm can be straightforwardly extended to 3D, and to detect landmarks for other anatomical structures.

2 Methods

2.1 Statistical Shape Modelling

SSMs have been used extensively for segmentation, recognition, and classification [9]. SSMs provide prior information to the image processing tools that helps to improve accuracy, robustness, and computational speed. Given a number of training shapes, an SSM consists of the average shape along with statistical information about the shape variation.

To build the SSM, we require a training set of images with corresponding labels for each landmark. Figure 1 shows two of our training examples, which consists of thirty 2D MRI slices, each from a different volunteer, that have been manually labelled by an expert. Each training image has been obtained from a different patient. Each image is labelled with 30 landmarks: 24 landmarks are labelled on the skin surface and 6 other landmarks that do not lie on the skin surface are the centres of the sternum, spinal cord, aorta, vertebra, and nipples. The six landmarks outside the skin surface were chosen as they have relatively fixed positions within the chest and can be readily detected in any unseen image. The SSM is built for the training set using the method of Cootes and Taylor [9] and provides a parameterisation, $\mathbf{b}$, of shapes similar to the training set

$$\mathbf{X} = \overline{\mathbf{X}} + \mathbf{Pb} \tag{1}$$

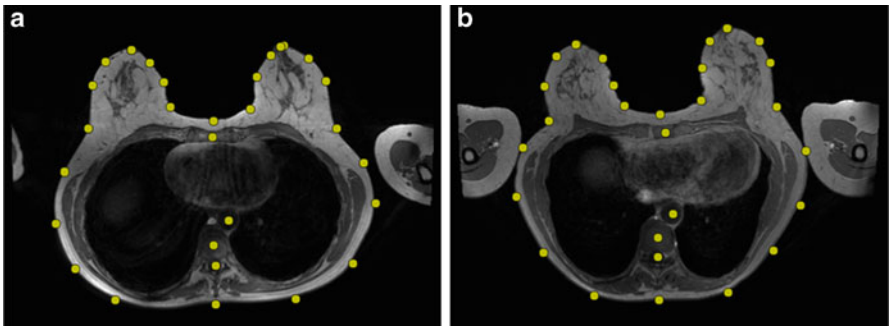

Fig. 1 Training examples for building statistical shape models of landmarks. 2D MR images from two volunteers are overlaid with manually labelled landmarks (*yellow dots*)

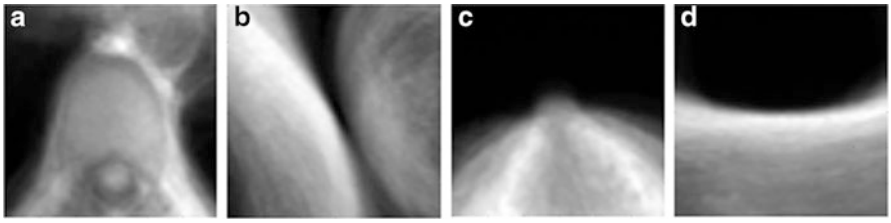

Fig. 2 Template patches for four landmarks. (**a**) Vertebra centre. (**b**) Skin surface point near the right arm. (**c**) Right nipple. (**d**) Skin surface point between the breasts

where $\overline{\mathbf{X}}$ is mean shape, $\mathbf{P}$ is a set of orthogonal modes of variation, and $\mathbf{b}$ defines a set of components of a deformable model. By varying the elements of $\mathbf{b}$, we can vary the shape $\mathbf{X}$ using Eq. (1).

2.2 Generation of Template Patches

The second part of our algorithm deals with matching template patches for each landmark across an unseen image. The template patch for a particular landmark is obtained by taking the average of the set of 60 mm × 60 mm patches that surrounded the manually identified landmarks from the images in the training set, for which the image intensities were normalised between 0 and 255 to compensate for variations between training images. Figure 2 shows examples of template patches for four different landmarks.

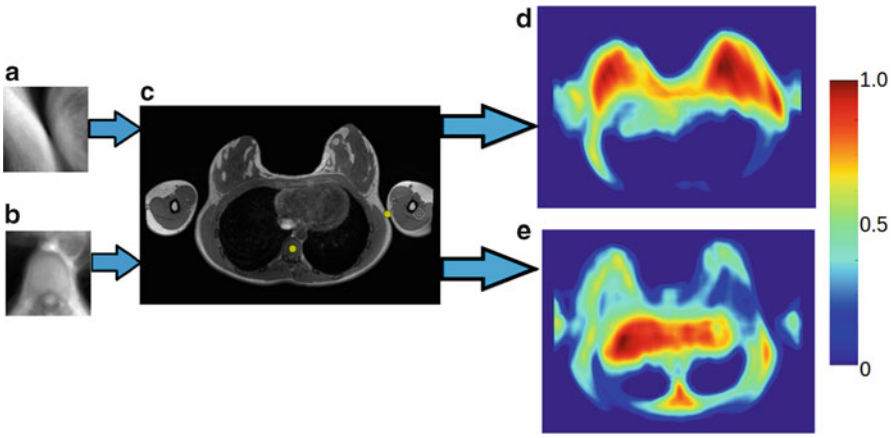

Fig. 3 (**a**) and (**b**) are examples of template images of landmarks and (**c**) an unseen image (with manually labelled landmarks for vertebra centre and skin surface for right arm). (**d**) and (**e**) are the correlation maps obtained after matching templates (**a**) and (**b**), respectively, with the unseen image. A higher value in the correlation map indicates a higher likelihood of the landmark being present at that location

2.3 Template Matching to Obtain a Correlation Image

Template matching is the process of sliding a template patch across an unseen image and comparing the overlapped patches using a similarity metric. We use normalised sum of squared differences as a similarity metric. The output from this step is a correlation map that can be used to infer the likelihood of the location of that particular landmark in the image. The unseen image intensities are normalised between 0 and 255 before applying template matching. Template matching was performed for all 30 landmarks to obtain 30 correlation maps. Figure 3 shows the correlation maps obtained for the vertebra centre and skin surface point of the torso near arm. As shown in Fig. 3e, the correlation map shows a local maximum for the landmarks in its actual location. It also shows a local maximum at other positions (false positives) in the image. Thus template matching alone is not robust for detecting individual landmarks since it can result in false positives.

2.4 Shape Component Optimisation

To combine the template matching information with shape modelling, we propose the following algorithm:

1. Vary the mode weights for the first three shape components between ± 2.5 standard deviations from the mean value, leaving all other component values at

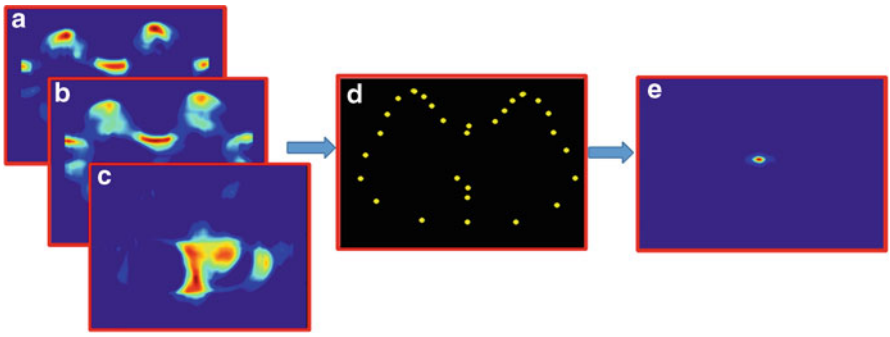

Fig. 4 (**a**), (**b**), and (**c**) are correlation maps for right nipple, sternum centre, and vertebra centre, respectively These correlation maps are translated to their position in the shape model (**d**), and then multiplied. The result of this step is the combined correlation map (**e**)

zero. We chose to vary only the first three shape modes as they are able to capture 80 % of the variation in the shape space;
2. Calculate the new shape and position of the landmarks using Eq. (1);
3. Translate the correlation maps for the individual landmarks to the position in the shape model;
4. Multiply the correlation map of the landmarks with each other to get a combined correlation map. Figure 4 shows an example of the combined correlation map. For optimal performance, the number and type of landmarks used for step 3 and 4 is explained in Sect. 3 below;
5. Select the combination of mode weights that provides the maximum combined correlation value;
6. Set the landmark points based on the shape model defined by the optimal weights determined in step 5. We refer to these as the "shape predicted landmarks".

2.5 Search the Local Region of Each Landmark for Maximum Correlation

The shape predicted landmarks provide a good initial estimate of the landmark locations but, due to the constraints of the shape model, it is not able to place all the landmarks to the point of maximum correlation. To improve accuracy, we search the correlation map of each landmark for a maximum similarity metric in a small 20 mm $\times$ 20 mm region around the shape predicted landmark location. The location corresponding to the maximum correlation is taken as the final landmark position. Figure 5 displays the improved accuracy provided by this additional step in comparison with the shape predicted landmark locations.

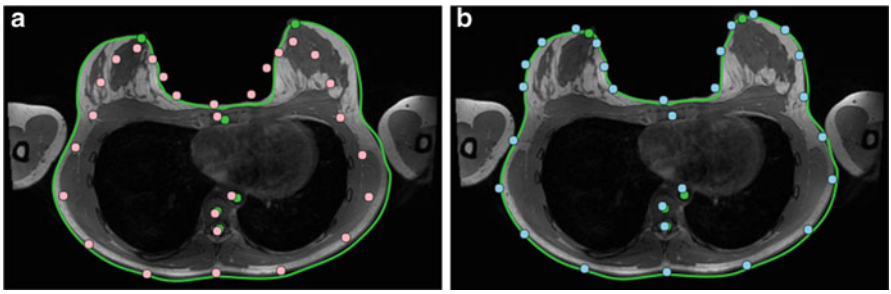

Fig. 5 Landmark matching results. In both (**a**) and (**b**), *green dots* and *green lines* represent the manually labelled landmarks and the skin surface, respectively. In (**a**), *pink dots* represent the shape predicted landmarks, which are not well aligned with the skin surface in the image. In (**b**), *blue dots* illustrate the improvement in alignment following the local search procedure

3 Results and Discussion

The criteria for success of the algorithm is the distance of the points computed using the automated methods compared to the manually labelled ground truth. For the landmarks that do not lie on the skin surface (sternum, vertebra, aorta, spinal cord, and nipples), the error was calculated as the Euclidean distance between the automatically predicted landmarks and their manually determined positions. For the skin surface landmarks, the error was calculated as the Euclidean distance between automatically detected landmarks and the closest approach to the skin surface.

3.1 Optimisation of Number of Landmarks for the Combined Correlation Map

To calculate the combined correlation map, it is not necessary to use the correlation maps for all of the landmarks. Instead, prominent landmarks that influence the overall shape can be selected to calculate the combined correlation map. This step helps to reduce computational expense. To determine the optimal number and type of landmarks, we compared the errors of the shape predicted landmarks after incrementally adding landmarks for calculating the combined correlation map. Figure 6 shows an example of how errors reduce and converge as additional landmarks are used for the combined correlation map. For Fig. 6, the order the landmarks were added is: (1) sternum; (2) spine; (3) right nipple; (4) left nipple; (5) skin surface point near right arm; (6) skin surface point near left arm; (7) skin surface point between the breasts; and (8) back skin surface point. Other combinations of landmarks were used (data not shown) but it was found that combining the first five above provided the best results.

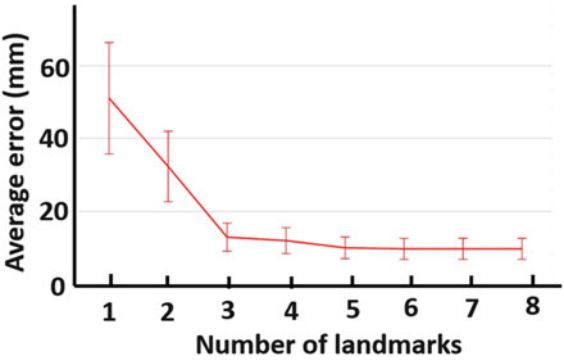

Fig. 6 Average error of the shape predicted landmarks over 30 images versus the number of landmarks used for calculating the combined correlation map. The *error bars* indicate the standard deviation in the landmark errors

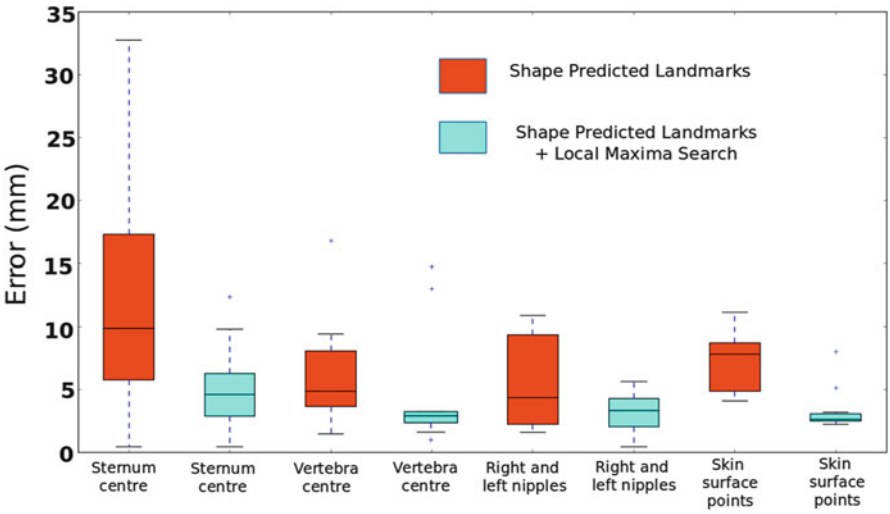

Fig. 7 Errors over 30 images for sternum centre, vertebra centre, nipples (*left* and *right*) and skin surface landmarks (24 landmarks). Skin surface point errors were calculated as the Euclidean distance between automatically detected landmarks and the closest approach to the skin surface

3.2 Landmark Matching Results

To determine the robustness and accuracy of our algorithm, a series of leave-one-out experiments was performed on thirty 2D breast MR images. The in-plane resolution of the images varied between 1.05 and 1.07 mm per pixel. Our landmark detection method succeeded in finding all 30 landmarks. The overall mean $\pm$ SD landmark error for 30 landmarks over the 30 images was 3.41 ± 2.10 mm. The mean $\pm$ SD error for the 24 skin surface landmarks was 3.3 ± 2.39 mm. The mean $\pm$ SD error for the six landmarks that do not lie on the skin surface (sternum, vertebra, aorta, spinal cord and nipples) was 4.1 ± 2.26 mm. Among these six landmarks, the smallest error was for the vertebra centre (3.1 ± 2.91 mm), while the largest error

was for the sternum centre (5.3 ± 3.5 mm). In Fig. 7, we compare the results of our method with the shape predicted landmarks. This comparison shows the improvement provided by the local maximum search in comparison with the shape predicted landmarks.

4 Conclusion

We have presented a novel algorithm to automatically find landmarks on the skin surface and other point landmarks for MR images. Our algorithm combines template matching and statistical shape modelling in a single framework to provide robust and accurate landmark detection for use to generate skin surface meshes. We plan to extend this method to three dimensions. Furthermore, active appearance models will be used to generate more precise correlation maps. We will determine whether this will result in more accurate landmark positioning for both shape predicted landmarks and, more importantly, the final landmark positions predicted by the local maximum search.

References

1. Gamage, T.P.B., Rajagopal, V., Nielsen, P.M., Nash, M.P.: Patient-specific modelling of breast biomechanics with applications to breast cancer detection and treatment. In: Patient-Specific Modelling in Tomorrow's Medicine. pp. 379–412 (2012)
2. Mostayed, A., Garlapati, R.R., Joldes, G.R., Wittek, A., Roy, A., Kikinis, R., Miller, K.: Biomechanical model as a registration tool for image-guided neurosurgery: evaluation against B-spline registration. Ann. Biomed. Eng. **41**(11), 2409–2425 (2013)
3. Criminsi, A., Shotton, J., Bucciarelli, S.: Decision forests with long range spatial context for organ localisation in CT volumes. In: Medical Image Computing and Computer-Assisted Intervention (MICCAI), pp. 69–80 (2009)
4. Potesil, V., Kadir, T., Platsch, G., Brady, M.: Improved anatomical landmark localization in medical images using dense matching of graphical models. In: British Machine Vision Conference (BMVC), pp. 1–10 (2010)
5. Worz, S., Rohr, K.: Localization of anatomical point landmarks in 3D medical images by fitting 3D parametric intensity models. Med. Image Anal. **10**(1), 41–58 (2006)
6. Rohr, K.: Extraction of 3D anatomical point landmarks based on invariance principles. Pattern Recognit. **32**, 3–15 (1999)
7. Hartkens, T., Rohr, K., Stiehl, H.S.: Evaluation of 3D operators for the detection of anatomical point landmarks in MR and CT images. Comput. Vis. Image Underst. **86**(2), 118–136 (2002)
8. Frantz, S., Rohr, K., Stiehl, H.S.: Development and validation of a multi-step approach to improved detection of 3D point landmarks in tomographic images. Image Vis. Comput. **23**(11), 956–971 (2005)
9. Cootes, T.F., Taylor, C.J.: Statistical models of appearance for medical image analysis and computer vision. In: Medical Imaging, International Society for Optics and Photonics. pp. 236–248 (2001)

Mechanical Properties of Brain–Skull Interface in Compression

Sudip Agrawal, Adam Wittek, Grand Joldes, Stuart Bunt, and Karol Miller

1 Introduction

Advancement in computing technology has accelerated interest in numerical modelling of brain for application in various fields like surgery simulation, computer-aided and image-guided surgery [1]. A typical example of modelling and simulation of brain is to compute craniotomy-induced brain shift that results in movement of tumour and healthy brain tissue. Such application involving deformation requires material properties of various tissues and components inside cranium, and loading and boundary condition for accurate results. In brain modelling, the mechanical properties of brain–skull interface determine the boundary condition. However, the existing quantitative data regarding the mechanical properties of the brain–skull interface, the complex comprising the meninges, skull and fluid-filled spaces in-between them, are very limited.

A number of studies have been conducted to determine the mechanical properties of brain tissue. Those studies have established that brain tissue is a very soft, non-linearly viscoelastic solid material, with very low linear viscoelastic strain limit (of the order of 0.1–0.3 %) [1]. However, there is no consensus regarding material properties of the brain–skull interface. Different research groups have implemented

S. Agrawal (✉) • A. Wittek • G. Joldes • K. Miller
Intelligent System for Medicine Laboratory (ISML), School of Mechanical Engineering, The university of Western Australia, Crawley-Perth 6009, WA, Australia
e-mail: sudip.agrawal@research.uwa.edu.au

S. Bunt
School of Anatomy, Physiology and Human Biology, The University of Western Australia, Crawley-Perth, 6009, WA, Australia

B. Doyle et al. (eds.), *Computational Biomechanics for Medicine*,
DOI 10.1007/978-3-319-15503-6_8

different ideas to address the issue in their model. Some assume the brain to be fixed to the surface of the skull [2, 3], while some use a gap between the brain and skull allowing motion of brain within the cranial cavity [4–9] and others use a frictionless sliding contact model [10, 11].

Anatomically the brain–skull interface is comprised of rigid cranial inner surface (also referred to as inner table), the meninges and the outer brain surface. The meninges are comprised of dura mater, arachnoid mater and pia mater [12]. The dura mater is attached to the skull. It consists of periosteal dura, meningeal dura and dural border. The connection between arachnoid and meningeal dura is established through the dural border and arachnoid border cells. From arachnoid mater's inner surface its fibres (arachnoid trabeculae) extend to the subarachnoid space (SAS) and becomes continuous with the pia mater. The pia mater is a thin delicate membrane which is attached to the brain outer surface. There is a fluid-filled space between the dural surface of arachnoid matter and the pia mater because arachnoid mater doesn't follow the contours of the brain like the pia mater. However the exact anatomical structure of this interface is still hotly debated [12]. A detailed representation of the brain–skull interface is shown in Fig. 1.

In this study we have conducted ex vivo uniaxial compression tests on a sample containing skull, meninges and brain and the simulations of the experiment to establish mechanical behaviour and properties of brain–skull interface. All the necessary ethical approvals were obtained prior to the experiment from Animal Ethics Committee, University of Western Australia (UWA). The approach ensured we could examine brain–skull interface in its closest natural state in a controlled study.

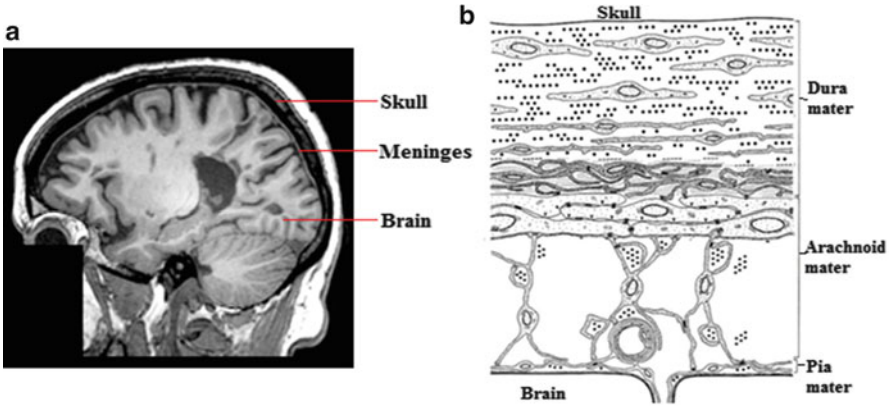

Fig. 1 Brain–skull interface (**a**) lateral section through human head showing the brain and surrounding tissue (taken from NAMIC registration case inventory brain) (**b**) detailed representation of the meninges (modified from Haines et al. [12])

2 Materials and Methods

2.1 Sample Preparation

Sheep heads were collected from Royal Perth Hospital (RPH), Perth. The specimens were taken as by-product of anaesthesia training programme. They were sacrificed using high dose of triple drip (a combination of xylazine, ketamine and guaifenesin, all anaesthetics compound). They were transported to the testing facility in a sealed container and stored at 4° C before further processing and testing. Samples were tested within 24 h from the time of death to reduce variability due to post-mortem changes [13]. The specimens were not frozen at any time.

The heads were skinned and a rectangular cut of $\sim 30 \times 30$ mm was made on the skull on top of the cranium (above cerebrum) using vibrating saw. Adjoining cut of $\sim 30 \times 10$ mm was also made. Using a microtome blade (Feather s35) the underlying brain was cut vertically in sagittal and coronal plane through the opening in skull. The smaller of the skull was removed along with the underlying brain tissue using forceps and scalpel to create an opening into cranium and the sample. From the opening, a horizontal cut (in transverse plane) was made in the brain leaving approximately 12 mm of tissue attached to skull using a bent razor blade. The free specimen was lifted out from the skull with the blade to ensure minimal damage to the meninges. The skull was set on epoxy putty (Selleys Knead It Multipurpose) base to roughly level the four corners of skull. The putty set in 10 min. The top surface of the brain was carefully levelled using microtome blade. $\sim$5 mm of brain tissue from all edges was removed using microtome blade and scalpel to ensure we discarded damaged meninges and tissues in the edges that may have been caused by the vibrating saw. This formed our test sample (with brain–skull interface). The process can be seen in Fig. 2a–g.

The resulting sample had brain tissue resting on skull with brain–skull interface intact. The width of the faces of brain tissue, position of four corners in contact with the skull and height at the corner of sample were measured. The widths of the faces of the samples were taken midway between the base and the top surface of brain tissue.

2.2 Experimental Set-Up

Uniaxial compressions of the samples were performed in set-up shown in Fig. 3. The experiment was done in a testing device developed in-house [14]. The displacement of impermeable loading plate was done by Haydon Kerk Linear actuator 43F4A-3.22-099, a stepper motor screw drive actuator. It has a displacement control of 7.9 μm per step and allowed loading velocities of 0.001–5 mm/s. The displacement was measured by MTS CS core sensor with analog output. The forces were

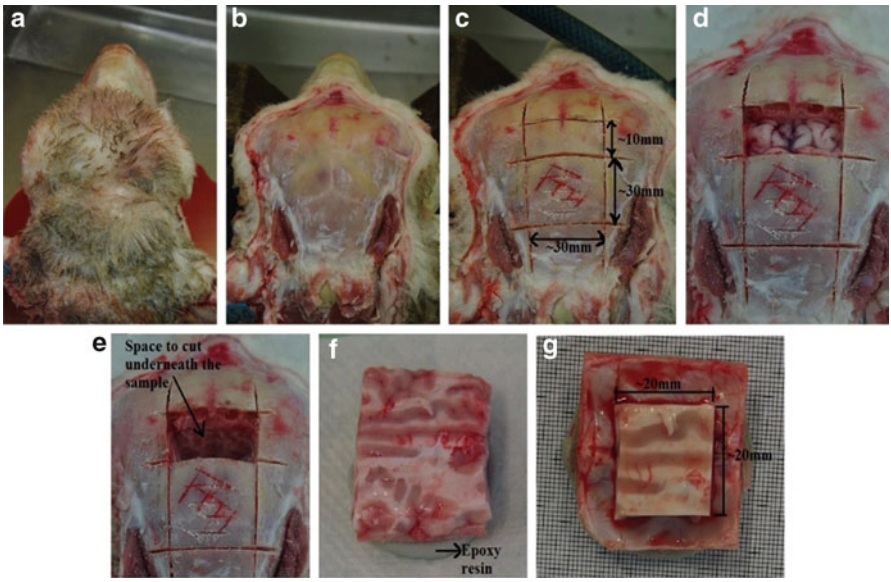

Fig. 2 Sample preparation (**a**) head (**b**) skinned for extraction (**c**) skull cut using vibrating saw, *lower* ∼30 × 30 mm and *upper* ∼10 × 30 (**d, e**) smaller free skull and brain removed (**f**) sample extracted and mounted in epoxy resin (**g**) complete sample A

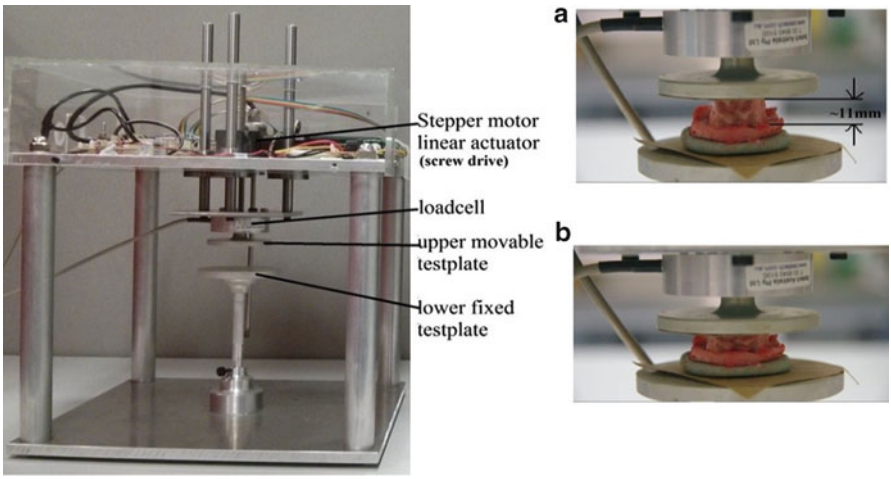

Fig. 3 Experimental set-up (**a**) sample before compression (**b**) sample after compression

measured by Burster 8523-20 0-20N loadcell with linear output in the required range of 1 N with error less than 0.15 % [14]. The experiment was documented using Pentax K5 camera with FA 50 mm f1:1.4 lens. The images were used to study deformation of samples after the experiment.

2.3 Experimental Protocol

The experimental protocol follows Miller and Chinzei [15]. The samples were compressed between two impermeable platens in a semi-confined uniaxial set-up. No preconditioning was done to the samples.

Tests were done at two different loading speeds 1 and 0.01 mm/s. The tests were performed at room temperature as suggested by literature [13, 15, 16]. The movement of the platen began about 0.5 mm above the sample and care was taken that the sample didn't touch the loading platen before compression started. The samples were compressed about 3 mm corresponding to approximate strain of 0.3. 120 grid sand papers were glued to both the platens to ensure no relative movement occurs between sample and loading plates, so no slip boundary condition could be used in the analysis.

The linear stepper motor, screw drive actuator had very high acceleration and hence the loading velocity was assumed to be achieved instantaneously.

2.4 Analysis

Dimensions of brain tissue in both the samples were measured. Geometry of internal surface of skull was required to create a model for both samples. After the experiment, the brain tissue and meninges were scraped from the skull and the internal surface of the skull was scanned using MODELA MDX-20 Scanner. The scanned surface of skull and the initial dimensions of the brain tissue were used to create models of the samples. Side walls of brain were assumed to be orthogonal and the top surface was assumed to be parallel to sample resting plane. Skull was assumed to be rigid body as it was orders of magnitude stiffer than brain tissue. Computational grid was created on the geometry. All the pre-processing of the model including mesh generation was done using Altair HyperMesh. The brain tissue was modelled using the Ogden-type [17]. Hyperelastic model as proposed by Miller and Chinzei [16].

$$W = \frac{2\mu}{\alpha^2}\left(\lambda_1^{\alpha} + \lambda_2^{\alpha} + \lambda_3^{\alpha} - 3\right) \tag{1}$$

where W is strain energy potential, λ_i principal stretches, μ relaxed shear modulus and α material coefficient. The experiment was simulated by applying fixed boundary condition at the skull and prescribed displacement at top surface of brain as shown in Fig. 4. The interface was simulated as friction less sliding contact. Loading surface reaction force-time relation was obtained from simulation using ABAQUS™ was matched close to data measured by the experiment to determine coefficients μ and α following Morriss et al. [18]. This formed subject specific material property of brain tissue for the sheep from which the sample was taken.

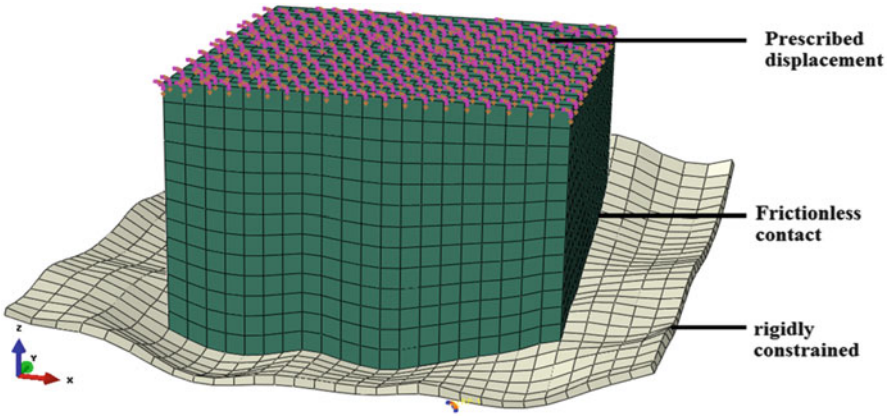

Fig. 4 Rigid skull (*white*) constrained in all direction at reference point and brain tissue (tissue) loading by displacement of nodes in z direction and constrained in x and y axes

The width of sample after the test was obtained from images of the experiment. Any lens distortion was corrected using camera software (Camera's JPEG engine) distributed by manufacturer (Ricoh, Japan). The width of each pixel was estimated using initial width measured and image before loading. It was compared with the results from simulation.

3 Results

Comparison of force vs time relation from the experiments and modelling is presented in Fig. 5 for both the samples. Corresponding material parameters and loading speed for the samples are listed in Table 1.

For compression of up to 3 mm (∼0.3 strain) the model can predict force magnitude with error less than 5 %. Comparison of width of side monitored by video with the modelling result along with initial width is presented in Table 2. The interface was represented by friction less sliding contact. The data showed there has good correlation between measured and predicted width for the two test samples.

4 Discussion

In this study, we presented results of compression experiment on samples containing sheep's skull, meninges and brain and evaluated behaviour of brain–skull interface through use of non-linear finite element modelling. To obtain the properties and behaviour of interface we performed uniaxial compression experiment on the tissue sample under controlled condition. Base of skull and top of brain were fixed

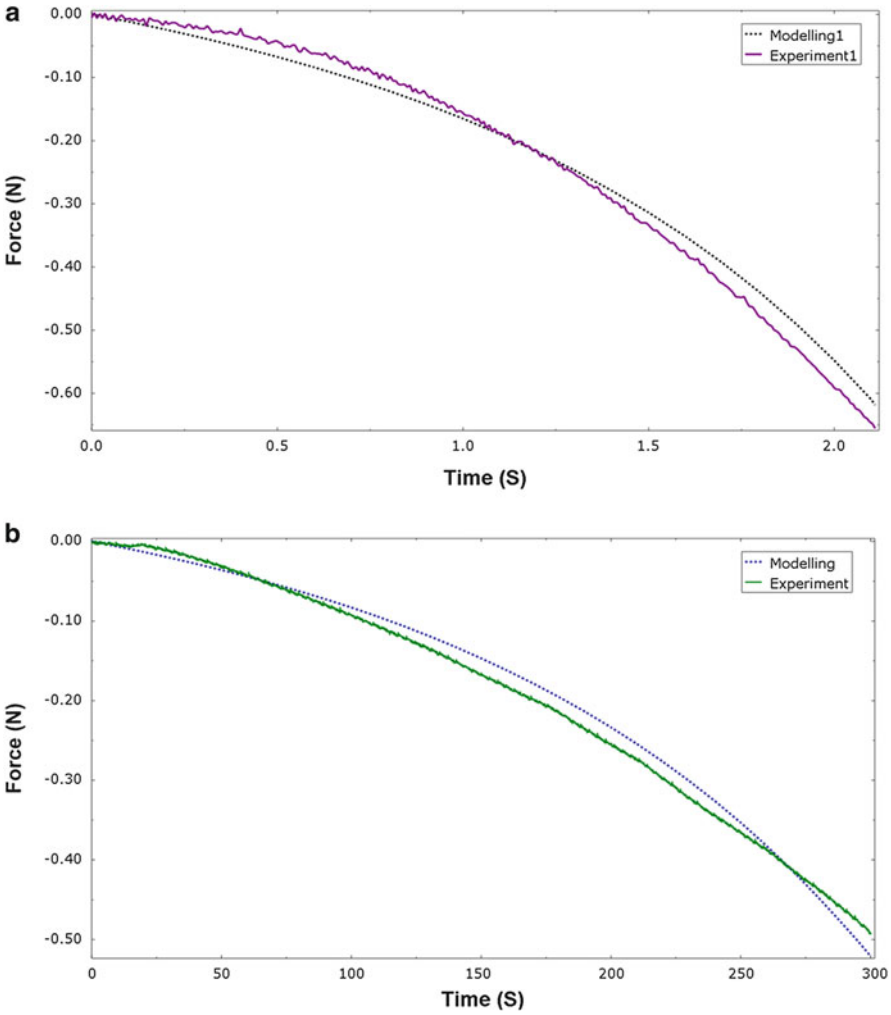

Fig. 5 Uniaxial compression of samples: comparison of modelling and experimental results (**a**) loading speed 1 mm/s (**b**) loading speed 0.01 mm/s

to impermeable testing platens to implement non-slip boundary condition during analysis. We measured initial width of faces brain tissue of sample and utilized video and image of the experiment to obtain width of a face after the compression. A model of sample was created where the skull, treated as rigid object, was fixed on a reference point and the compression of sample was achieved by nodal displacement of nodes on upper surface of brain. The brain–skull interface was modelled as friction less contact interaction between brain and skull. The finite element model accurately predicted the compressive forces (Fig. 5) and changes in width of the face of sample (Table 2).

Table 1 Odgen type hyperelastic material constants for tissue samples by calibrating the model using ABAQUS finite element solver

Sample	Loading speed (mm/s)	μ (Pa)	α
a	1	790	−6.3
b	0.01	600	−6.3

Table 2 Comparison of width of monitored side of brain tissue

		Final width (mm)		
Loading speed (mm/s)	Initial width	Experiment	Simulation	Difference (mm)
1	18.99	20.65	20.85	0.20
0.01	20.47	21.93	21.90	0.03

We hypothesize that the minor discrepancies between the modelling and experimental result could be attributed to minor inaccuracies in determining the geometry of brain and skull surface. The sample was manually prepared using by hand using tools like scalpel blade and razor blade and contained unevenness reducing the geometric and measured dimension accuracy to about 1 mm. This also affected image processing to obtain final width of the face.

A limitation of our study is the number of experiments conducted. The preparations of samples were very challenging and delicate process and it resulted in a lot of damaged samples during the testing. Another limitation is as the experiment is ex vivo, we assume some of the cerebrospinal fluid (CSF) leaks from the meninges. Hence this approach may not be sufficient to represent brain–skull interface during very high speed impacts where fluids may have greater relevance. We observed that deformation shape of sample was mainly dictated by the geometry of skull. Depending on slope of skull surface in contact with brain, the deformation tends to be more toward the inclination of the surface. For further validation and improvement of the model more experiment needs to be conducted and feature or deformation has to be tracked and compared in 3D to have better correlation with simulation on a number of samples.

The study presents experimental results with quantitative assessment of brain–skull interface compression to determine its properties. The result suggests that frictionless contact can replicate brain–skull interaction of the samples in compression, when brain presses against the skull, at low loading speeds.

Acknowledgements The first author of this paper is supported by Australian Postgraduate Award and UWA safety-Net Top-Up Scholarship. The financial support of Australian Research Council (Discovery Grant No. DP120100402) and National Health and Medical Research Council (Grant No. APP1063986) is gratefully acknowledged.

References

1. Miller, K.: Biomechanics of the Brain. Springer (2011)
2. Hagemann, A., Rohr, K., Stiehl, H.S., Spetzger, U., Gilsbach, J.M.: Biomechanical modeling of the human head for physically based, nonrigid image registration. IEEE Trans. Med. Imaging **18**(10), 875–884 (1999)
3. Miga, M.I., Paulsen, K.D., Hoopes, P.J., Kennedy Jr., F.E., Hartov, A., Roberts, D.W.: In vivo quantification of a homogeneous brain deformation model for updating preoperative images during surgery. IEEE Trans. Biomed. Eng. **47**(2), 266–273 (2000)
4. Wittek, A., Miller, K., Kikinis, R., Warfield, S.K.: Patient-specific model of brain deformation: application to medical image registration. J. Biomech. **40**(4), 919–929 (2007)
5. Dutta-Roy, T., Wittek, A., Miller, K.: Biomechanical modelling of normal pressure hydrocephalus. J. Biomech. **41**(10), 2263–2271 (2008)
6. Wittek, A., Omori, K.: Parametric study of effects of brain-skull boundary conditions and brain material properties on responses of simplified finite element brain model under angular acceleration impulse in sagittal plane. JSME Int. J. Ser. C Mech. Syst. Mach. Elem. Manuf. **46**(4), 1388–1399 (2003)
7. Wittek, A., Hawkins, T., Miller, K.: On the unimportance of constitutive models in computing brain deformation for image-guided surgery. Biomech. Model. Mechanobiol. **8**(1), 77–84 (2009)
8. Wittek, A., Kikinis, R., Warfield, S., Miller, K.: Brain shift computation using a fully nonlinear biomechanical model. In: Duncan, J., Gerig, G. (eds.) Medical Image Computing and Computer-Assisted Intervention – MICCAI 2005, pp. 583–590. Springer, Berlin/Heidelberg (2005).
9. Hu, J., Jin, X., Lee, J.B., Zhang, L., Chaudhary, V., Guthikonda, M., Yang, K.H., King, A.I.: Intraoperative brain shift prediction using a 3D inhomogeneous patient-specific finite element model. J. Neurosurg. **106**(1), 164–169 (2007)
10. Joldes, G.R., Wittek, A., Miller, K., Morriss L.: Realistic and Efficient Brain-Skull Interaction Model for Brain Shift Computation (2008)
11. Joldes, G.R., Wittek, A., Miller, K.: Suite of finite element algorithms for accurate computation of soft tissue deformation for surgical simulation. Med. Image Anal. **13**(6), 912–919 (2009)
12. Haines, D.E., Harkey, H.L., Al-Mefty, O.: The "Subdural" space: a new look at an outdated concept. Neurosurgery **32**(1), 111–120 (1993)
13. Rashid, B., Destrade, M., Gilchrist, M.D.: Influence of preservation temperature on the measured mechanical properties of brain tissue. J. Biomech. **46**(7), 1276–1281 (2013)
14. Agrawal, S., Wittek, A., Bunt, S., Miller K.: Portable experimental device for determining the mechanical properties of brain-skull interface.http://school.mech.uwa.edu.au/ISML/archive/reports/isml-no-01-2014.pdf (2014)
15. Miller, K., Chinzei, K.: Constitutive modelling of brain tissue: experiment and theory. J. Biomech. **30**(11–12), 1115–1121 (1997)
16. Miller, K., Chinzei, K.: Mechanical properties of brain tissue in tension. J. Biomech. **35**(4), 483–490 (2002)
17. Ogden, R.W.: Large deformation isotropic elasticity: on the correlation of theory and experiment for compressible rubberlike solids. In: Proceedings of the Royal Society of London. Series A, Mathematical and Physical Sciences, vol. 328, no. 1575, pp. 567–583 (1972)
18. Morriss, L., Wittek, A., Miller, K.: Compression testing of very soft biological tissues using semi-confined configuration—a word of caution. J. Biomech. **41**(1), 235–238 (2008)

Modelling the Deformation of the Human Cornea Produced by a Focussed Air Pulse

Nouran Bahr, Noor Ali, Dipika Patel, Charles McGhee, Peter Hunter, and Harvey Ho

1 Introduction

The cornea is a transparent, avascular structure that forms the anterior part of the eye. The normal mean corneal diameter is 11.7 mm horizontally and the cornea is thinnest centrally, gradually increasing in thickness towards the periphery, with mean values of 0.52 mm and 0.67 mm, respectively, [1]. The cornea is subject to a number of forces, including the internal eye pressure, termed intraocular pressure (IOP), and external atmospheric pressure (Fig. 1a). The mechanical properties of the cornea are predominantly defined by the corneal stroma, which contributes to 90 % of the corneal thickness [2].

Accurate measurement of IOP is crucial in the diagnosis and management of glaucoma, a common, potentially blinding eye disease [3]. The thickness and biomechanical properties of the cornea are known to significantly influence IOP measurement [3]. Many models for the cornea have been proposed (for reviews, see [2, 4]), which recruit various constitutive equations to describe the nonlinear anisotropic mechanical properties of the cornea (for a review, see [2]). Their results are often compared and validated using tonometers (devices for measuring IOP in clinical practice).

Recently a new, non-contact tonometer (Corvis ST, Oculus, Wetzlar, Germany) (Fig. 1) has become commercially available. This device uses an ultra-high-speed Scheimpflug camera (4,330 frames/s) to visualize and measure the corneal deformation response to an air pulse [5], which yields the mechanical properties of cornea

N. Bahr • P. Hunter • H. Ho (✉)
Auckland Bioengineering Institute, University of Auckland, Auckland, New Zealand
e-mail: harvey.ho@auckland.ac.nz

N. Ali • D. Patel • C. McGhee
Faculty of Medical and Health Sciences, Department of Ophthalmology, New Zealand National Eye Centre, University of Auckland, Auckland, New Zealand

B. Doyle et al. (eds.), *Computational Biomechanics for Medicine*,
DOI 10.1007/978-3-319-15503-6_9

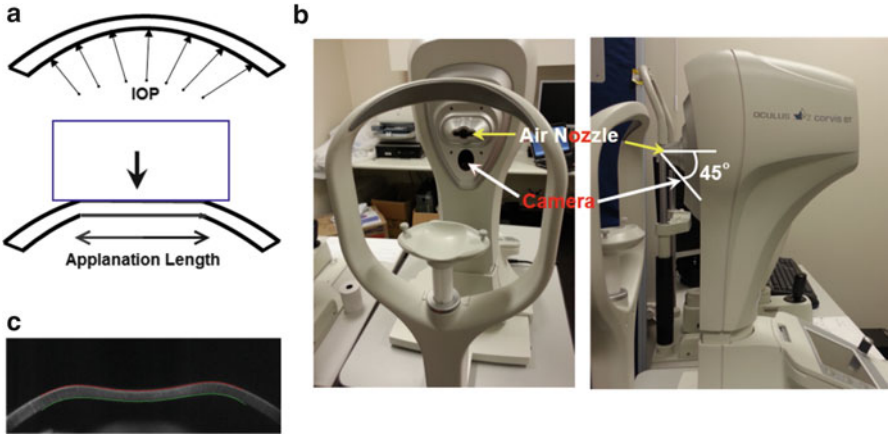

Fig. 1 (**a**) Illustration of the cornea, the IOP and applanation length; (**b**) the Corvis device from two different angles; (**c**) the cornea image it takes

implicitly. This new technique poses challenges to current finite element models (FEMs) which provide alternative means to understand cornea properties, as both the fluid and solid domains need to be solved, with the forces updated across their moving boundaries. The aim of this study was to develop an initial FSI model and to establish some basic parameters for future wide scale studies.

2 Methods

2.1 Medical Imaging

The Corvis ST device was used to measure the corneal deformation in an adult, male volunteer. The fast motion of the cornea under the air puff (duration ∼25 ms) was captured by an ultra-fast camera into a slow motion video. A series of images were selected from the video for further analysis and comparison with our model. The image with the highest concavity is shown in Fig. 1c. Note that the camera was not vertically facing the cornea but placed at a 45° angle towards the cornea [5]. Other relevant data collected included the corneal thickness, IOP, deformation amplitude, applanation length, and corneal velocity.

2.2 Geometry Modelling

The Corvis system was simplified as a working domain consisting of a nozzle, a cornea, and an air space. Their respective geometric modelling is described below.

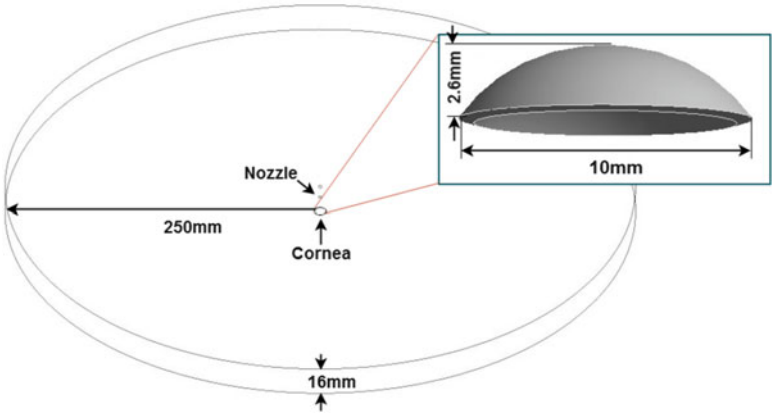

Fig. 2 The entities in the working domain: the open space, the nozzle, and the cornea

2.2.1 Air Space

The air field was designed as an open space consisting of a circular enclosure (500 mm in diameter, 16 mm in height) where the nozzle and the cornea were placed at the centre (Fig. 2). The space was designed to be much larger than the cornea to avoid the influence of rebounding air flow from the wall.

2.2.2 Cornea

Taking the measurements made by the Corvis ST device into account, the cornea was modelled as a dome-shaped elastic solid. We used a constant thickness of 0.52 mm, a horizontal diameter of 10 mm, and a vertical height of 2.6 mm to approximate the cornea in this initial work (Fig. 2).

2.2.3 Air Nozzle

The nozzle was configured as a hollow pipe 3.08 mm in diameter placed 11 mm from the cornea, as per the Corvis manual [5].

Using the grid generator within ANSYS, an adaptive mesh was generated for the air space where the smallest element size was 1 mm. A fine mesh was created at a region under the nozzle and the discharging area. The final fluid mesh contained 4,784,871 tetrahedron elements and 844,235 nodes, the cornea mesh contained 44,409 elements and 70,148 nodes (Fig. 3).

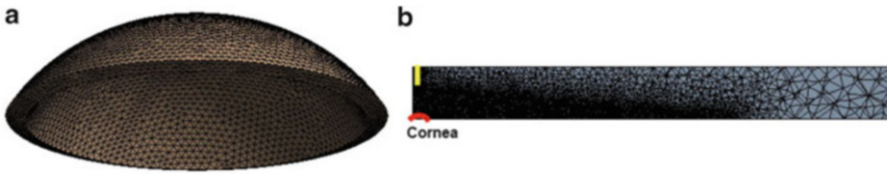

Fig. 3 Computational grid for: (**a**) the cornea; (**b**) the enclosure space (adaptive mesh)

2.3 Biomechanics Modelling

2.3.1 Fluid Solver

With the aim of modelling air flow through a pipe and the resulting effect on the cornea. The ANSYS CFX software was used for air flow simulation. A κ-ω turbulence model was used for flow modelling. The flow was treated as transient and the highest flow velocity from the outlet of the nozzle was set as 80 m/s. Therefore the airflow had a brief and strong pressure impact on the cornea. The wall was treated as outlet of the domain.

The air flow was treated as transient so that the airflow had a brief and strong pressure impact on the cornea. The jet inflow from the nozzle was approximated by a sinusoidal wave (Fig. 4). A κ-ω model was used for air turbulence modelling.

2.3.2 Solid Solver

With different fibre orientations in the corneal centre and periphery, the mechanical properties of the cornea are very complex. In this work we employed a much simpler Neo-Hookean strain energy function:

$$W = \frac{\mu}{2}(\bar{I}_1 - 3) + \frac{1}{d}(J-1)^2, \tag{1}$$

where μ is the initial shear modulus, d is the incompressibility parameter, $\bar{I}_1$ is the invariant of the Cauchy–Green deformation tensor, J is the determinant of the elastic deformation gradient. The shear modulus (=100 kPa) was computed using the relationship:

$$\mu = \frac{E}{2(1+\nu)}, \tag{2}$$

where a Young's modulus $E = 225{,}000$ Pa and a Poisson's ratio $\nu = 0.49$ were assumed in all calculations (refer to [2] $E = 0.3$ MPa, $\nu = 0.49$). The ANSYS interface requires the initial shear modulus and the incompressibility parameter to be specified. The remainder are automatically computed and exploited by the software to fit the model to the experimental data.

2.3.3 FSI Framework

The FSI framework within ANSYS is built upon a multi-field analysis (MFX) solver. In brief, within each time step there is a stagger loop whose number of iterations is determined by the convergence of the load transfer between fields or the maximum number of stagger iterations specified [6].

Since the movement of the cornea is insignificant compared with the enclosure size, a one-way fluid–structure analysis was performed, i.e., the transient air force working on the cornea was solved in CFX at first. The computed data are then passed to the structure solver.

2.3.4 Boundary Conditions

The boundary conditions for the fluid and solid solvers are summarized as below:

- A transient outflow profile of 30 m/s was applied at the nozzle (as inflow to the air space);
- The highest flow velocity from the nozzle was set as 80 m/s [5];
- The wall of the enclosure was treated as outlet of the domain;
- A fixed support was configured at the periphery, preventing rotation and translation of the cornea;
- A constant normal pressure of 1 kPa against the cornea wall was also applied to mimic the effect of IOP (normal 1.5 kPa).

Note that the above boundary conditions were set as close to reality as possible. However there were also some simplification treatments, e.g., the fixed periphery condition, to ease the numeric simulations.

3 Results

3.1 Simulation of Air Jet Flow

The transient air flow dynamics was solved within 5.5 h on a desktop computer (Intel Core Quad CPU @ 2.5 GHz) for a simulation of 30 ms. The computer solutions were exported at 20 time steps. Figure 4a shows the jet flow velocity at $t = 15$ ms, where the highest velocity ($\sim$80 m/s) occurred at the air flow centre just below the nozzle (as the boundary condition). After hitting the cornea the air pulse was discharged at a velocity of $\sim$40 m/s. Of particular interest were the pressure forces acting on the cornea, which are shown in Fig. 4b. It can be seen that the highest pressure force acting on the cornea was at its centre at $\sim$2.3 kPa, whereas the pressure was negative at the corneal periphery, due to the IOP (1 kPa) acting from the opposite direction. These raw load data were passed to the solid solver for structural analysis, as described below.

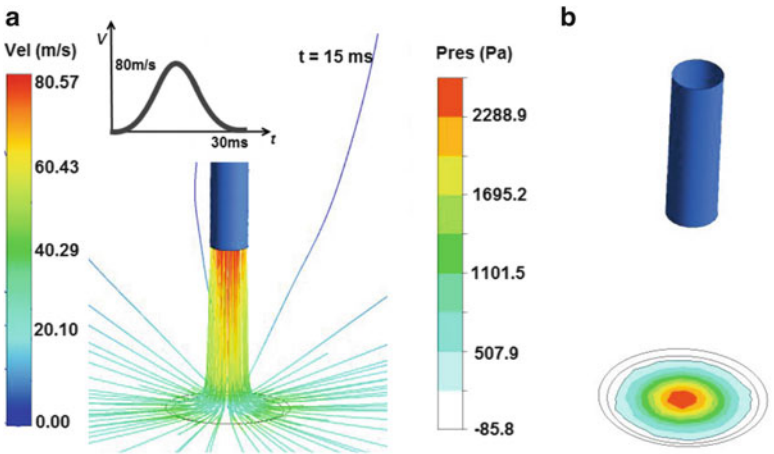

Fig. 4 (**a**) Air flow velocity along the flow streamlines; (**b**) the pressure force acting on the cornea. Note that the pressure at the edge of the cornea (coloured in *white*) was negative due to IOP acting from the opposite direction

3.2 Simulation of Corneal Deformation

Figure 5a provides the in vivo data for the applanation length and the maximum concavity given by the Corvis ST device. In comparison, it can be seen from Fig. 5b that the applanation length yielded from the model was ~2.6 mm, which agreed with that measured by the Corvis ST device (2.5 mm). The curve of the deformation of apex (cornea centre) shows that the largest amplitude was 1.1 mm ($t = 17$ ms) from the Corvis data, whilst our model result suggested a similar maximum amplitude of 0.9 mm ($t = 15$ ms).

A comparison was also made between the image sequence of cornea deflection and that simulated from our model (Fig. 6). The similarity of the concavity of cross section, the thickness of cornea and the applanation length were confirmed in the comparison, yet our model was able to yield more "hidden" information such as the stress and strain that the cornea was subjected to.

4 Discussion

Understanding the biomechanical behaviour of the cornea offers a wide variety of applications including the diagnosis of glaucoma and the detection of eye diseases. Previous works modelled deformation of the cornea subject to a uniformly distributed solid object load, with various material properties proposed. However, a different approach is necessary to estimate the deformation induced by a focussed air pulse. The purpose of this study was to apply an FSI analysis for this problem.

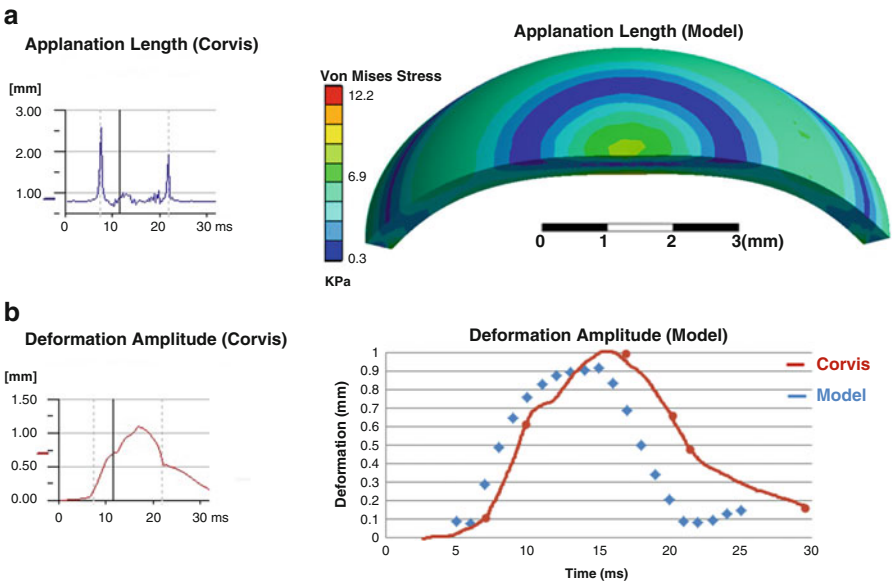

Fig. 5 Comparison between the Corvis measurement and the model: (**a**) applanation length—Corvis: 2.5 mm, model—2.6 mm; (**b**) the deformation amplitude of apex—Corvis: 1.1 mm, model: 0.9 mm

The model was validated against test data obtained in vivo, in particular against the video captured by the device's ultra-fast camera. To our knowledge, this study represents the first FSI model for non-contact corneal deformation.

The complex microstructure of the cornea was simplified to an isotropic material recruiting the nonlinear Neo-Hookean constitutive equation, as focus has not been placed on testing sophisticated material laws at this stage, but rather on establishing the FSI pipeline. Neither did we consider the time-dependent strain for this basic model. Nevertheless the current work could be extended by taking into account important variables, including: varying corneal thickness, non-homogeneity, corneal-scleral connection, and scleral deformation as the cornea deforms.

Further collaboration between ophthalmic clinician-scientists and bioengineers will be beneficial in enhancing the current model. For example, corneal biomechanical properties are known to be significantly altered in keratoconus [7], a non-inflammatory disease in which the cornea assumes a conical shape due to thinning and protrusion resulting in the possibility of corneal transplantation. The diagnosis of keratoconus is usually made on the basis of a combination of clinical and computerized corneal tomographic signs. However, early cases are notoriously difficult to detect. By assessing biomechanical properties in vivo coupled with computer modelling, the Corvis ST is a potentially useful adjunctive tool in the diagnosis of keratoconus.

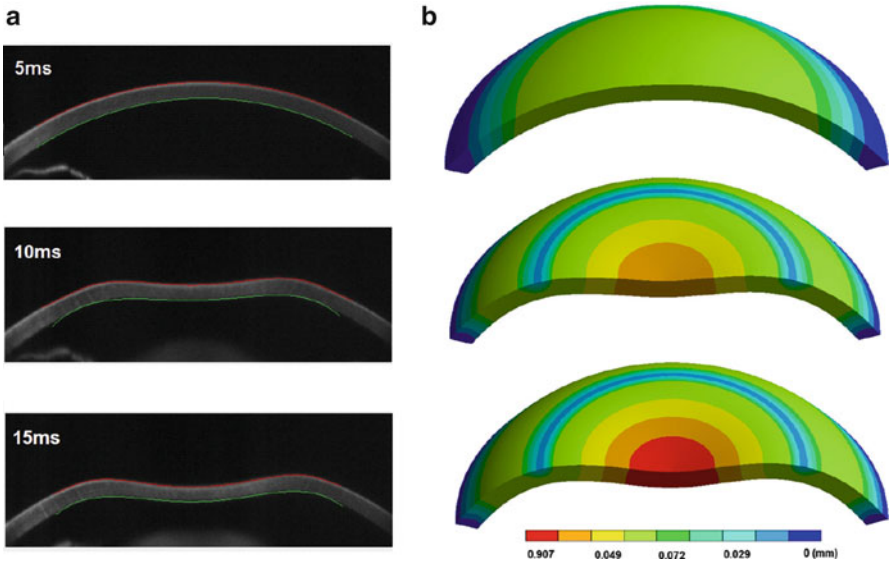

Fig. 6 (**a**) The cross section of the cornea at three time steps (5, 10, and 15 ms, respectively); (**b**) the corresponding corneal deflection simulated from our model

5 Conclusion

This study reports a fluid–structure interaction (FSI) model to describe the deformation of the human cornea under a focussed air pulse. The simulation results were validated against in vivo data derived from the Corvis ST device. The model has a range of potential applications in understanding corneal biomechanical properties in health and disease, and in the diagnosis and management of corneal pathology.

References

1. Bron, A.J., Tripathi, R.C., Tripathi, B.J.: The cornea and sclera. In: Wolff's Anatomy of the Eye and Orbit, 8th edn. Chapman & Hall Medical, London (1997)
2. Pandolfi, A., Manganiello, F.: A model for the human cornea: constitutive formulation and numerical analysis. Biomech. Model. Mechanobiol. **5**(4), 237–246 (2006)
3. Browning, A.C., Bhan, A., Rotchford, A.P., Shah, S., Dua, H.S.: The effect of corneal thickness on intraocular pressure measurement in patients with corneal pathology. Br. J. Ophthalmol. **88**(11), 1395–1399 (2004)
4. Pinsky, P.M., Datye, D.V.: A microstructurally-based finite element model of the incised human cornea. J Biomech. **24**(10), 907–922 (1991)
5. OCULUS: Corvis ST instruction manual (2011)
6. ANSYS: ANSYS CFX-Solver, Release 10.0: Theory. ANSYS Europe Ltd. (2005)
7. Nash, I.S., Greene, P.R., Foster, C.: Comparison of mechanical properties of keratoconus and normal corneas. Exp. Eye Res. **35**(5), 413–424 (1982)

Biomechanical Modeling of the Respiratory System: Human Diaphragm and Thorax

Hamid Ladjal, Joseph Azencot, Michael Beuve, Philippe Giraud, Jean Michel Moreau, and Behzad Shariat

1 Introduction

One of the major difficulties in radiotherapy is the treatment of moving tumors. Tumor motion during irradiation reduces the coverage target and increases dose deposition to healthy tissues. The respiratory motion modifies both the shape and position of internal organs. This is liable to degrade the quality of radiation treatment of cancer. Moreover, in the case of a four-dimensional radiotherapy treatment plan aiming to estimate the evolution of the dose distribution during the respiratory cycle, not only the position of the organs but also the deformations of the tissues throughout the respiratory cycle need to be estimated. Prediction of respiratory motion has the potential to substantially improve cancer radiation therapy. As of now, a full-four dimensional continuous imaging of the internal anatomy of the patient during the treatment procedure is not yet feasible.

H. Ladjal (✉)
LIRIS, Laboratoire d'InfoRmatique en Image et Systèmes d'information CNRS UMR 5205, University of Lyon, Université Claude Bernard Lyon 1, Villeurbanne, France

IPNL CNRS UMR 5822, University of Lyon, Université Claude Bernard Lyon 1, 69622, Villeurbanne, France
e-mail: hamid.ladjal@liris.cnrs.fr

J. Azencot • J.M. Moreau • B. Shariat
LIRIS, Laboratoire d'InfoRmatique en Image et Systèmes d'information CNRS UMR 5205, University of Lyon, Université Claude Bernard Lyon 1, Villeurbanne, France

M. Beuve
IPNL CNRS UMR 5822, University of Lyon, Université Claude Bernard Lyon 1, 69622, Villeurbanne, France

P. Giraud
Paris Descartes University (Paris V), Service d'Oncologie Radiothérapie, Hopital Europeen Georges Pompidou, Paris, France

B. Doyle et al. (eds.), *Computational Biomechanics for Medicine*,
DOI 10.1007/978-3-319-15503-6_10

Internal organ motion estimation methods may be divided into two groups: image-based, and biomechanical models. The first methods consist of deformable image registration (DIR) techniques that estimate motion vector fields by directly extracting them from 4D image sequences. A detailed overview of DIR-based methods may be found in [1]. Image-based methods calculate the displacement fields without explicitly taking the information related to the breathing physiology and physical properties of organs into account. In contrast, biomechanical models attempt to describe respiratory-induced organ motion through a mathematical formulation based on physics. More precisely, biomechanical models describe the physiological process related to organ motion using continuum mechanics, which explains why image-based models require biomechanical modeling.

Concerning lung cancer, respiratory tumor motion tracking is very challenging in external beam radiation therapy of the lung, including 3D conformal radiotherapy (3D-CRT) [2], Intensity Modulated Radio Therapy [3], stereotactic radiation therapy (SRT) [4], and proton beam therapy (PBT) [5]. Current techniques based on imaging, such as Cone-Beam or DIR, attempt to predict the position of lung tumors [6]. Unfortunately, these methods assume a reproducible motion of the respiratory system.

However, the respiratory motion is complex and its prediction is not a simple task, especially since breathing is controlled by the independent action of two muscles: the diaphragm and the intercostal muscles of the ribcage. The former is composed of a peripheral part (muscular fiber) and a central part (tendon). The latter are attached to the ribs, including the complete thorax with musculoskeletal structure. Consequently, the respiratory motion is non-reproducible [6] and image-based techniques are liable to give unsatisfactory results. The diaphragm is the main muscle for respiration, and studying its shape and motion is also important to detect respiratory diseases and to study the induced motion of other organs for radiotherapy or laparoscopic surgery.

Various models have been proposed for diaphragm modeling by the computer graphics community for real-time applications [7, 8]. The main drawback of these models is the lack of precision due to the difficulty of the integration of the biomechanical parameters into them. Other models have been implemented to demonstrate the concept using the finite element method (FEM) [9–12]. The main advantages of FEMs are accuracy and realism. Furthermore, the FEM model allows the direct integration of experimentally obtained biomechanical tissue parameters.

Unfortunately, the behavior of the diaphragm using FEM models is not confronted with clinical data, and the authors don't include the influence of the thorax and ribs kinematics on the diaphragm motion.

In this chapter, we propose a biomechanical model of the respiratory system and study the impact of nonlinearities and the role of rib kinematics on the amplitude of the diaphragm motion. This model includes the physiological information of the diaphragm, including the tendon and muscles, and the complete thorax with musculoskeletal structure (ribs, thoracic vertebra, costal cartilage margin, body of sternum) extracted directly from 4D CT scan images coupled with the kinematics modeling of the ribcage based on the finite helical axis method (FHAM). In order

to study the appropriate biomechanic model of the diaphragm, we propose two nonlinear hyperelastic models: Saint-Venant Kirchhoff (large displacement) and Mooney–Rivlin (large displacement and large strain).

2 Materials and Methods

2.1 Anatomy and Physiology of the Respiratory System

Breathing is an active and complex process where the mechanics of the respiratory motion is controlled by two muscle groups: the diaphragm and the intercostal muscles attached to the ribs. The diaphragm is a dome-shaped musculofibrous membrane which separates the thorax from the abdominal cavity. It presents the shape of a dome concave toward the abdomen (Fig. 1). It is composed of a peripheral part (muscular fiber) and a central part (tendon). The tendon is the upper part of the diaphragm, in contact with the lungs and is closer to the front than to the back of the thorax, so that the posterior muscular fibers are longer. The peripheral part, which consists of muscles, is linked to the lower thoracic cavity perimeter and has three major insertions: lumbar, sternum, and ribs.

The diaphragm moves down during the inhalation, creating negative pressure around the thoracic cavity and decreasing pressure on abdominal organs. As it moves up during exhalation, the pressure increases on the lungs and on abdominal organs (Fig. 1). Lungs are linked to the diaphragm and to the ribs through the pleura. The pleura consists of two sheets (visceral and parietal). The visceral pleura is attached to the lungs and the parietal pleura is attached to the diaphragm and to the chest wall. Between the two sheets, an incompressible fluid allows lungs to slide while they follow diaphragm and ribs motion.

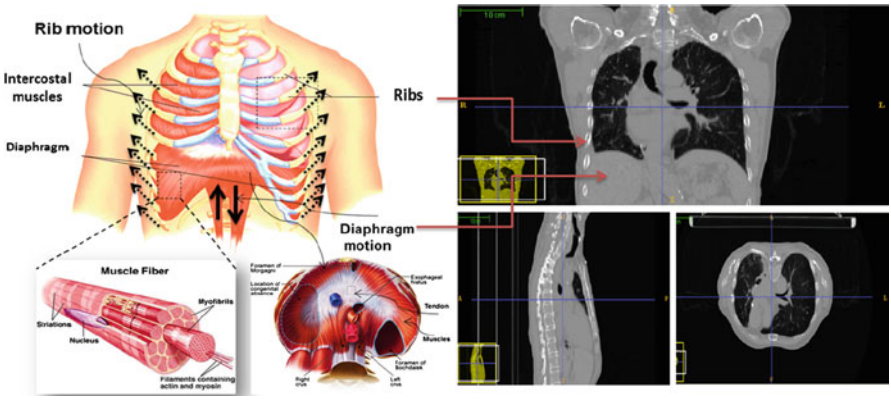

Fig. 1 Respiratory mechanics: the role of the diaphragm and thorax in breathing

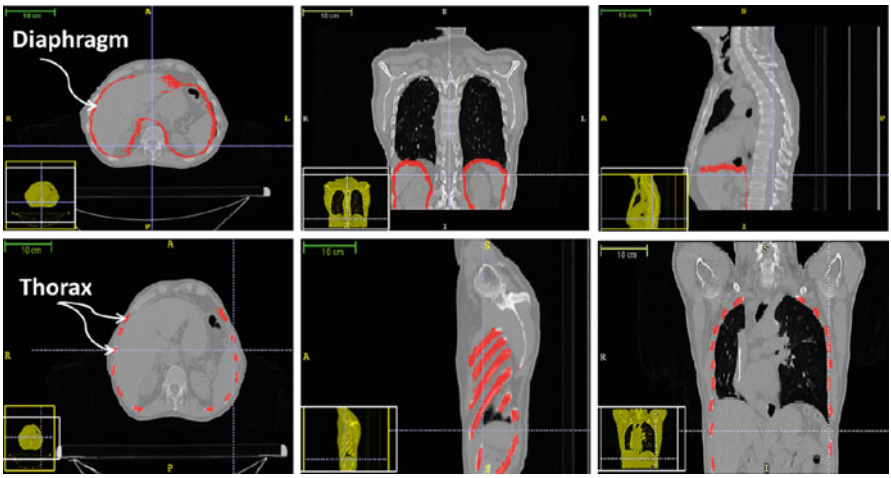

Fig. 2 Automatic and semi-automatic segmentation of the internal organs of the respiratory system: ribs, human diaphragm, and lungs

2.2 3D Automatic and Semi-Automatic Segmentation

We have chosen CT scan data covering the whole thorax of a patient. The 4D CT set is issued from a pre-treatment procedure of a lung cancer patient. From the 4D set, we choose two 3D sets of images that correspond to the maximum and to the minimum of the respiratory cycle. The diaphragm is a thin tissue, with thickness between 2 and 5 mm. In Fig. 2, the diaphragm was segmented semi-automatically using the snake evolution methodology available in the ITK-SNAP library. The diaphragm muscles and tendon may not be identified separately on CT images. According to [13], the mean central tendon surface area is 143 cm^2. This area does not vary to a large extent from one person to another.

An automatic segmentation algorithm of the thorax with all musculoskeletal structure was developed in our team. We have applied a threshold value to the images and used morphological operators in order to fill holes and link separated regions that correspond to the same rib. Then, a surface mesh of the ribs and spine was generated using the marching tetrahedron algorithm.

2.3 Patient-Specific Anatomical 3D Model

Figure 3 presents a global methodology pipeline in order to generate biomechanical patient-specific anatomical 3D models of the respiratory system from medical images. The main motivations of the proposed methodology pipeline based on CAD-modeling come from the difficulties in applying the finite element (FE)

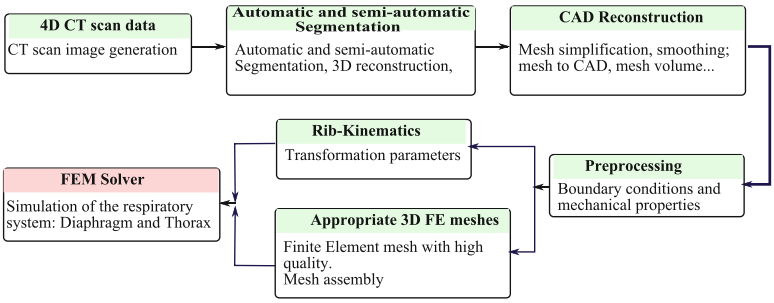

Fig. 3 Global pipeline in order to generate patient-specific anatomical 3D models of the respiratory system from medical images (CT scan data) to finite element simulation

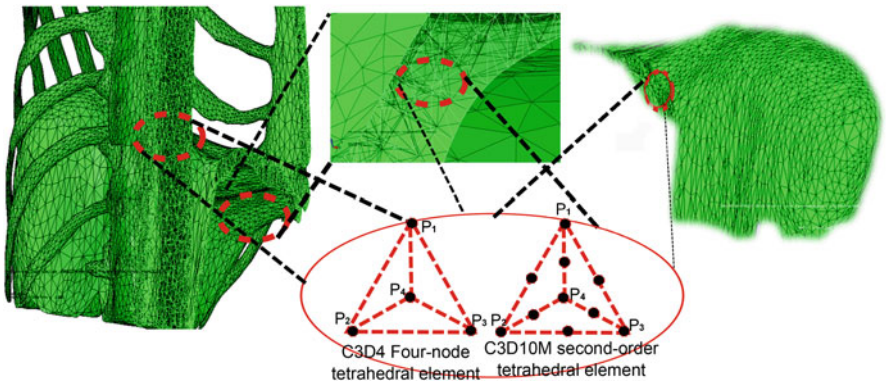

Fig. 4 Representation of the 3D diaphragm and thorax meshes

method in biomechanical analysis due to the complexity associated with creating subject-specific anatomical models. For this reason we have adopted the following computational procedure:

1. 4D CT scan images; acquisition and generation of the 4D CT images of the whole respiratory system,
2. 3D automatic and semi-automatic segmentation, 3D reconstruction of the respiratory system (different organs),
3. 3D CAD model reconstruction and then 3D mesh generation from CT images (decimation, smoothing, etc.) in order to generate the appropriate mesh elements adapted to finite element simulation, (Fig. 4)
4. Boundary conditions between the various organs of the respiratory system (lungs, diaphragm, thorax, etc.) based on anatomical and physiological properties,
5. Finite element analysis of the respiratory system based on appropriate behavior laws for each organ (linear elastic, nonlinear hyperplastic, homogenous or heterogenous, etc.).

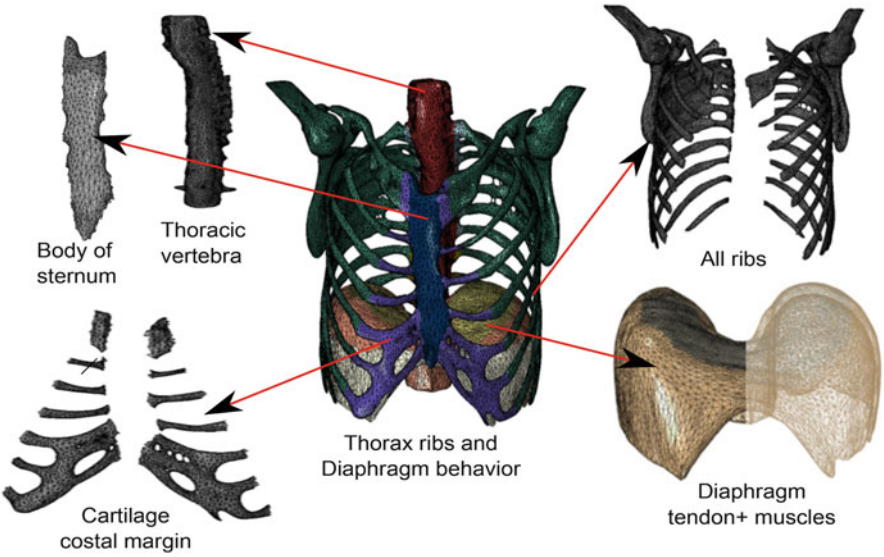

Fig. 5 Different parts of the human diaphragm and thorax including: tendon and muscles tissues, ribs, thoracic vertebra, costal cartilage margin, body of sternum

2.4 Generation of the Finite Element Mesh

Mesh generation is a critical and important step in the finite element analysis process. The mesh affects the accuracy, convergence, and speed of the computational process: a more precise and efficient finite element mesh will result in a more accurate and faster solution. Suitable geometry simplification plays a major role in obtaining a proper finite element model for a specific application. Simplifications usually involve elimination of less important details that unnecessarily increase the meshing complexity. In this order, it is necessary to obtain a high quality 3D geometrical representation of anatomical shapes and generate adapted FEM meshes. For the geometries, we have used NURBS surface models, resulting in non-intersecting and smooth organ representations (Fig. 5).

2.5 Respiratory Biomechanics

Finite element simulations are performed by using Abaqus.[1] In this study, we chose two simple hyperelastic models: Saint-Venant Kirchhoff and Mooney–Rivlin.

[1]The FE code Abaqus is developed by SIMULIA.

For an isotropic elastic or hyperelastic material, the elastic energy, noted W, may be written as:

$$W(\mathbf{E}) = \frac{\lambda}{2}(tr\,\mathbf{E})^2 + \mu\,(tr\,\mathbf{E}^2), \tag{1}$$

where $\mathbf{E}$ is the Green–Lagrange strain tensor, λ and μ are the Lame coefficients. As the strain energy function W is quadratic in terms of strain invariants, we obtain a linear relation between the second Piola–Kirchhoff stress tensor and the Green–Lagrange strain tensor given by:

$$\mathbf{S} = \lambda\,(tr\,\mathbf{E})\,\mathbf{I} + 2\,\mu\,\mathbf{E}. \tag{2}$$

The strain energy of the second hyperelastic Mooney–Rivlin model may be written as:

$$W(\mathbf{C}) = c_1\left(\bar{I}_1(\mathbf{C}) - 3\right) + c_2\left(\bar{I}_2(\mathbf{C}) - 3\right) + \frac{K}{2}\left(J(\mathbf{C}) - 1\right)^2, \tag{3}$$

where c_1, c_2 are material parameters and K is the Bulk modulus. The quantities $\bar{I}_1$ and $\bar{I}_2$ are the isochoric invariants of the Cauchy-deformation tensor $\mathbf{C}$: $\bar{I}_1(\mathbf{C}) = J(\mathbf{C})^{-2/3}\,I_1(\mathbf{C})$, $\bar{I}_2(\mathbf{C}) = J(\mathbf{C})^{-4/3}\,I_2(\mathbf{C})$ where $I_1(\mathbf{C}) = tr\mathbf{C}$, $I_2(\mathbf{C}) = \frac{1}{2}((tr\mathbf{C})^2 - tr\mathbf{C}^2)$ and J is the Jacobian: $J(\mathbf{C}) = det\,\mathbf{F}$.

2.6 Rib Cage and Intercostal Muscles: Rib Kinematics

The diaphragm biomechanics model is coupled with rib kinematics, with the aim to establish a thoracic model that may be monitored by external parameters. We have developed two different methods:

- a "direct" method allowing to compute the skin position from the ribs motion.
- an "inverse" method providing rib motion and consequently lung motion. It may be computed from the outer surface motion.

In this chapter, we focus on the first approach. The direct model describes the motion of the ribcage based on particular rigid transformations computed with the finite helical axis (FHA) method applied to each rib, which describes movement as a rotation and a translation along a single axis in the 3D space.

A state-of-the-art methodology to study human rib displacements using the FHAM is presented in our work [14, 15]. Since ribs may be considered as rigid bodies in comparison with other surrounding anatomical elements, each rib transformation parameter is computed automatically between the initial and final states of the respiratory motion (Fig. 6).

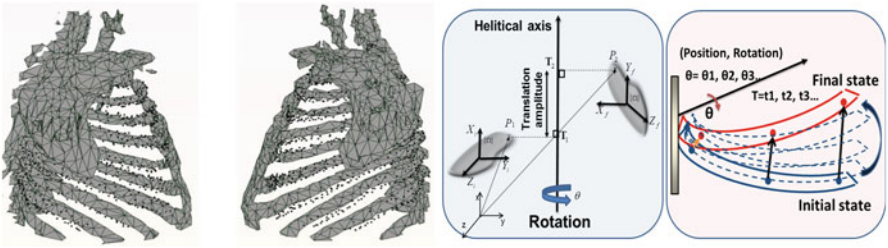

Fig. 6 Rib kinematics based on the finite helical axis method (FHAM). *Left figure*: two thorax sagittal—views gray mesh: thorax segmented on the CT scans at an intermediate state of breathing black dots: computed rib cage position by inverse kinematics. *Right figure*: finite helical axis method principle

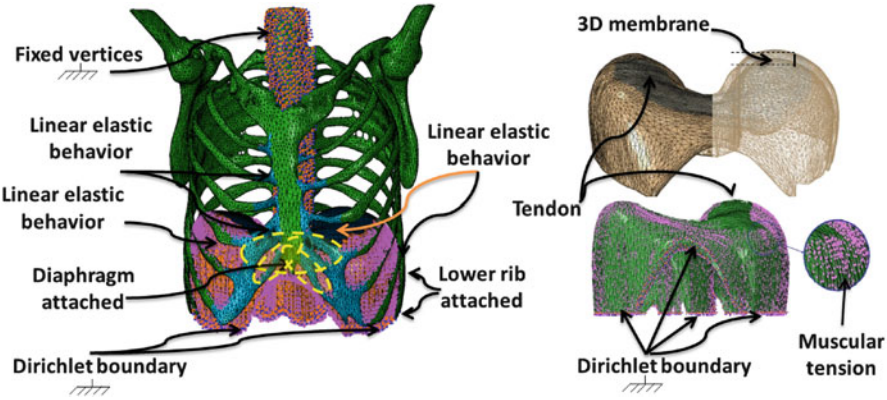

Fig. 7 The boundary conditions applied to the mesh nodes of the respiratory system: human diaphragm and thorax

2.7 Boundary Condition

The boundary conditions are inferred from the anatomy and identified by medical experts (see Fig. 7). The peripheral part, which consists of muscles, is linked to the lower thoracic cavity perimeter and has three major insertions: lumbar, sternum, and ribs. The lumbar part is fixed to the lumbar vertebrae by means of the crura. The sternal part is attached to the internal surface of the xyphoid process. The costal part is attached to the internal surfaces of the lower six costal cartilages or ribs. Dirichlet boundary conditions are applied in the lower part of the diaphragm. Two parameters are set to monitor diaphragm motion: the amplitude of muscles tension and ribs displacement. The pressure is applied on the muscular part of the

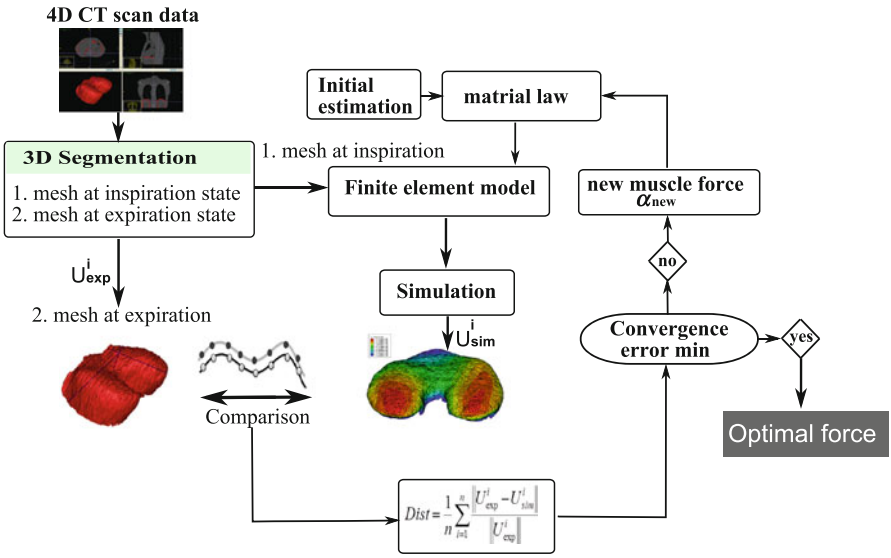

Fig. 8 Iterative process to minimize the displacement errors between simulation U_{sim} and initial mesh U_{exp}

diaphragm. The surface tension models generate forces that only depend on their amplitude applied to the surface. When applying the tension $\overrightarrow{t_s}$ on the diaphragm muscles, the resulting force may be written as:

$$\overrightarrow{f} = \int_S \overrightarrow{t_s}\, dS = \alpha \int_S \overrightarrow{\text{dir}_s}\, dS \tag{4}$$

with S, α et $\overrightarrow{\text{dir}_s}$, respectively, the mesh surface, the force amplitude, and direction. Figure 7 presents the radial direction of muscle forces, which corresponds anatomically to the direction of muscle fibers [12]. In order to determine the appropriate values of α, we have used an iterative process to minimize the errors between simulation and initial data (see Fig. 8).

2.8 *Quantitative and Qualitative Analysis of Biomechanical Simulations*

In order to demonstrate the validity of our biomechanical and kinematic model, a quantitative and qualitative analysis of simulations was conducted. We have compared the results of a simulated motion with the experimental data provided by the CT scan images, where the mechanical properties used in our finite element simulations are given in Table 1. First, it is important to check that the presence of

Table 1 Mechanical properties of the diaphragm and thorax, where E stands for the Young modulus, and ν for the Poisson coefficient

Tissues	Young modulus (MPa)	Poisson coefficient	References
Diaphragm muscle	5.32	0.33	Behr et al. (2006)
Diaphragm tendon	33	0.33	Behr et al. (2006)
Ribs	5,000	0.3	Yamada et al. [16]
Costal cartilage margin	49	0.4	[17, 18]
Body of sternum	11,500	0.3	Yamada et al. [16]
Thoracic vertebra	9,860	0.3	Yamada et al. [16]

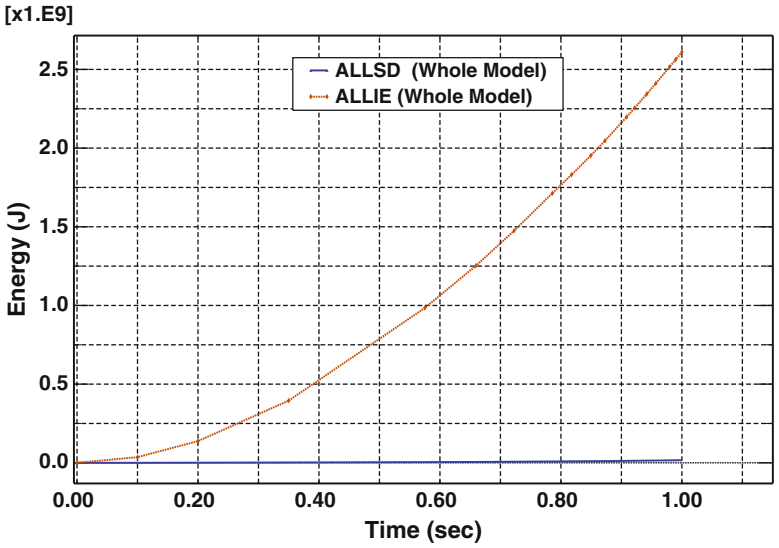

Fig. 9 Stabilization and internal energies: comparison between the energy dissipation due to stabilization (ALLSD) and the internal energy of the structure (ALLIE)

contact stabilization does not significantly alter the physics of the problem. One way to assess this requirement is to compare the energy dissipation due to stabilization (ALLSD) against the internal energy of the structure (ALLIE). Ideally the amount of stabilization energy should be a small fraction of the internal energy. The energies involved in the process have been plotted with respect to time. Figure 9 shows the variation of the stabilization and internal energies. It is clear that the dissipated stabilization energy is, indeed, small. Figure 10 shows the stress distribution, the total deformation, and the maximum displacement components of the thorax and diaphragm during normal inspiration between the initial state (inspiration) and the final state (expiration). The results show the maximum displacement of the diaphragm inside the thorax on the right-posterior (RP) and left-posterior (LP) sides.

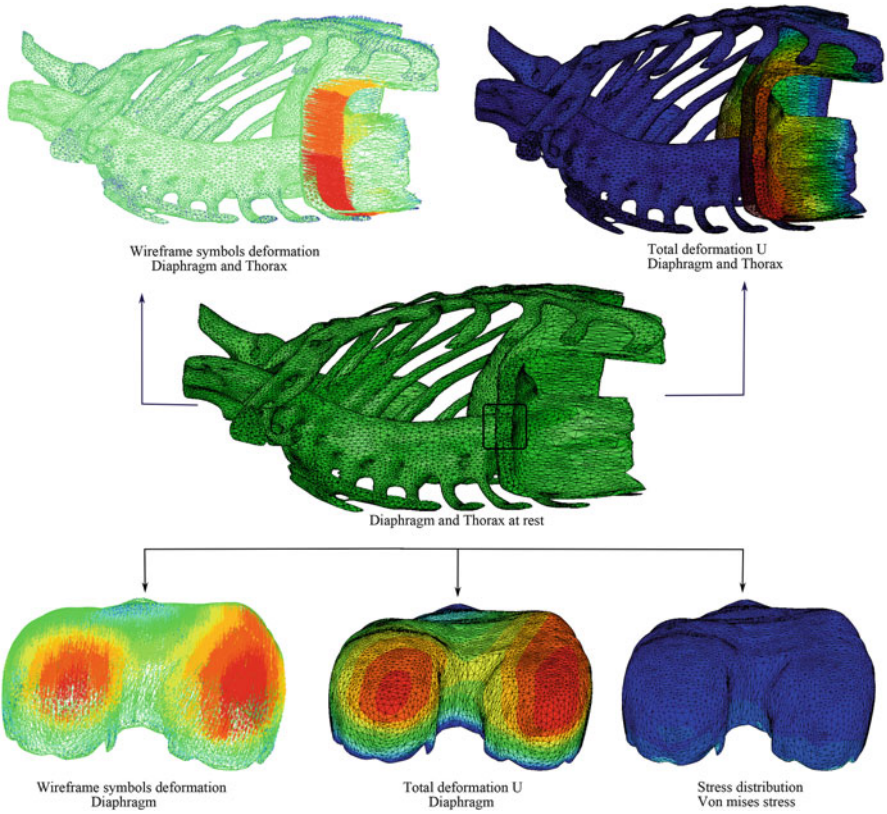

Fig. 10 Finite element simulation of the human respiratory system: stress distribution and the total deformation of the diaphragm including the thorax behavior

It is also possible to notice a slightly larger (RP) side motion than (LP) side motion, in concordance with the physiological anatomy.

Then, we were interested in evaluating the impact of the nonlinear behavior of the diaphragm. In this order, we have considered four cases: (1) $\mathbf{S_1}$, $\mathbf{S_2}$: The diaphragm was considered as compressible, heterogenous with a linear elastic behavior with large displacement (Saint-Venant Kirchhoff) considering or not the effect of ribs kinematics, (2) $\mathbf{S_3}$, $\mathbf{S_4}$: The diaphragm was considered as compressible, heterogenous with nonlinear hyperelastic behavior (Mooney–Rivlin) considering or not the effect of ribs kinematics.

Figure 11 presents a 3D distance map and distance between cross sections measured on the original mesh and the FEM simulation mesh of the diaphragm at inspiration.

Table 2 shows the errors in the region of interest; diaphragm/lungs contact, between the end inspiration (EI) and the end expiration (EE)—the average surface errors are 2.0 ± 2.2 mm. The simulation shows that the developed finite element

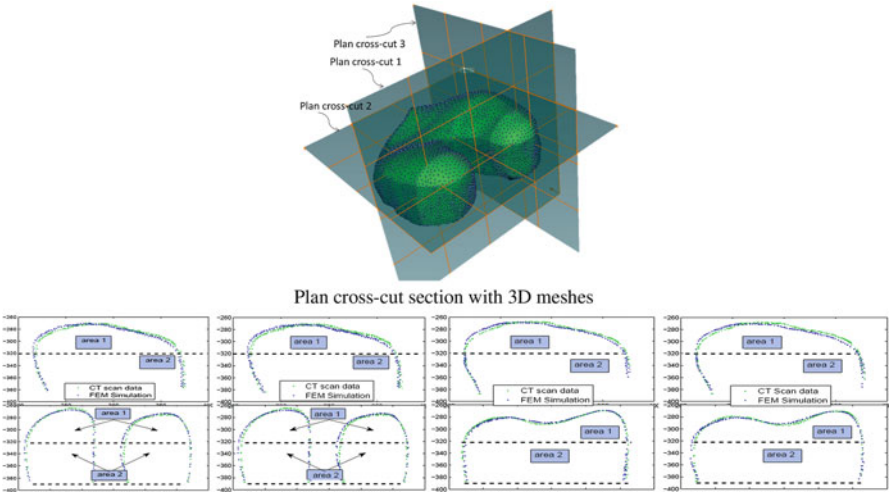

Fig. 11 3D distance map from the vertices of the diaphragm surface mesh at inspiration (simulation) to the reference mesh at inspiration. St-Venant Kirchhoff versus Mooney–Rivlin models. Showing the view from the cross sections, between the reference mesh at expiration and finite element simulation. Area 1 presents the interest region (the large amplitude of the deformation). Area 2 presents the peripheral contact between the diaphragm and ribcage (small displacement)

Table 2 Average error measurement ϵ and standard deviation (SD): applied to different scenarios

	Patients			
	St-Venant Kirchhoff		Mooney–Rivlin	
	$\mathbf{S_1}$ (without RK)	$\mathbf{S_2}$ (with RK)	$\mathbf{S_3}$ (without RK)	$\mathbf{S_4}$ (with RK)
Mean $\pm$ D (mm)	2.1 ± 2.3	2.0 ± 2.2	2.2 ± 2.3	1.9 ± 2.1

model is in a good agreement with the experimental data. However, these errors depend mainly on the quality of the 3D segmentation.

3 Discussion and Conclusion

From a biomechanical point of view, Saint-Venant Kirchhoff (linear elastic behavior with large displacement) gives as good results as Mooney–Rivlin (full nonlinear hyperelastic behavior). The linear elasticity is often used for the modeling of deformable materials, mainly because the equations remain quite simple and the computation time may be optimized. The physical behavior of soft tissue may be considered as linear elastic if its displacement and strain remain small (less than 10 % of the mesh size). To verify the hypothesis of small displacement and strain,

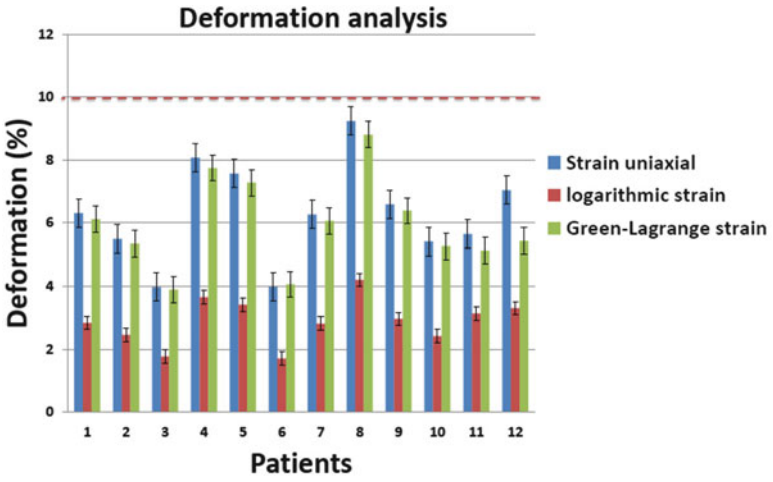

Fig. 12 Strain estimation: the uniaxial strain deformation ε_1, the logarithmic strain ε_2, and the Green-Lagrange strain ε_3

we compared the geometry of the diaphragm at the end of inspiration (EI) and at the end of expiration (EE).

We have calculated the uniaxial strain deformation measured by: $\varepsilon_1 = \frac{l-l_0}{l_0}$, where the large deformations may be measured by the logarithmic strain (also called natural strain) $\varepsilon_2 = ln\left(\frac{l}{l_0}\right)$. The Green-Lagrange strain is defined as: $\varepsilon_3 = \frac{1}{2}\left(\frac{l^2-l_0^2}{l_0^2}\right)$, where l_0 is the original length of the undeformed mesh and l is the length of the deformed mesh. All calculations have been tested on 12 patients. Figure 12 shows the average errors ϵ_i and standard deviation (SD) of the clinical data between EI and EF. These results confirm that the approach of small strains (with the large displacement) may be globally maintained in the modeling of the diaphragm (typically less than 10 % of the mesh size).

To conclude, we have investigated the challenging issues in biomechanical modeling of the human diaphragm and ribs kinematic. The first results of our simulations are quite realistic, compared to the experimental data. We can see that the proposed physically based FEM model coupled with the rib kinematics is capable of simulating correctly the respiratory system including the real boundary conditions of the diaphragm and thorax.

Currently, we are working on integrating the developed model in an interactive virtual physiological human model of the respiratory system based on GPU implementation, including the behavior of the lungs, pleura, heart, thorax, and soft tissues. Furthermore, these simulations will be monitored and correlated with external surrogates, using different imaging modalities. Also, the objective of this work is to produce a novel 4D computational patient-specific phantom that could be used

for diagnosis, beam therapy, dose distribution computation, or better registration of online imaging systems.

Acknowledgements This research was supported by the ENVISION project (co-funded by the European Commission under the FP7 Collaborative Projects Grant Agreement Nr. 241851FP7), by ETOILE's Research Program (PRRH/UCBL, under CPER 2007-13 funding) and by the LABEX PRIMES (ANR-11-LABX-0063), within the program "Investissements d'Avenir" (ANR-11-IDEX-0007) operated by the French National Research Agency (ANR).

References

1. Ehrhardt, J., Lorenz, C.: 4D modeling and estimation of respiratory motion for radiation therapy. Springer, Berlin (2013). ISBN 978-3-642-36441-9
2. Wu, K.L., Jiang, G.L., Liao, Y., Qian, H., Wang, L.J., Fu, X.L., Zhao, S.: Threedimensional conformal radiation therapy for non-small-cell lung cancer: a phase I/II dose escalation clinical trial. Int. J. Rad. Oncol. Biol. Phys. **57**(5), 1336–1344 (2003)
3. Sura, S., Gupta, V., Yorke, E., Jackson, A., Amols, H., Rosenzweig, K.E.: Intensity modulated radiation therapy (IMRT) for inoperable non-small cell lung cancer: the Memorial Sloan-Kettering Cancer Center (MSKCC) experience. Radiother. Oncol. **87**(1), 17–23 (2008)
4. Hiraoka, M., Matsuo, Y., Takayama, K.: Stereotactic body radiation therapy for lung cancer: achievements and perspectives. Jpn. J. Clin. Oncol. **40**(9), 846–854 (2010)
5. Nakayama, H., Sugahara, S., Tokita, M., Satoh, H., Tsuboi, K., Ishikawa, S., Tokuuye, K.: Proton beam therapy for patients with medically inoperable stage I non-small-cell lung cancer at the university of Tsukuba. Int. J. Radiat. Oncol. Biol. Phys. **78**(2), 467–471 (2010)
6. Shirato, H., et al.: Speed and amplitude of lung tumor motion precisely detected in four-dimensional setup and in real-time tumor-tracking radiotherapy. Int. J. Rad Onco Biol. Phys. **64**(4), 1229–1236 (2006)
7. Promayon, E., Baconnier, P.: A 3D discrete model of the diaphragm and human trunk. In: ESAIM: Proceedings, pp. 66–77 (2008)
8. Villard, P.F., Bourne, W., Bello, F.: Interactive simulation of diaphragm motion through muscle and rib kinematics. In: Recent Advances in the 3D Physiological Human, pp. 91–103. Springer, London (2009)
9. Hostettler, A., George, D., Rémond, Y., Nicolau, S.A., Soler, L., Marescaux, J.: Bulk modulus and volume variation measurement of the liver and the kidneys in vivo using abdominal kinetics during free breathing. Comput. Methods Programs Biomed. **100**(2), 149–157 (2010)
10. Fuerst, B., et al.: A personalized biomechanical model for respiratory motion prediction. MICCAI **15**(3), 566–573 (2012)
11. Behr, M., Pérès, J., Llari, M., Godio, Y., Jammes, Y., Brunet, C.: A three-dimensional human trunk model for the analysis of respiratory mechanics. J. Biomech. Eng. **132**, 014501-1-014501-4 (2010)
12. Pato, M., et al.: Finite element studies of the mechanical behaviour of the diaphragm in normal and pathological cases. CMBBE **14**(6), 505–513 (2011)
13. Cluzel, P., Similovsky, T., Lefebvre, C., Zelter, M., Derenne, J.P., Grenier, P.: Diaphragm and chest wall: assessment of the inspiratory pump with MR imaging - preliminary observations. Radiology **215**, 574–583 (2000)

14. Didier, A.L., Villard, P.F., Saade, J., Moreau, J.M., Beuve, M., Shariat, B.: A chest wall model based on rib kinematics. In: IEEE ICV, pp. 159–164 (2009)
15. Ladjal, H., Shariat, B., Azencot, J., Beuve, M.: Appropriate biomechanics and kinematics modeling of the respiratory system: human diaphragm and thorax. In: IEEE IROS (2013)
16. Kimpara, H., et al.: Development of a three-dimensional finite element chest model for the 5(th) percentile female. Stapp Car Crash J. **49**, 251–269 (2005)
17. Abe, H., Hayashi, K., Sato, M. (eds.): Data Book on Mechanical Properties of Living Cells, Tissues, and Organs. Springer (1996)
18. Yamada, H.: In: Evean, F.G. (ed.) Strength of Biological Materials. The Williams & Wilkins Company, Baltimore (1970)

A Collective Approach for Reconstructing 3D Fiber Arrangements in Virtual Musculoskeletal Soft Tissue Models

Hon Fai Choi, Andra Chincisan, and Nadia Magnenat-Thalmann

1 Introduction

The mechanical properties of musculoskeletal soft tissue structures are often altered in orthopedic interventions, either intentionally or inadvertently. Therefore, evaluation of biomechanical consequences as part of the preoperative planning can enhance the surgical outcome, but requires an adequate quantification of soft tissue excursions. Medical imaging is not always favorable for this purpose because of limitations in acquisition speed and field of view or the patient's mobility. Virtual simulations provide an alternative means to estimate the mechanical conditions in soft tissue structures that are critical for the patient's movement, which can be quantified in three-dimensional (3D) anatomical models using the finite element (FE) method [1, 2]. In the musculoskeletal system, soft tissues such as muscles, tendons, ligaments, and menisci are characterized by a hierarchical organization in fiber bundles or fascicles running between attachments. The orientations of these bundles are important determinants of mechanical capacities and need to be represented in the tissue model to simulate an adequate mechanical response.

Quantitative measurement of the complete internal fibrous architecture is currently still challenging. Cadaveric dissections are often performed, but require specialized expertise and are work intensive. Consequently, cadaveric measurements are often sparsely sampled, especially in large skeletal muscles, while detailed dissection studies have been reported for only a few selected muscles [3].

H.F. Choi (✉) • A. Chincisan
MIRALab, University of Geneva, Geneva, Switzerland
e-mail: choi@miralab.ch

N. Magnenat-Thalmann
MIRALab, University of Geneva, Geneva, Switzerland

IMI, Nanyang Technological University, Singapore, Singapore

B. Doyle et al. (eds.), *Computational Biomechanics for Medicine*,
DOI 10.1007/978-3-319-15503-6_11

To obtain in vivo measurements, ultrasound imaging is an accessible modality with a fast acquisition time, but has a limited scan depth and currently only allows for the quantification of projected fiber angles in the 2D imaging plane which is sensitive to the probe orientation [4]. Alternatively, diffusion tensor magnetic resonance imaging (DT-MRI) can visualize fiber orientations in any anatomical region of the body, but technical challenges such as low signal-to-noise ratio are still limiting a wide application for musculoskeletal measurements [5]. As such, DT-MRI data are generally noisy and require post-processing with user-defined parameters and exclusion conditions to remove erroneous fiber tracts [6]. Currently, most experimental characterizations of 3D fiber arrangements have been focused on skeletal muscles [3, 6]. Fiber bundle architectures in tendon, ligaments, and menisci have been predominantly investigated in cadaveric or ultrasound studies, with average quantitative measurements reported in a few studies [7, 8]. Alternatively, microstructural characterization of 3D fiber distributions from confocal microscopy images has been demonstrated in the meniscus [9, 10], showing potential for non-destructive in situ mechanical modeling in arthroscopy applications.

Because in vivo 3D volumetric measurements are not yet fully standardized, computational approaches provide an alternative to construct computational representations of musculoskeletal fiber arrangements in 3D anatomical models that are physiologically plausible for biomechanical simulations. To this end, several methods have been proposed aiming at different tissue types and with varying levels of approximations. Uniform orientation along a single axis of the global coordinate system has been proposed [11, 12], while other studies define fiber orientations implicitly according to element directions in structured hexahedral mesh models [13]. An approximation based on neuromuscular line-element models has been described for anatomical muscle models [14], while a centerline method combined with diffusion interpolation was suggested for knee ligament models [15]. To account for the diversity of muscle morphologies, other studies have proposed spline-based interpolation based on data from cadaveric studies [16], volumetric warping of fascicle map templates onto 3D anatomical models [1] or generation of a Laplacian vector field representation based on the characteristic properties of the fascicle arrangements [17].

The diversity of methods offers different possibilities to represent soft tissue fiber arrangements in anatomical simulation models. However, several of these approaches involve geometrical simplifications or assumptions or depend on a structured mesh topology, which is difficult to generalize for the variability in complexity of musculoskeletal anatomy. Application in computer assisted systems would therefore require differentiation between use cases to select methods, resulting in an implementation that is impractical to manage. Because the typical physical properties as displayed by the fascicle organization are similar among the musculoskeletal soft tissues, the Laplacian approach can potentially serve as a collective methodological basis. Therefore, the aim of this study is to investigate the feasibility of the Laplacian method to define fiber bundle orientations in 3D virtual models for the various types of musculoskeletal soft tissue structures. Hereto, the utility for the common penniform muscle type is further explored by

modifying the procedure as proposed in [17] to facilitate the model construction. In addition, the implementation of the Laplacian method is tested in example models of connective soft tissue structures that are important in orthopedic interventions, i.e. ligaments and knee menisci. The application for concrete use cases is further evaluated in biomechanical simulations.

2 Methods

The general workflow of the Laplacian approach to generate fiber arrangements in 3D anatomical models has been adopted from [17] and is illustrated in Fig. 1. The theoretical foundation of the method has been outlined for skeletal muscles, but can be translated to most other musculoskeletal fibrous tissues that share a similar bundled organization. In summary, the conceived physical properties of the bundled fiber arrangements are that the bundles are parallel aligned and run continuously between the attachment areas. These properties can be mathematically represented by a rotation and divergence free Laplacian vector field which is obtained by solving the linear Laplace equation:

$$\Delta\phi = 0 \tag{1}$$

To solve the differential Eq. (1), Neumann boundary conditions are applied on the surfaces which describe the values of the potential gradient or flux, $\partial\phi/\partial\mathbf{n}$.

Because termination only occurs at the attachment areas, a zero gradient is defined on the bulk surface. A uniform flux can be applied at the attachment surfaces such that the mass equation is respected, which allows for the generation of physically plausible fiber directions as demonstrated in skeletal muscle models in [17]. The Laplace equation can be solved using the finite element (FE) or finite volume (FV) method, but the calculation of the flux values across element faces in the FV method allows for a robust element-by-element tracing of the fascicle trajectories between the attachments as described in [17].

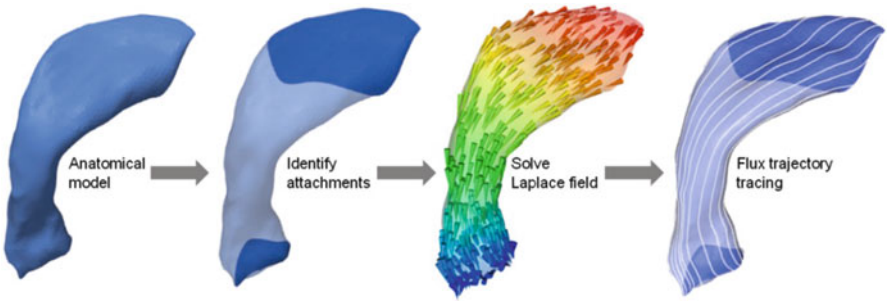

Fig. 1 Overview of the workflow to generate a computational vector field representation of fiber arrangements in 3D anatomical models using the Laplacian approach

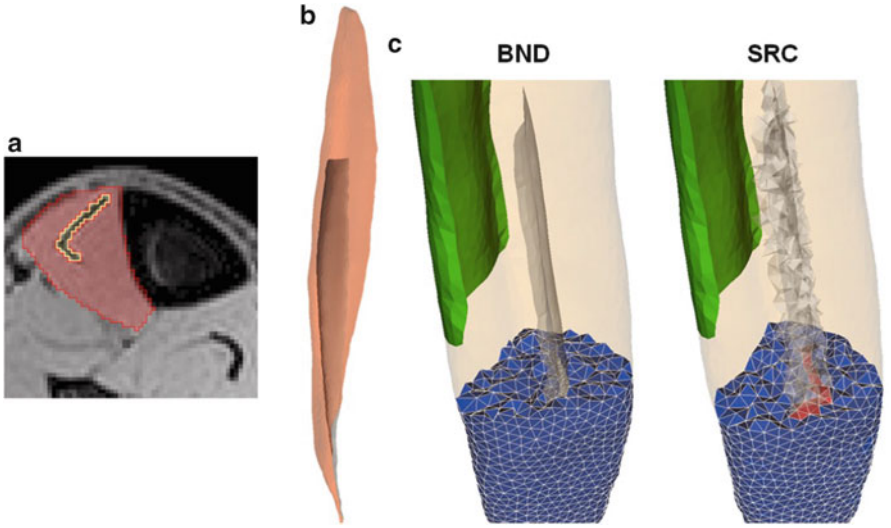

Fig. 2 Comparison of the internal tendon representation of the tibialis anterior muscle (lower leg) using surface reconstruction (BND) and source term (SRC) approach: (**a**) MRI segmentation, (**b**) 3D surface reconstruction, (**c**) clipped volumetric meshes to illustrate the localization of the tendon. The proximal attachment is indicated in green

The workflow summarized in Fig. 1 provides a robust basis to computationally generate musculoskeletal fiber arrangements. However, many skeletal muscles are characterized by an architecture in which oblique fibers originate from narrow internal aponeurosis tendons embedded in the muscle bulk volume as illustrated in Fig. 2. Because the tendon inserts at a very shallow angle, an awkward geometry is obtained, generating topological conditions that make it difficult to generate a 3D volumetric mesh that is adequate for FE simulations of large deformations. As an alternative, we propose to incorporate a source term s in Laplace's equation:

$$\Delta\phi = s \tag{2}$$

The tendon location is indicated by the source term, of which the distribution is assigned to elements in the volumetric mesh of the bulk muscle (Fig. 2). We have used algorithms from the VTK-library (www.vtk.org) to find the source elements as those intersecting with the segmented image voxels of the internal tendon. This approach allows to approximate the tendon location inside the muscle volume without having to include it in the surface reconstruction as attachment area.

Some musculoskeletal soft tissues are characterized by multiple fiber families. The collagen fibers in the knee menisci are mainly organized in circumferential bundles, with sparse bundles in the radial directions [18]. Therefore, meniscus tissue is often modeled as an orthotropic material [13], which requires the definition of three perpendicular directions that reflects the multiple fiber anisotropy. The definition of

the circumferential $\mathbf{f}_c$ and radial $\mathbf{f}_r$ fiber orientations can be obtained by applying the Laplacian method with attachments at respectively the horns of the menisci and at the internal and external surfaces as illustrated in Fig. 6. For the radial fibers, a uniform value for the potential ϕ is applied as boundary condition to better reflect the radial orientations. Because the generated circumferential and radial fiber directions are not necessarily perpendicular, a similar approach as in the OpenKnee model [13] can be applied to define the local coordinate system $\mathbf{e}_i$ for the orthotropic material symmetry:

$$\mathbf{e}_1 = \mathbf{f}_c,\ \mathbf{e}_2 = \mathbf{e}_3 \times \mathbf{e}_1,\ \mathbf{e}_3 = \frac{\mathbf{f}_c \times \mathbf{f}_r}{\|\mathbf{f}_c \times \mathbf{f}_r\|} \tag{3}$$

3 Case Studies

The Laplacian method was evaluated in several examples of different musculoskeletal soft tissue organs. Three-dimensional anatomical models were constructed from segmentation of MRI images of which volumetric tetrahedral meshes were generated. The numerical implementations as described in [17] were used to construct the workflow, using Gmsh [19] as the mesh generator and the OpenFOAM package (www.OpenFOAM.com) as the FV solver.

The modified approach incorporating the source term (SRC) was tested in a model of the tibialis anterior muscle and contrasted against the original boundary attachment approach (BND). This muscle was selected to allow for a comparison with the results obtained in [17], which was shown to compare well with DT-MRI data presented in [20]. The tibialis anterior muscle is characterized by a long distal aponeurosis tendon that runs deep into the muscle, which divides the muscle into a deep and superficial compartment (Fig. 2). Following [17], the fascicle trajectory lengths of both compartments were analyzed, with trajectories traced from seed points defined on the deep and superficial side of the distal tendon (Fig. 3). The mean and standard deviation of the differences between both approaches expressed as percentage of the BND fascicle lengths were calculated as a measure of comparison. The overall agreement was further assessed by calculating the angle difference between the fiber orientation vectors as the inverse cosine of the dot product in the element centroids of the volume meshes generated in both approaches. To evaluate the impact on FE simulations of deformation, a comparison was also made between the fiber strains obtained for an isometric muscle contraction with 80 % muscle activation which was simulated in the FEBio software [21] with the muscle material model from [1] (Fig. 4).

To demonstrate the feasibility for other musculoskeletal soft tissues, anatomical models of knee ligaments and menisci were considered. As a comparison between methods, the Laplacian approach was applied to the OpenKnee models of these structures (simtk.org/home/openknee) in which the fiber orientations are defined implicitly by the directions in the hexahedral meshes. The OpenKnee models

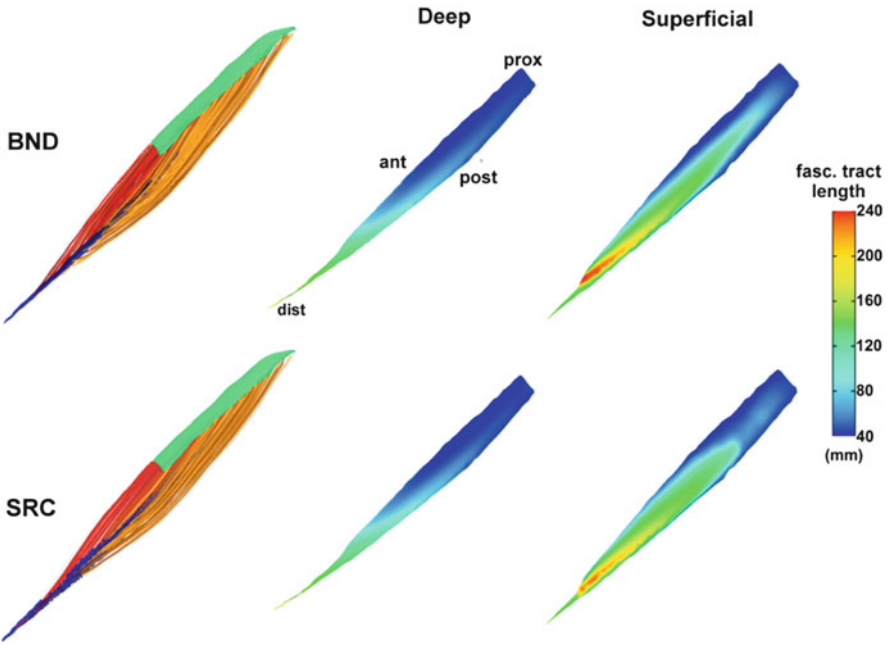

Fig. 3 Comparison of fascicle tract lengths between the BND and SRC approaches in a model of the tibialis anterior muscle. Samples of 3D fascicle trajectories for the deep (*red*) and superficial (*yellow*) compartments are shown in the *left column* (proximal and distal attachments shown in *green* and *blue* respectively). The fascicle lengths distributions mapped on the surfaces of the internal tendon for both compartments are shown on the *right*

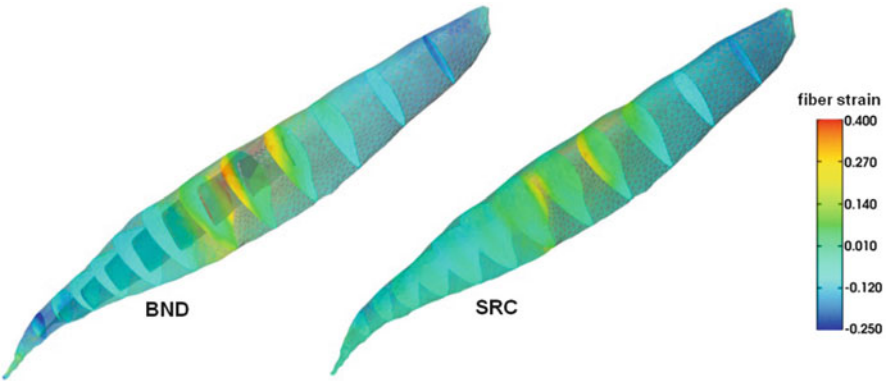

Fig. 4 Comparison of fiber strain between the BND and SRC approaches in a simulation of isometric contraction with 80 % activation level in the tibialis anterior muscle. The proximal attachment area is indicated by the wireframe

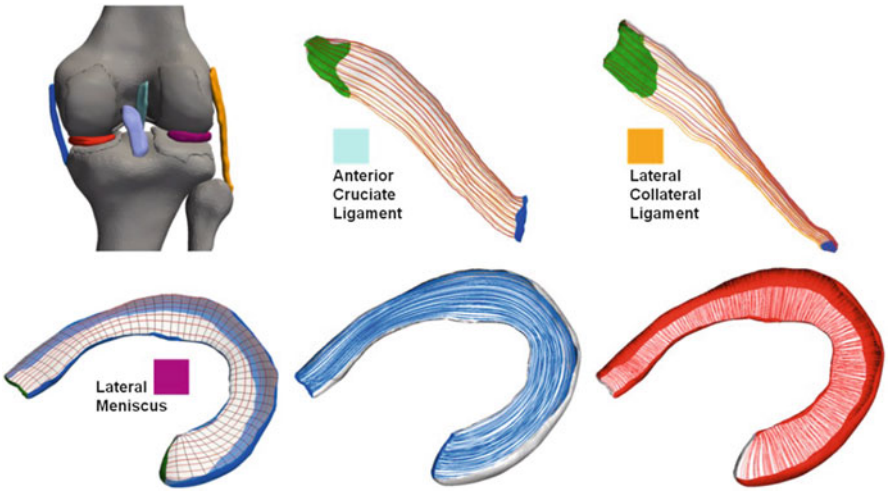

Fig. 5 Examples of Laplacian generated fiber traces (shown on the surface) in knee ligaments and menisci. The locations of the different structures are indicated by the color in the anatomical knee model shown in a posterior view in the *top left corner*. Generated circular (*blue*) and radial (*red*) fiber arrangements are shown for the lateral meniscus example in the *bottom row*

of ligaments and menisci were remeshed with tetrahedral elements to calculate the Laplacian fiber field. In each element center of the OpenKnee hexahedral meshes, the Laplacian vector calculated in the tetrahedral element that contained the hexahedral element center was compared with the hexahedral fiber direction. The comparison of fiber vectors was performed with the same measure as in the tibialis anterior muscle case. Additionally, the Laplacian method was further evaluated in a second in-house developed anatomical knee model (Fig. 5). FE simulations of anterior–posterior displacement were performed in FEBio for two cases: (1) with ligament fibers and (2) without ligament fibers and using material parameters averaged between the fiber and transverse directions. The force-displacement relation or knee laxity was calculated and compared with experimental data (Fig. 6). Secondly, a rotational flexion of 45° around an axis fitted through the femur condyles [22] was also simulated in FEBio. Length changes of fascicle trajectories in the ligaments were calculated and compared with experimental studies presented in the literature (Fig. 6). For these simulations, the transverse isotropic Mooney–Rivlin was used as material model for the ligaments, following [13].

4 Results

The distributions of the calculated fascicle trajectory lengths for the deep and superficial compartments in the tibialis anterior muscle are presented in Fig. 3. The results obtained for both the boundary attachment (BND) and source term

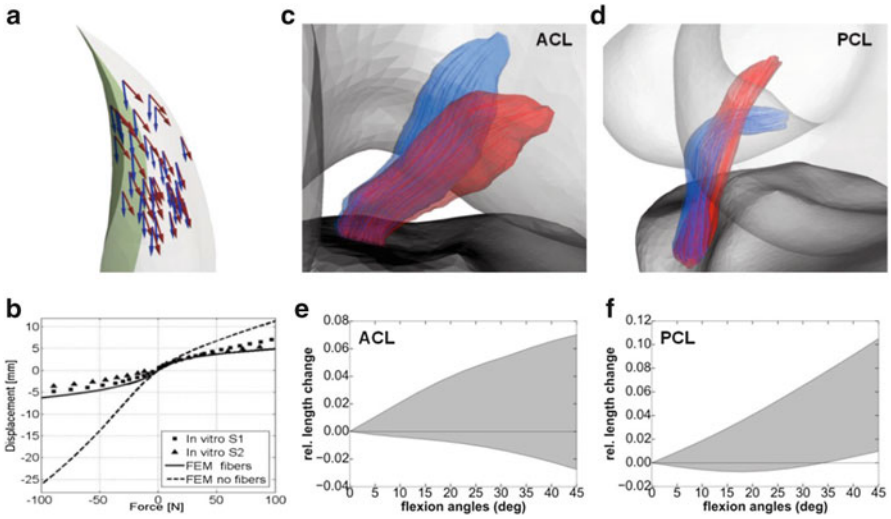

Fig. 6 Illustration of comparisons in knee ligament models. (**a**) Difference between Laplacian (*red*) and hexahedral (*blue*) fiber vectors near the femoral attachment in the OpenKnee model of the anterior cruciate ligament (*ACL*). (**b**) Comparison between simulated (FEM) and measured (in vitro) force-displacement curves for an anterior–posterior knee laxity test. (**c**) and (**d**) show the initial (*blue*) and deformed (*red*) configuration with Laplacian fascicle traces for the cruciate ligaments in the simulation of 45° knee flexion. The associated ranges of relative length changes in the fascicle traces are shown in (**e**) and (**f**)

(SRC) approaches display similar distributions. The mean differences in fascicle trajectory lengths are 2.85 ± 2.33 % and 8.60 ± 9.92 % for the deep and superficial compartments respectively, which is within the intra-subject variability as obtained in [20]. The mean angle difference between fiber orientation vectors as calculated in the meshes generated in the SRC and BND approaches are $3.19 \pm 4.82°$ and $2.50 \pm 3.34°$ respectively. This shows that a high similarity is obtained for the fiber orientation vectors, although the similarity in fascicle lengths is lower due to the cumulative effect of the tracing procedure. The range in fascicle lengths was between 40 and 240 mm, which is comparable with the range obtained in [17] (25–255 mm). The distributions as shown in Fig. 2 also display the same general characteristics as demonstrated in [17, 20], with fascicle lengths decreasing from the distal towards the proximal end. Some differences in the local gradients of the distributions can be observed, which can be explained by regional differences in the tendon geometry, especially at the distal end. As shown in Fig. 4, the fiber strains obtained in the FE simulation of isometric contraction show similar distributions between the BND and SRC approaches. The largest differences occur in the region around the proximal end of the internal distal tendon where the fiber strains are lower for the SRC approach compared to the BND approach (about 10 %). The simulation of isometric muscle contraction yielded a mean difference in fiber strain of 0.011 ± 0.065 and -0.014 ± 0.067 in the SRC and BND meshes respectively.

Table 1 Mean angle differences in degrees between Laplacian and hexahedral mesh generated fiber orientations in the OpenKnee models of anterior (*ACL*) and posterior (*PCL*) cruciate ligaments, lateral (*LCL*) and medial (*MCL*) collateral ligaments and lateral (*LM*) and medial (*MM*) menisci

ACL	PCL	LCL	MCL
7.21 ± 8.50	3.89 ± 2.74	3.58 ± 4.11	4.62 ± 3.67
LM		MM	
$\mathbf{e}_1$	$\mathbf{e}_2$	$\mathbf{e}_1$	$\mathbf{e}_2$
3.70 ± 2.72	3.08 ± 2.70	2.49 ± 1.85	3.35 ± 2.63

The fascicle trajectories, for example, of ligaments and menisci in the in-house developed 3D anatomical knee model are illustrated in Fig. 5. The angle differences between the fiber orientation vectors obtained with the Laplacian method and with the hexahedral mesh directions in the OpenKnee models are listed in Table 1. A close agreement is found in all cases, except for the anterior cruciate ligament (ACL). In this case, a larger difference was obtained in the region adjacent to the femoral attachment, where the orientation vectors converged towards the attachment in the Laplacian approach while they were aligned tangentially in the OpenKnee model as shown in Fig. 6a.

The anterior–posterior knee laxity or force-displacement relations obtained in the FE simulations with the in-house knee model are shown in Fig. 6b. The simulations performed with and without fibers show a noticeable difference, whereby the simulation with fibers displayed a good agreement with two experimental data sets. The deformations of the anterior (ACL) and posterior (PCL) cruciate ligaments obtained in the simulation of knee flexion are shown in Fig. 6c, d, illustrating the robust flux tracing of the fascicle paths. This allows for the calculation of the resulting length changes in the traced fascicle paths of which the ranges are shown in Fig. 6e, f. Comparison for the ACL shows a similar range in fiber stretching as reported in [8] (0.05), but the range in fiber slacking seems to be underestimated (reported range of -0.2 in [8]). The range in fascicle length changes in the PCL is comparable with those reported in [7] (-0.05 to 0.15). To further illustrate the feasibility of the Laplacian method for other joint ligaments, examples of fascicle trajectories in hip ligaments are shown in Fig. 7.

5 Discussion and Conclusion

The goal of this study was to investigate whether a Laplacian vector field representation can provide a collective basis to reconstruct plausible 3D in vivo fiber architecture in virtual models of the assorted musculoskeletal soft tissue structures. To this end, the application in specific cases was evaluated. A modification of the

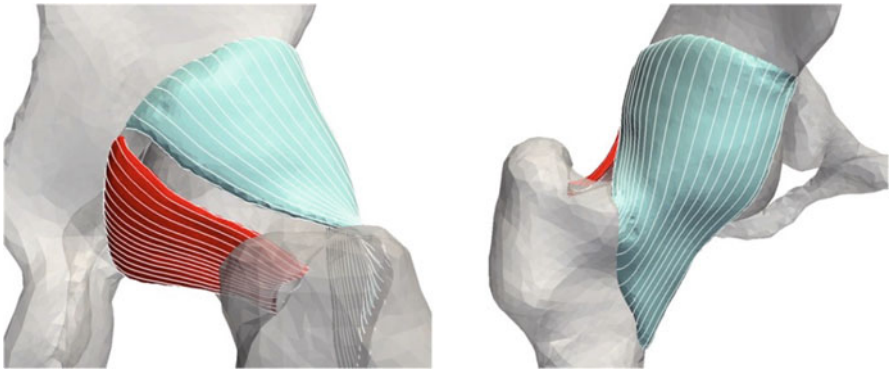

Fig. 7 Examples of Laplacian generated fiber traces (shown on the surface) in anatomical models of the iliofemoral (*blue*) and ischiofemoral (*red*) hip ligaments in anterolateral (*left*) and posterolateral (*right*) views

original strategy as proposed in [17] was formulated to facilitate the modeling procedure for difficult muscles with embedded tendons, which are prevalently present in major muscle groups, such as the tibialis anterior and rectus femoris. The results based on a model of the tibialis anterior muscle show a close similarity with those presented in [17] and good agreement with DT-MRI measurements reported in [20], while an FE simulation of a muscle contraction shows consistent results. The modified approach thus further fosters the feasibility of the Laplacian method for a wide range of muscle morphologies. The application in knee joint soft tissues demonstrated that fiber orientations are comparable with those in the OpenKnee models [13] that are based on a hexahedral mesh topology. However, the Laplacian approach can generate highly oblique fiber orientations at the attachment areas such as in the ACL (Fig. 6a) or in many skeletal muscles, while this is difficult to capture with a hexahedral mesh.

The comparison between experimental data and FE simulations of knee displacement and flexion further shows that physiological plausible mechanical behavior of the ligaments is also obtained. The robust flux tracing enables a quantification of fascicle length changes that are not typically reported in modeling studies of the knee. The results suggest that the slack range in the ACL was underestimated compared to reported experimental data, which is possibly related to the definition of the knee kinematics.

An adequate representation of fiber bundle orientations in models of musculoskeletal tissues is important to obtain simulations that are sufficiently realistic to give useful feedback for surgical planning and training. This is of particular importance in procedures that aim at altering mechanical function, such as tendon-transfer surgeries, or in complex arthroscopic interventions to reconstruct or replace damaged tissues. Virtual simulations are considered as valuable addition to traditional teaching methods, but require further developments to increase the realism in the soft tissue behavior [9], which are often modeled

as isotropic materials. The significant difference between ligament models with and without fiber orientations as obtained in the knee displacement simulation (Fig. 6b) illustrates the importance of incorporating fiber representations to model the anisotropy. Although several modeling studies have included a definition of fiber bundle orientations, this was done with a variety of methods with different levels of approximations in different soft tissues, which hardens comparison of simulation results and implementation for surgical applications. The results presented in this study support the feasibility of the Laplacian based approach to provide a common basis to model fiber bundle architecture in musculoskeletal virtual models. This allows for a comprehensive implementation, which benefits from fast solving strategies for the linear Laplace equation [23]. In addition, the same preprocessing steps as implemented for FE simulations of mechanical deformation (mesh construction and attachment indication) can be reused. Pathological regions can be defined by giving random or altered fiber orientations in the included mesh elements. In arthroscopic applications, a Laplacian modeling approach for the complete structure can be combined with in situ measurements using confocal microscopy [9, 10].

In future steps, the method needs to be further tested in applications and validated through comparison with detailed cadaveric or subject-specific measurements using DT-MRI, ultrasound or confocal microscopy, allowing for optimizing the boundary conditions at the attachment areas to match or smooth experimental data.

Acknowledgments This work has been funded by the EU FP7 Marie-Curie ITN project MultiScaleHuman under Grant number 289897. We thank the University Hospital of Geneva in Switzerland, for providing the medical images, and the biomechanics laboratory LBB-MHH of the medical school in Hanover, Germany, for the experimental data of knee displacement.

References

1. Blemker, S.S., Delp, S.L.: Three-dimensional representation of complex muscle architectures and geometries. Ann. Biomed. Eng. **33**(5), 661–673 (2005)
2. Weiss, J.A., Gardiner, J.C., Ellis, B.J., et al.: Three-dimensional finite element modeling of ligaments: technical aspects. Med. Eng. Phys. **27**(10), 845–861 (2005)
3. Kim, S.Y., Boynton, E.L., Ravichandiran, K., et al.: Three-dimensional study of the musculotendinous architecture of supraspinatus and its functional correlations. Clin. Anat. **20**, 648–655 (2007)
4. Klimstra, M., Dowling, J., Durkin, J.L., et al.: The effect of ultrasound probe orientation on muscle architecture measurement. J. Electromyogr. Kinesiol. **17**, 504–514 (2007)
5. Longwei, X.: Clinical application of diffusion tensor magnetic resonance imaging in skeletal muscle. Muscles Ligaments Tendons J. **3**(2), 58–59 (2012)
6. Kermarrec, E., Budzik, J.F., Khalil, C., et al.: In vivo diffusion tensor imaging and tractography of human thigh muscles in healthy subjects. AJR Am. J. Roentgenol. **195**, W352–W356 (2010)
7. Belvedere, C., Ensini, A., Feliciangeli, A., et al.: Geometrical changes of knee ligaments and patellar tendon during passive flexion. J. Biomech. **45**, 1886–1892 (2012)
8. Blankevoort, L., Huiskes, R., de Lange, A.: Recruitment of knee joint ligaments. J. Biomech. Eng. **113**, 94–103 (1991)

9. Taylor, Z.A., Kirk, T.B., Miller, K.: Confocal arthroscopy-based patient-specific constitutive models of cartilaginous tissues – I: development of a microstructural model. Comput. Meth. Biomech. Biomed. Eng. **10**(4), 307–316 (2007)
10. Taylor, Z.A., Kirk, T.B., Miller, K.: Confocal arthroscopy-based patient-specific constitutive models of cartilaginous tissues – II: prediction of reaction force history of meniscal cartilage specimens. Comput. Meth. Biomech. Biomed. Eng. **10**(5), 327–336 (2007)
11. Hirokawa, S., Tsuruno, R.: Three-dimensional deformation and stress distribution in an analytical/computational model of the anterior cruciate ligament. J. Biomech. **33**(9), 1069–1077 (2000)
12. Lu, Y.T., Zhu, H.X., Richmond, S., et al.: Modelling skeletal muscle fibre orientation arrangement. Comput. Methods Biomech. Biomed. Eng. **14**(12), 1079–1088 (2011)
13. Erdemir, A.: Open knee: a pathway to community driven modeling and simulation in joint biomechanics. In: Proceedings of the ASME/FDA 2013 1st Annual Frontiers in Medical Devices, Washington, DC, USA (2013)
14. Maurice, X., Sandholm, A., Pronost, N., et al.: A subject-specific software solution for the modeling and the visualization of muscles deformations. Vis. Comput. **25**(9), 835–842 (2009)
15. Heimann, T., Chung, F., Lamecker, H., et al.: Subject-specific ligament models: toward real-time simulation of the knee joint. In: Computational Biomechanics for Medicine IV, pp. 107–119. Springer, New York (2010)
16. Wu, F.T., Ng-Thow-Hing, V., Singh, K., et al.: Computational representation of the aponeuroses as NURBS surfaces in 3D musculoskeletal models. Comput. Methods Programs Biomed. **88**(2), 112–122 (2007)
17. Choi, H.F., Blemker, S.S.: Skeletal muscle fascicle arrangements can be reconstructed using a laplacian vector field simulation. PLoS One **8**(10), e77576 (2013)
18. Greis, P.E., Bardana, D.D., Holmstrom, M.C., et al.: Meniscal injury: I. basic science and evaluation. J. Am. Acad. Orthop. Sur. **10**(3), 168–176 (2002)
19. Geuzaine, C., Remacle, J.F.: Gmsh: a three-dimensional finite element mesh generator with built-in pre- and post-processing facilities. Int. J. Numer. Methods. Eng. **79**, 1309–1331 (2009)
20. Heemskerk, A.M., Sinha, T.K., Wilson, K.J., et al.: Quantitative assessment of DTI-based muscle fiber tracking and optimal tracking parameters. Magn. Reson. Med. **61**(2), 467–472 (2009)
21. Maas, S.A., Ellis, B.J., Atheshian, G.A., Weiss, J.A.: Febio: finite elements for biomechanics. J. Biomech. Eng. **134**(1), 011005 (2012)
22. Miranda, D.L., Rainbow, M.J., Leventhal, E.L., et al.: Automatic determination of anatomical coordinate systems for three-dimensional bone models of the isolated human knee. J. Biomech. **43**(8), 1623–1626 (2010)
23. McKenney, A., Greengard, L.: A fast Poisson solver for complex geometries. J. Comput. Phys. **118**, 348–355 (1995)
24. Wedmid, A., Llukani, E., Lee, D.I.: Future perspectives in robotic surgery. BJU Int. **108**(6b), 1028–1036 (2011)

Optimization of Acetabulum Reorientation in a Periacetabular Osteotomy by Finite Element Simulation: A Preliminary Study

L. Liu, T. Ecker, S. Schumann, K. Siebenrock, C. Chu, and G. Zheng

1 Introduction

Periacetabular osteotomy (PAO) is an effective approach for surgical treatment of hip dysplasia in young patients [12]. The aim of PAO is to increase acetabular coverage of the femoral head and to reduce contact pressures by realigning the hip joint [8]. It was reported that PAO planning approach is mainly based on two types of optimization strategies which are morphology-based and biomechanics-based optimization, respectively. In clinical routine, diagnosis and pre-operative planning of hip dysplasia is based on hip joint morphological parameters measured from a plain radiograph. However, these radiographic parameters for diagnosing hip dysplasia are unreliable. For instance, Clohisy et al. [7] evaluated the reliability of six hip specialists identifying important radiographic features of the hip on plain radiographs. They concluded that the standard radiographic parameters used to diagnose dysplasia are not reproducible [7]. Additionally, the same group, Carlisle et al. [6] further investigated the reliability of radiographic measurements of the hip by various musculoskeletal physicians. They found that while the measurements were reliable for a given observer, the measurements were less reliable across observers and were limited in determining a consistent radiographic diagnosis. A clear set of definitions and measurements need to be developed to enable more reliable diagnosis of early hip disease [7].

L. Liu • S. Schumann • C. Chu • G. Zheng (✉)
Institute for Surgical Technology and Biomechanics, University of Bern, 3014, Bern, Switzerland
e-mail: guoyan.zheng@istb.unibe.ch

T. Ecker • S. Siebenrock
Orthopaedic Department, Inselspital, University of Bern, 3010 Bern, Switzerland

B. Doyle et al. (eds.), *Computational Biomechanics for Medicine*,
DOI 10.1007/978-3-319-15503-6_12

The other type of planning strategy is based on biomechanics optimization. Zhao et al. [18] conducted a 3D finite element (FE) analysis of acetabular dysplasia. The effects of dysplasia and PAO were both investigated by analyzing the change of Von Mises stress in the cortical bone before and after surgery. They showed that the PAO may be beneficial. One limitation of this method lies in that the acetabular dysplastic models representing different levels of severity of dysplasia were generated by deforming the acetabular rim of a normal hip. Thus, it ignores the effect of the abnormal shape of the femoral head and acetabulum of the real dysplastic hip. In contrast, the computer-assisted biomechanical guidance system (BGS) introduced by Armand et al. [2] combines geometric and biomechanical feedback with intra-operative tracking to guide the surgeon through the PAO procedure. During the planning stage, the PAO planning computes contact pressures via discrete element analysis (DEA) in order to suggest a reorientation of the acetabulum that minimizes simultaneous peak contact pressure in sitting, standing, and walking positions [3]. Recently, Zou et al. [20] developed a 3D FE simulation of PAO and validated their method on five models generated from CT scans of dysplastic hips. The acetabulum of each model was rotated in 5° increments in the coronal plane from original lateral center edge (LCE) angle, and the relationship between contact area and pressure and Von Mises stress in the femoral and pelvic cartilage were investigated until the optimal position for the acetabulum following PAO was found.

Previously, we have developed a computer-assisted planning and navigation system for PAO [10], which allows for not only quantifying the 3D hip morphology with geometric parameters such as acetabular orientation (expressed as inclination and anteversion angles), LCE angle, and femoral head coverage for a computer-assisted diagnosis of hip dysplasia but also virtual PAO surgical planning and simulation. In this paper, based on this previously developed PAO planning and navigation system, we developed a patient-specific 3D FE model to investigate the optimal acetabulum reorientation after PAO. Our aim was to find the optimal orientation for the acetabulum after PAO.

2 Materials and Methods

2.1 Computer-Assisted Planning and Navigation System for PAO

2.1.1 System Workflow

Here we would like to briefly summarize the workflow of our previously developed computer-assisted planning and navigation system for PAO as shown in Fig. 1. For detailed description, we refer to [9, 10].

Our system works in two stages: pre-operative planning stage and intra-operative navigation stage. The input to the pre-operative planning stage is 3D surface models of pelvis and femur generated from pre-operatively acquired CT data

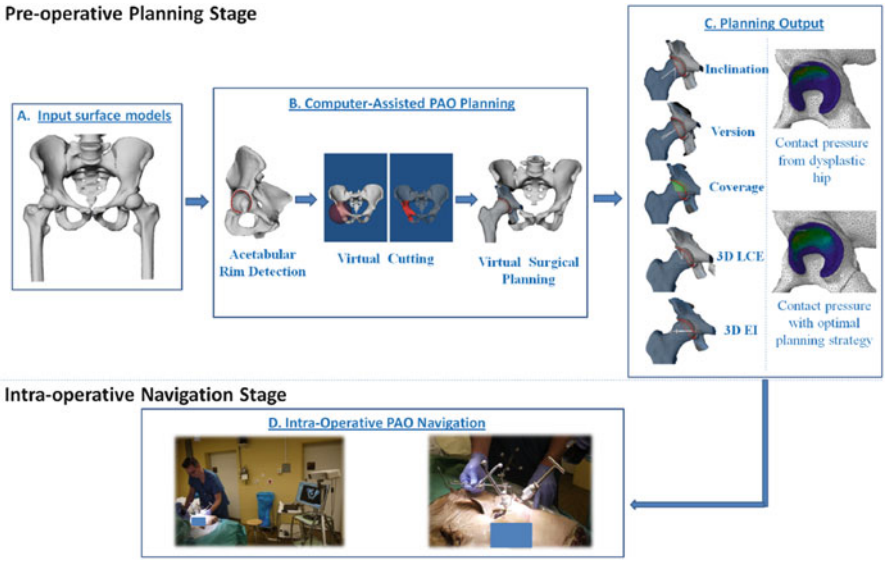

Fig. 1 Schematic view of our computer-assisted planning and navigation of PAO. (**a**) The input surface models; (**b**) computer-assisted PAO planning; (**c**) the pre-operative planning output; (**d**) intra-operative PAO navigation for implementing the planned PAO surgery

using a commercially available segmentation program (AMIRA, Visage Imaging, San Diego, USA). The pelvic local coordinate systems is then established using anatomical landmarks extracted from the CT data (see Fig. 1) which is defined on the anterior pelvic plane (APP) using the bilateral anterior superior iliac spines (ASISs) and the bilateral pubic tubercles [19]. After local coordinate system is established, a fully automatic detection of the acetabular rim is conducted using an improved algorithm [9] for the rim detection method of [16]. The detected acetabular rims allow for quantifying the acetabular morphology with parameters such as version, inclination, and acetabular coverage. After that, virtual reorientation procedure for acetabulum fragment is performed until an optimal biomechanics situation is obtained. The results from the planning stage are then passed to the intra-operative navigation stage [10] where a visual feedback is provided during the acetabular fragment reorientation procedure in order to achieve the planned situation.

2.1.2 Quantifying 3D Hip Joint Morphology

Accurate assessment of acetabular morphology and its relationship to the femoral head is essential for PAO planning. As soon as acetabular rim points are extracted, least-squares fitting is used to fit a plane to these points. The fitted plane then allows for computing acetabular inclination and anteversion [13] (see Fig. 1c). Additional hip morphological parameters such as the 3D LCE angle, the 3D femoral head

extrusion index (EI), and the 3D acetabular coverage (AC) are computed as well (see Fig. 1c). LCE is depicted as an angle formed by a line parallel to the longitudinal pelvic axis and by the line connecting the center of the femoral head with the lateral edge of the acetabulum according to Wiberg [17]. EI is defined as the percentage of uncovered femoral head in comparison with the total horizontal head diameter according to Murphy et al. [11]. AC is defined to be a ratio between the area of the upper femoral head surface covered by the acetabulum and the area of the complete upper femoral head surface.

2.1.3 Virtual PAO Surgical Procedure

A virtual PAO procedure is conducted with our system as follows. First, a sphere is used to simulate osteotomy operation. The center of femoral head is taken as the center of the sphere whose radius and position can be interactively adjusted along lateral/medial, caudal/cranial, and dorsal/ventral directions, respectively, in order to approximate actual osteotomy operation (see Fig. 2a). After that, the virtual PAO procedure is conducted by interactively changing the inclination and the anteversion of the acetabulum fragment (see Fig. 2b). During the acetabulum fragment reorientation, 3D LCE angle, EI, and AC are computed in real time based on the reoriented acetabulum fragment and showed at the bottom of the screen (see Fig. 2b). Once a desired position is achieved, the realigned model is stored and transferred to the biomechanical analysis module for an FE simulation as explained in detail in the following section.

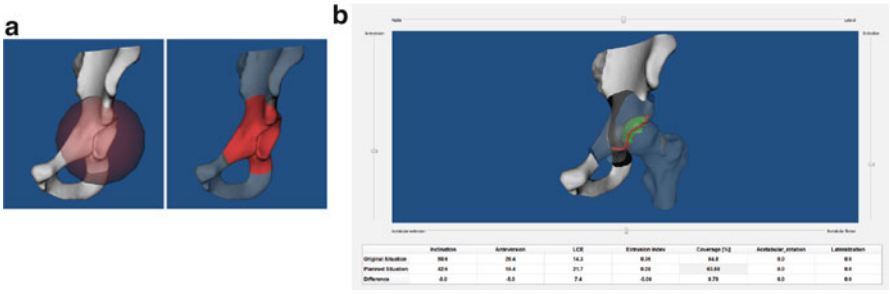

Fig. 2 Virtual PAO surgical procedure in our PAO planning system. (**a**) Virtual cutting operation is done with a *sphere*, whose radius and position can be interactively adjusted; (**b**) virtual reorientation operation is done by interactively adjusting anteversion and inclination angle of the acetabulum fragment

2.2 *Patient-Specific Biomechanical Model*

2.2.1 Mesh Generation

Bone surface models of the reoriented hip joints are imported into ScanIP software (Simpleware Ltd., Exeter, UK). While patient-specific cartilage models are essential in biomechanical simulation, it has been previously reported in [14] that the predicted optimal alignment of the acetabulum was not significantly sensitive to the choice of cartilage thickness distribution over the acetabulum. Therefore a 3D dilation operation was performed on femoral head and acetabular surfaces to create femoral and pelvic cartilage layers with a constant thickness as has been done in [1]. Reconstructed surfaces were smoothed with a recursive Gaussian filter to remove segmentation artifacts (Fig. 3a, c).

Surfaces were discretized using tetrahedral elements (Fig. 3b, d). Since the primary concern was focused on the joint contact, a finer mesh was employed for the cartilage than for the bone. Refined tetrahedral meshes were constructed for the cartilage layers using ScanFE module (Simpleware Ltd., Exeter, UK). Cortical bone surfaces were discretized using coarse tetrahedral elements. Trabecular bone was not included in the models, for it has little effect on predictions of contact stress as

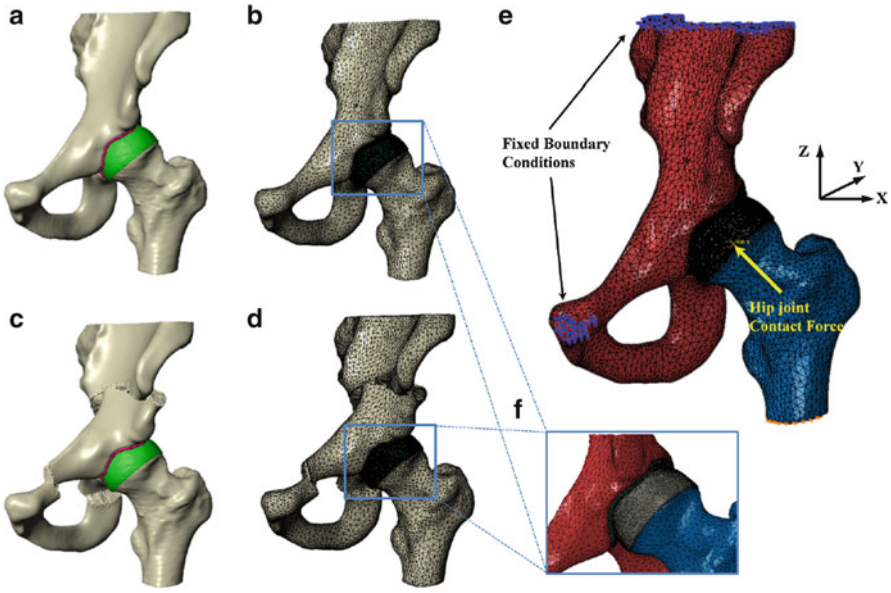

Fig. 3 Biomechanical simulation of contact pressure on acetabular cartilage. (**a**) Surface models for dysplastic hip; (**b**) volume meshes for dysplastic hip; (**c**) surface models for a planned situation after acetabulum fragment reorientation; (**d**) volume meshes for the planned situation; (**e**) boundary conditions and loading for biomechanical simulation; (**f**) coarse meshes for pelvic and femoral models, and refined meshes for pelvic and femoral cartilages

reported in [1]. Tied and sliding contact constraints were used in Abaqus/CAE 6.10 (Dassault Systmes Simulia Corp, Providence, RI) to define the cartilage-to-bone and cartilage-to-cartilage interfaces, respectively. It has been reported in [5] that the friction coefficient between articulating cartilage surfaces is very low, on the order of 0.01–0.02 in the presence of synovial fluid. Therefore, it is reasonable to neglect frictional shear stresses between contacting articular surfaces.

2.2.2 Material Property

Pelvic and femoral cartilages were modeled as homogeneous, isotropic, and linearly elastic material with Young's Modulus $E = 15\,\text{MPa}$ and Poissons ratio $= 0.45$. Cortical bone of pelvis and femur were modeled as homogeneous, isotropic material with elastic modulus $E = 17\,\text{GPa}$ and Poissons ratio $= 0.3$ as has been used in [20].

2.2.3 Loading and Boundary Conditions

The loading and boundary conditions used in this paper resemble those used by Phillips et al. [15] (Fig. 3e). The top surface of pelvis and pubic areas were fixed, and the distal end of the femur was constrained to prevent displacement in the body x and y directions while being free in vertical z direction (Fig. 3e). The center of femoral head derived from a least-square sphere fitting was selected to be the reference node. The nodes of femoral head surface are constrained by the reference node via kinematic coupling. The fixed boundary condition model was then subjected to a loading condition as published in [4], representing a single leg stance situation with the resultant hip joint contact force acting at the reference node. Although CT scan was performed in the supine orientation and the loading condition of our biomechanical simulation is based on one-leg stance situation [4], previous work [14] has shown that there is no significant difference between the contact pressure in the Bergmanns reference frame and those in the supine reference frame. In addition, as pointed out by Armiger et al. [3], it is not an infrequent clinical practice to use the supine frame as an estimate of the standing frame. Therefore we believe our model makes good use of valuable, available data from Bergmanns work [4]. Following the loading specification in [15], the components of joint contact force along three axes are given as 195, 92, and 1,490 N, respectively, by assuming a constant body weight of 650 N for all subjects to remove any scaling effect of body weight on the absolute value of the contact pressure. The resultant force is applied based on anatomical coordinate system described in Bergmann et al. [4], whose local coordinate is defined with the x axis running between the centers of the femoral heads (positive running from the left femoral head to the right femoral head), the y axis pointing directly anteriorly, and the z axis pointing directly superiorly.

2.3 Experiment Design and Results

A preliminary study was conducted to verify the efficacy of the developed FE model. In this study, 3D models of hip joints are produced based on CT scans from two subjects with hip dysplasia. For each subject, the acetabulum fragment was virtually rotated in 4° increment in the APP from the original acetabulum inclination angle, thus their corresponding planned situation has different hip joint morphological parameters (3D LCE and AC). The loading condition consists of static and dynamic loading scenarios. In static loading scenario, constant components of resultant force were applied to hip joint. However, in dynamic loading scenario, a time-dependent force function with a duration of 11 s was applied to the center of hip joint. This dynamic time-dependent force function was derived from the in vivo measurement data published by Bergmann et al. [4]. The mesh models of original dysplastic hip and a series of planned situations were imported into Abaqus simulation environment for biomechanical simulation (see Fig. 3 for details). The peak contact pressure and total contact area are directly extracted from the output of Abaqus. We then compared quantitatively the peak contact pressure and contact area on acetabulum cartilage in different acetabulum position and investigated optimal planning strategy in static one-leg stance loading scenario.

Figure 4 shows how contact pressure distribution of the pelvic cartilage changed for the 1st dysplastic hip when AC and 3D LCE angle were increased. The contact area originally focused on the superior region and almost no contact area was in the anterior and posterior regions. When the AC and 3D LCE angle were increased, the contact area shifted from lateral region towards the medial region. Figure 5a, c

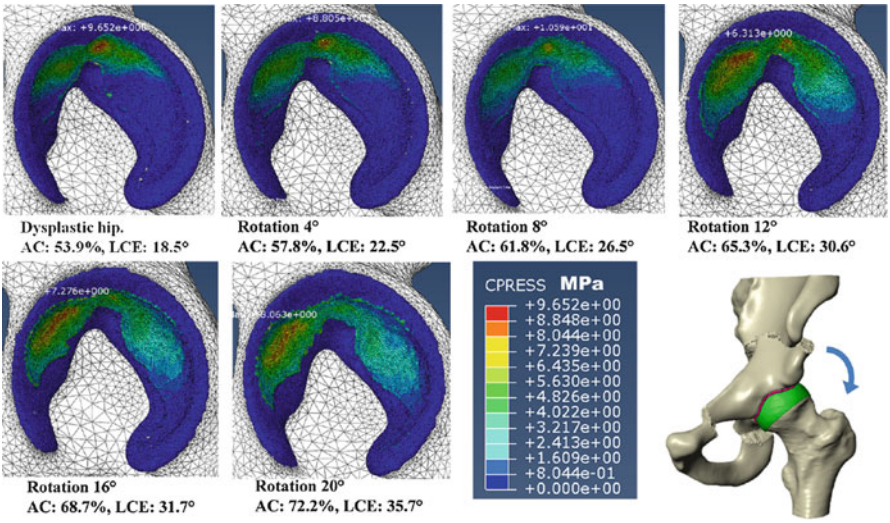

Fig. 4 Contact pressure distribution on acetabular cartilage for 1st dysplastic hip in static one-leg stance situation

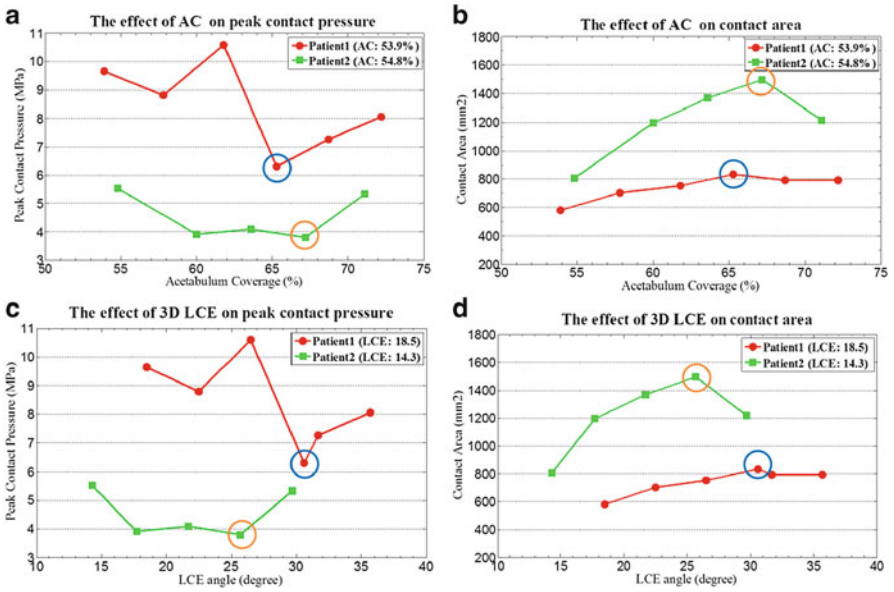

Fig. 5 (**a**) Effect of AC on hip joint peak contact pressure. *Circled points* represent the lowest pressures for each subject; (**b**) effect of AC on hip joint contact area. *Circled points* indicate the largest contact areas for each subject; (**c**) effect of 3D LCE on hip joint peak contact pressure. *Circled points* represent the lowest pressures for each subject; (**d**) effect of 3D LCE on hip joint contact area. *Circled points* indicate the largest contact areas for each subject

present peak contact pressures at different AC and 3D LCE angles. Contact areas are shown in Fig. 5b, d as well. The peak contact pressures and contact areas are available for both pelvic and femoral cartilages, but in our study only contact pressure pattern of the pelvic cartilage was investigated. An optimal acetabulum fragment reposition with minimum peak contact pressure and maximum contact area was achieved for both dysplastic hips. More importantly, for each hip, both the minimal peak contact pressure and the maximum contact area were achieved at the same acetabulum fragment reposition. A large rotation of acetabulum does not guarantee low peak contact pressure and large contact area. For two dysplastic hips, we found that the peak contact pressures on the optimal planned situations are 6.3 and 3.8 MPa, respectively, while their contact areas are quite different (833.9 and $1,496.7\,\text{mm}^2$, respectively). The reason is simply that these two patients have different acetabulum. For example, the diameters of acetabulum rims from these two patients are 43.6 and 52.6 mm, respectively.

When the optimized position of an acetabulum was found, we then compared the peak contact pressure and the contact area between the original dysplastic hip and the optimally reoriented hip in dynamic one-leg stance loading condition where a time-dependent hip joint force function was applied [4]. The simulation process lasted 11 s in total, and the time-dependent force curve was shown in Fig. 6a. We compared the difference of corresponding peak contact pressure and contact

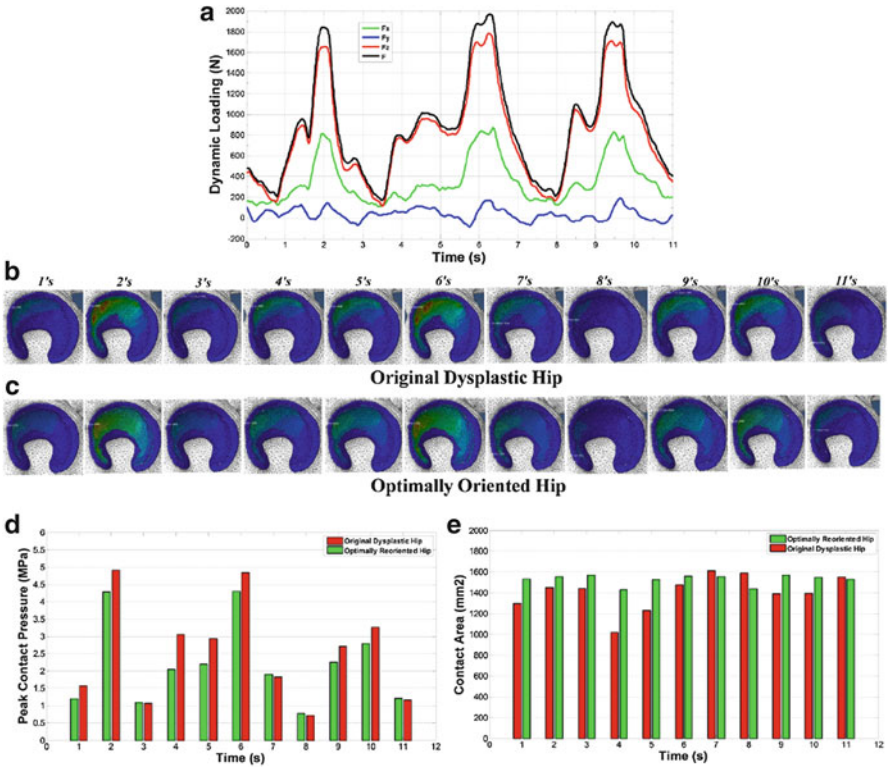

Fig. 6 Contact pressure distribution on acetabular cartilages for dynamic one-leg stance loading scenario. (**a**) Time-dependent dynamic loading input; (**b**) contact pressure distribution of the original dysplastic hip over the 11 s simulation; (**c**) contact pressure distribution of the optimally reoriented hip over the same 11 s simulation; (**d**) comparison of peak contact pressures between the original dysplastic hip and the optimally reoriented hip over the 11 s simulation; (**e**) comparison of contact areas between the original dysplastic hip and the optimally reoriented hip over the 11 s simulation

area at each second (see Fig. 6b, c) between the original dysplastic hip and the optimally reoriented hip. Our simulation results show that when the results of the optimally reoriented hip were compared with those of the original dysplastic hip, the peak pressures were reduced while the contact areas were increased (see Fig. 6d, e).

3 Discussions and Conclusion

In this paper, we proposed and developed a patient-specific 3D FE model for optimization of the acetabulum reorientation after PAO. A preliminary study conducted on two dysplastic hips were used to verify the efficacy of the developed FE model.

It is known that the purpose of PAO is to increase acetabular coverage of the femoral head and thereby decrease contact pressure over the cartilage surface [8], so this has motivated the recent introduction of various computer-assisted planning systems for PAO based on biomechanics optimization [2, 3, 20]. The BGS introduced by Armand et al. [2] performed DEA to estimate the contact pressure on a patient-specific model in short periods of time. Although DEA is a computationally efficient method for modeling of cartilage stress, it is still an approximate method to estimate the location and magnitude of the peak contact pressure compared to FE methods, because the results of DEA that the stress distribution becomes smoother and the peak pressures are underestimated as reported in [14]. Different from the method of Armand et al. [2, 3], we developed a patient-specific 3D FE model for biomechanical analysis derived from our computer-assisted planning system, which is computationally expensive but more accurate. Compared to the results reported by Zou et al. [20], who also developed a 3D FE simulation of PAO in order to find optimal reorientation position by minimizing peak contact pressure and at the same time maximizing contact area of the cartilage surfaces, our results are consistent with theirs. Both studies have proved that 3D FE model is an efficient tool to predict cartilage contact stress change before and after PAO reorientation planning [20]. However their virtual PAO procedure was roughly performed in Abaqus due to the fact that Abaqus does not have a precise virtual reorientation planning tool and an accurate approach for quantifying 3D hip joint morphology. In addition, their work modeled only a static loading for biomechanics analysis.

It is worth to mention the limitations of the present method. The main limitation is that a fixed body weight of 650 N derived from Bergmann et al. [4] was applied all two dysplastic hips for 3D FE simulation, which is not real patient-specific in the strict sense. The argument why we adopted such a strategy is that we are aiming to compare the relative change of contact pressure before and after PAO reorientation planning. Thus, it makes sense to use a constant loading, which was originally proposed by Zou et al. [20]. The second limitation of our study is that the number of dysplastic hips for 3D FE model is still too small. The efficacy of the developed FE model needs to be further validated when more cases are available in the future.

In summary, we developed a 3D FE model to predict cartilage contact pressure based on our previously developed computer-assisted planning system for PAO. Our experimental results demonstrated that the developed 3D FE model could be used to find the optimal reorientation of the acetabulum fragment after PAO by minimizing peak contact pressure and at the same time maximizing contact area of the cartilage surfaces. In conclusion, this study suggested that our computer-assisted planning and navigation system with FE modeling can be a promising tool to determine the optimal PAO planning strategy.

Acknowledgements This work was partially supported by the Japanese-Swiss Science and Technology Cooperation.

References

1. Anderson, A.E., Ellis, B.J., Maas, S.A., Peters, C.L., Weiss, J.A.: Validation of finite element predictions of cartilage contact pressure in the human hip joint. J. Biomech. Eng. **130**(5), 051008 (2008)
2. Armand, M., Lepist, J., Merkle, A.C., Tallroth, K., Liu, X., Taylor, R.H., Wenz, J.: Computer-aided orthopedic surgery with near-real-time biomechanical feedback. Johns Hopkins APL Tech. Dig. **25**, 242–252 (2004)
3. Armiger, R.S., Armand, M., Tallroth, K., Lepist, J., Mears, S.C.: Three-dimensional mechanical evaluation of joint contact pressure in 12 periacetabular osteotomy patients with 10-year follow-up. Acta Orthop. **80**(2), 155–161 (2009)
4. Bergmann, G., Deuretzabacher, G., Heller, M., Graichen, F., Rohlmann, A., Strauss, J., Duda, G.N.: Hip contact forces and gait patterns from routine activities. J. Biomech. **34**, 859–871 (2001). Including the HIP98 CD, 3-9807848-0-0
5. Caligaris, M., Ateshian, G.A.: Effects of sustained interstitial uid pressurization under migrating contact area, and boundary lubrication by synovial uid, on cartilage friction. Osteoarthr. Cartil. **16**(10), 1220–1227 (2008)
6. Carlisle, J.C., Zebala, L.P., Shia, D.S., Hunt, D., Morgan, P.M., Prather, H., Wright, R.W., Steger May, K., Clohisy, J.C.: Reliability of various observers in determining common radiographic parameters of adult hip structural anatomy. Iowa Orthop. J. **31**, 52–58 (2011)
7. Clohisy, J.C., Carlisle, J.C., Trousdale, R., Kim, Y.J., Beaule, P.E., Morgan, P., Steger May, K., Schoenecker, P.L., Millis, M.: Radiographic evaluation of the hip has limited reliability. Clin. Orthop. Relat. Res. **467**(3), 666–675 (2009)
8. Ganz, R., Klaue, K., Vinh, T., Mast, J.: A new periacetabular osteotomy for the treatment of hip dysplasia. Technique and preliminary results. Clin. Orthop. Relat. Res. **232**, 26–36 (1988)
9. Liu, L., Ecker, T.M., Schumann, S., Siebenrock, K.A., Nolte, L., Zheng, G.: Computer assisted planning and navigation of periacetabular osteotomy with range of motion optimization. In: Medical Image Computing and Computer-Assisted Intervention MICCAI, pp. 643–650 (2014)
10. Liu, L., Ecker, T.M., Schumann, S., Siebenrock, K.A., Nolte, L.P., Zheng, G.: A novel planning and navigation system for peri-acetabular osteotomy (PAO). Int. J. Comput. Assist. Radiol. Surg. (Suppl 1), S168–S169 (2014)
11. Murphy, S.B., Ganz, R., Muller, M.E.: The prognosis in untreated dysplasia of the hip. A study of radiographic factors that predict the outcome. J. Bone Joint Surg. Am. **77**, 985–989 (1995)
12. Murphy, S.B., Millis, M.B., Hall, J.E.: Surgical correction of acetabular dysplasia in the adult. A Boston experience. Clin. Orthop. Relat. Res. **363**, 38–44 (1999)
13. Murray, D.W.: The definition and measurement of acetabular orientation. J. Bone Joint Surg. Br. **75**(2), 228–232 (1993)
14. Niknafs, N., Murphy, R.J., Armiger, R.S., Lepist J., Armand, M.: Biomechanical factors in planning of periacetabular osteotomy. Biomechanics. **1**(20), 1–10 (2013)
15. Phillips, A.T.M., Pankaj, P., Howie, C.R., Usmani, A.S., Simpso, A.H.R.W.: Finite element modelling of the pelvis: inclusion of muscular and ligamentous boundary conditions. Med. Eng. Phys. **29**, 739–748 (2007)
16. Puls, M., Ecker, T.M., Steppacher, S.D., Tannast, M., Siebenrock, K.A., Kowal, J.H.: Automated detection of the acetabular rim using three-dimensional models of the pelvis. Comput. Biol. Med. **41**, 285–291 (2011)
17. Wiberg, G.: The anatomy and roentgenographic appearance of a normal hip joint. Acta Chir. Scand. Suppl. **83**, 7–38 (1939)
18. Zhao, X., Chosa, E., Totoribe, K.: Effect of periacetabular osteotomy for acetabular dysplasia clarified by three-dimensional finite element analysis. J. Orthop. Sci. **15**, 632–640 (2010)
19. Zheng, G., Marx, A., Langlotz, U., Widmer, K.H., Buttaro, M., Nolte, L.P.: A hybrid CT-free navigation system for total hip arthroplasty. Comput. Aid. Surg. **7**, 129–145 (2002)
20. Zou, Z., Chavez-Arreola, A., Mandal, P., Board, T.N., Alonso-Rasgado, T.: Optimization of the position of the acetabulum in a Ganz periacetabular osteotomy by finite element analysis. J. Orthop. Res. **31**(3), 472–479 (2012)